ENVIRONMENTAL EFFECTS ON INTERFEROMETRIC FIBER OPTIC GYROSCOPE PERFORMANCE

A DISSERTATION SUBMITTED TO

THE GRADUATE SCHOOL OF ENGINEERING AND SCIENCE

OF BILKENT UNIVERSITY

IN PARTIAL FULFILLMENT OF THE REQUIREMENTS FOR

THE DEGREE OF

DOCTOR OF PHILOSOPHY

IN

ELECTRICAL AND ELECTRONICS ENGINEERING

By

Berk Osunluk

February 2021

ENVIRONMENTAL EFFECTS ON INTERFEROMETRIC FIBER OPTIC GYROSCOPE PERFORMANCE

By Berk Osunluk

February 2021

We certify that we have read this dissertation and that in our opinion it is fully adequate, in scope and in quality, as a dissertation for the degree of Doctor of Philosophy.

Ekmel Özbay (Advisor)

B. Orhan Aytür

Coşkun Kocabaş

F. Ömer İlday

Oğuzhan Çifdalöz

Approved for the Graduate School of Engineering and Science:

Ezhan Karaşan

Director of the Graduate School

ABSTRACT

ENVIRONMENTAL EFFECTS ON INTERFEROMETRIC FIBER OPTIC GYROSCOPE PERFORMANCE

Berk Osunluk

Ph.D. in Electrical and Electronics Engineering

Advisor: Ekmel Özbay

February 2021

Today main performance limitations for fiber optic gyroscope technology are its sensitivity to temperature fluctuations and vibration. Shupe error is the main error source for both disturbances. We propose an approach to reduce the thermal sensitivity by controlling the strain inhomogeneity through the fiber coil. The approach is based on advanced fiber coil modeling, which is verified by a series of experiments.

Vibration is often a neglected disturbance by the researchers as it highly depends on the integrated platform. We propose a model for bias error formation due to optical power fluctuations under vibration. Model is composed of power fluctuation characteristics, spurious rotation rate formation due to mechanical Shupe error, and the suppression of the rotation rate by the closed-loop operation. Lastly, we introduce the concept of angle random walk performance degradation under vibration due to interferogram nonlinearity.

Keywords: Fiber optic gyroscope, Shupe error, Thermal sensitivity, Vibration, Bias, Angle random walk (ARW), Interference nonlinearity.

ÖZ

GİRİŞİMÖLÇÜCÜ FİBER OPTİK DÖNÜÖLÇER PERFORMANSI ÜZERİNE ÇEVRESEL ETKİLER

Berk Osunluk

Elektrik-Elektronik Mühendisliği, Doktora

Tez Danışmanı: Ekmel Özbay

Şubat 2021

Günümüzde fiber optik dönüölçer teknolojisi için temel performans limiti sıcaklık hassasiyeti ve titreşimdir. Shupe hatası her iki bozanetken için de temel hata kaynağıdır. Fiber sarımdaki gerinim tektürelsizliğini kontrol ederek sıcaklık hassasiyetini düşüren bir yaklaşım öneriyoruz. Yaklaşım, bir dizi deney ile doğrulanmış ileri seviye bir modellemeye dayanmaktadır.

Titreşim entegre edilen platforma bağlı olduğu için çoğunlukla araştırmacılar tarafından göz ardı dilen bir bozanetkendir. Titreşim altında optik güç salınımları nedeniyle oluşan sabit hata için bir model öneriyoruz. Model optik güç salınım karakteristikleri, mekanik Shupe hatası nedeniyle sahte dönü hızı oluşumu, ve kapalı döngü opearsyon ile dönü hızı baskılanmasını içermektedir. Son olarak girişimölçer doğrusalsızlığı nedeniyle titreşim altında açısal rastgele yürüme performans düşüşünü tanıtıyoruz.

Anahtar sözcükler: Fiber optik dönüölçer, Shupe hatası, Sıcaklık hassasiyeti, Titreşim, Sabit hata, Açısal rastgele yürüme (ARW), Girişim doğrusalsızlığı.

Annem'e

ACKNOWLEDGEMENT

A decade ago, the fiber optic gyroscope jumped into the middle of my professional life and meanwhile, it feels like a child. This thesis is a rite of passage. From now on, our relation will be much more stable, and I may save more time for my beloved toddler, *Uygar*.

Creating this dissertation was not a personal experience, definitely a collective one, and I owe gratitude to a lot of people. First and foremost, I would like to express my sincerest gratitude to my advisor Prof. Ekmel Özbay for his invaluable guidance. I would also like to extend my gratitude to Dr. Burak Seymen for his highly innovative contributions, especially for Chapter 4. My special thanks go to my academic buddy Serdar Öğüt, without whom the thesis may not come true.

This thesis is funded by SSB (Savunma Sanayii Başkanlığı) and Aselsan Inc. with a SAYP (Savunma Sanayii için Araştırmacı Yetiştirme Programı) project. I am very grateful for the resources and facilities that were made available to me during my studies.

I would like to send my warm thanks to each of my family members, but especially to my father, for their continuous support, not only for this thesis but also for my life.

Last, but certainly not least, I would like to thank my wife *Gülçin* for her non-stop support, patience, and help. Her existence makes everything much more meaningful, without which not only this thesis but also anything will be harder.

“. . . Our sons ought to study mathematics and philosophy, . . . navigation, . . . in order to give their children a right to study painting, poetry, music . . .” J. Adams

CONTENTS

LIST OF FIGURES

LIST OF TABLES

LIST OF ALGORITHMS

CHAPTER 1

INTRODUCTION

Today, interferometric fiber optic gyroscope (IFOG, or FOG as commonly used) technology is 45 years old [1]. It has been integrated into many different platforms operating in various environments, including air, naval, and land vehicles, deep drilling platforms, and even space [2], [3], [4]. Today, the trend is towards seeking excellence under different environmental effects. Environmental effects include moisture [5], radiation [6], [7], magnetic field [8], [9], vibration, and temperature fluctuation. The first three disturbances may be suppressed by simple mechanical solutions. Moisture level can be controlled by a hermetically sealed case. Radiation hardened fibers and electro-optic parts are proposed for robust FOG configurations for space applications. The magnetic field effect can be suppressed by a shield having high permeability and covering the Sagnac loop. However, the temperature fluctuations and vibration may limit the performance of FOG; even thermal or mechanical isolators are used.

This dissertation is devoted to defining the performance limitations of FOG due to temperature and vibration effects. Chapter 2 covers the basic principles and structure of commonly used FOG configuration. Shupe equations are direct results of the Sagnac relation. The modulation/demodulation scheme and closed-loop configuration of FOG should be reviewed for a better understanding of the vibration error due to optical fluctuations. Lastly, the interference of the waves forms the basis of the interferogram nonlinearity analyses.

Chapter 3 starts by sketching the panorama of the thermal sensitivity of the FOG coil. Literature work is handled by both referring and repeating it with similar models and simulation scenarios to underline the need for an advanced model. The advanced modeling approach is presented in detail and verified by laboratory experiments. The trimming phenomenon is revisited with simulations. Lastly, different thermal bias error contributions are analyzed and strain inhomogeneity analysis is presented for further improvement of fiber coil. A fiber coil design is reached, showing that the approach proposes simple design changes to increase the performance to the same order of magnitude as the latest developments in the literature. Performance is better than various quadrupole designs [10], [11], [12] and close to octupolar winding performance [11], [12].

Chapter 4 is dedicated to FOG performance under vibration. Vibration, as a disturbance, is highly dependent on the platform on which the sensor is integrated into. Characteristics of the vibration like the frequency range, magnitude, and occurrence rate change dramatically for different vehicles, terrains, and operation concepts. Furthermore, mechanical isolators for the suppression of the vibration may be designed according to the platforms during the integration phase. So, the inertial sensor performance under the vibration is often a neglected issue in the academic literature, sensor tests under vibration are deferred until the integration phase of the project, and engineers/researchers are sleeping on the issue during the design phase. However, the vibration can be the limiting factor of the inertial sensor performance. Today, one of the main limitations of FOG performance is its sensitivity to vibration. Vibration is a time-dependent disturbance on the fiber sensing coil, similar to the temperature, which results in performance degradation. Several literature works focus on the mechanical Shupe error [13], [14], [15], [16], [17] and some the effect of the optical power fluctuation [18], [19]. The mechanical Shupe error is much more investigated and modeled than the latter one.

Detailed analyses of error formation due to optical power fluctuation for different cases are presented in Chapter 4. Error occurs in two different forms: Bias error and Shupe like error. Both errors depend on the multiplication of the Sagnac phase shift with power fluctuation. Bias error exists if only the two signals are in phase. Chapter 4 proceeds to closed-loop configuration and mechanical Shupe error. Sagnac phase shift is a multiplicative term in error equations and closed-loop suppresses the phase shift. The effectiveness of the loop closure, which can often be neglected in the literature, is modeled and part of the optical power estimations in experiments part.

One of the important parts of Chapter 4 is about the non-linear fashion of the interferogram. Nonlinearity creates low frequency error in the FOG output, although no input energy exists at those frequencies. The noise floor of the gyroscope increases under vibration which results in the angle random walk (ARW) performance degradation. The theoretical proposal is supported by the simulations and laboratory experiments of a FOG. To the best of our knowledge, this dissertation is the first literature work about this phenomenon.

CHAPTER 2

BASICS OF FOG

FOG measures the phase shift between two light waves counter-propagating through a rotating loop of fiber. Rotation induces a phase shift between the waves, called the Sagnac effect [20], [21]. This effect depends on the Einstein's special theory of Relativity, although Sagnac explains his experiment as a demonstration of the Aether theory, which bases on the Fresnel-Fizeau drag effect. Von Laue explained the Fresnel-Fizeau drag effect as a relativistic effect by considering the first-order solution of the law of addition of speeds of special Relativity for a medium [2].

The Sagnac phase shift between the counter-propagating waves can be measured with an interferogram. The rotation rate is obtained by measuring the power level of the interfering waves.

2.1 Sagnac Scale Factor

Two counter-propagating waves in a fiber loop experience a relative phase shift while the loop rotates about its symmetry axis (Figure 2.1). Counter-propagating waves enter the loop at the same time with identical phases. The shift of the exit point due to rotation causes one of the waves to exit the loop earlier and the other one later.

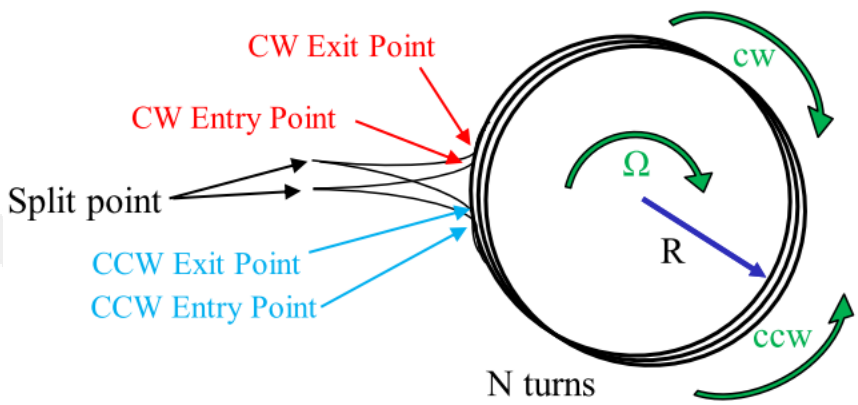

Figure 2.1: Sagnac effect.

Time difference between the waves due to rotation,

$$t_{cw} = \frac{R(2\pi + \Omega t_{cw})}{c} \tag{2.1}$$

$$t_{ccw} = \frac{R(2\pi - \Omega t_{ccw})}{c} \tag{2.2}$$

where t_{cw} and t_{ccw} are propagation times of clockwise (CW) and counter- clockwise (CCW) waves respectively. R is the radius of the fiber coil loop, Ω is the rate of rotation, and c is the velocity of light in vacuum. The time difference is,

$$\Delta t = t_{cw} - t_{ccw} \tag{2.3}$$

$$\Delta t = \frac{4\pi\Omega R^2}{c^2 - \Omega^2 R^2} \tag{2.4}$$

A number of loops of fiber can be wound on a fiber coil to enhance the effect. Multiplying the equation with number of loops N and by using the approximation $c^2 \gg \Omega^2 R^2$,

$$\Delta t = \frac{4\pi\Omega R^2 N}{c^2} \tag{2.5}$$

$$\Delta t = \frac{LD\Omega}{c^2} \tag{2.6}$$

where, L is the length and D is the diameter of the fiber coil. Waves travel the loop with the angular velocity $\omega = \frac{2\pi c}{\lambda}$, where λ is the wavelength in vacuum. Phase difference between the waves due to the Sagnac effect becomes,

$$\Delta\phi = \frac{2\pi LD}{\lambda c}\Omega \tag{2.7}$$

This linear coefficient between the rotation rate and the phase shift is named Sagnac Scale Factor. Equation (2.7) also applies to the fiber medium where c and λ values are still for the vacuum.

2.2 Interference of Waves

Two coherent counter-propagating waves interfere and create an optical power shift due to the phase difference between the waves. The Sagnac effect can be measured by using an interferometer. Two monochromatic waves with a phase difference can be defined as,

$$E_1(\mathrm{x}, \mathrm{t}) = E_{10}\hat{y}sin(kx - \omega t) \tag{2.8}$$

$$E_2(\mathrm{x}, \mathrm{t}) = E_{20}\hat{y}sin(kx - \omega t + \Delta\phi) \tag{2.9}$$

where k is the wave vector,

E_{10} and E_{20} are electric field intensities,

and $\hat{y}$ is the unit vector.

Time averaged optical power output of the interference of the waves can be computed as,

$$P(x,t) = c\varepsilon_0 |E_1(\mathrm{x}, \mathrm{t}) + E_2(\mathrm{x}, \mathrm{t})|^2 \tag{2.10}$$

$$P(x,t) = c\varepsilon_0 \left[\frac{{E_{10}}^2}{2} + \frac{{E_{20}}^2}{2} + \langle 2E_{10}E_{20}sin(kx - \omega t)sin(kx - \omega t + \Delta\phi)\rangle\right] \tag{2.11}$$

$$P(x,t) = c\varepsilon_0 \left[\frac{{E_{10}}^2}{2} + \frac{{E_{20}}^2}{2} + E_{10}E_{20}\langle cos(\Delta\phi) - cos(2kx - 2\omega t + \Delta\phi)\rangle\right] \tag{2.12}$$

$$P(x,t) = P_1 + P_2 + 2\sqrt{P_1P_1}cos(\Delta\phi) \tag{2.13}$$

where P_1 and P_2 are the average optical power of the two interfering waves. Under the assumption of $P_1 = P_2$,

$$P(x,t) = \frac{I_0}{2}[1 + cos(\Delta\phi)] \tag{2.14}$$

where I_0 is the maximum optical power, i.e. when $\Delta\phi$=0.

2.3 Minimum FOG configuration

A rotation rate measurement setup can be formed by using a light source for the light wave creation, a coupler to divide the light wave into counter-propagating waves, a fiber coil to obtain the Sagnac effect, and a detector to convert the optical power due to interference into current (Figure 2.2). Rate measurement can be obtained with this simple configuration. Optical power remains at maximum in the no-rotation case and it decreases under any rotation, CW or CCW, which states the lack of the direction information of the rotation rate input.

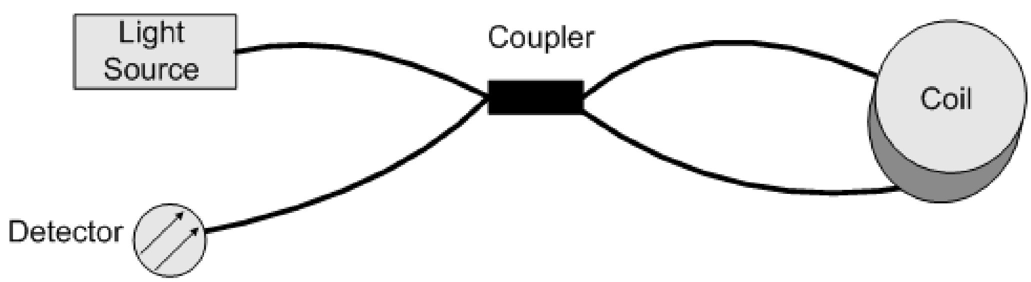

Figure 2.2: Rotation rate sensing device.

Phase modulation is the common way to overcome this problem. Phase bias is injected between the waves using a phase modulator. Multifunctional integrated optical chip (MIOC) and piezoelectric transducer (PZT) are two widely used phase modulators for injecting a phase shift. Although there are several FOGs making use of PZT in the market, MIOC is much more preferred due to its much higher bandwidth and phase stability.

Besides the phase bias injection, the configuration of a FOG should be reciprocal [22]. The reciprocal configuration ensures the waves travel the same optical path so that only the Sagnac effect results in a phase delay. Reciprocal configuration brings the need for using a second coupler.

Lastly, the fiber has a slightly anisotropic structure: Optical path length and the refractive index is different for the waves with orthogonal polarization states. If both of the polarization states are let to propagate through the loop, then spurious waves interfere at the detector with a birefringence phase shift rather than the Sagnac phase shift. Using a polarizer in the optical path is a solution for this problem [22]. Figure 2.3 shows the minimum FOG configuration including a polarizer, second coupler, phase modulator, and bias modulation/demodulation electronics.

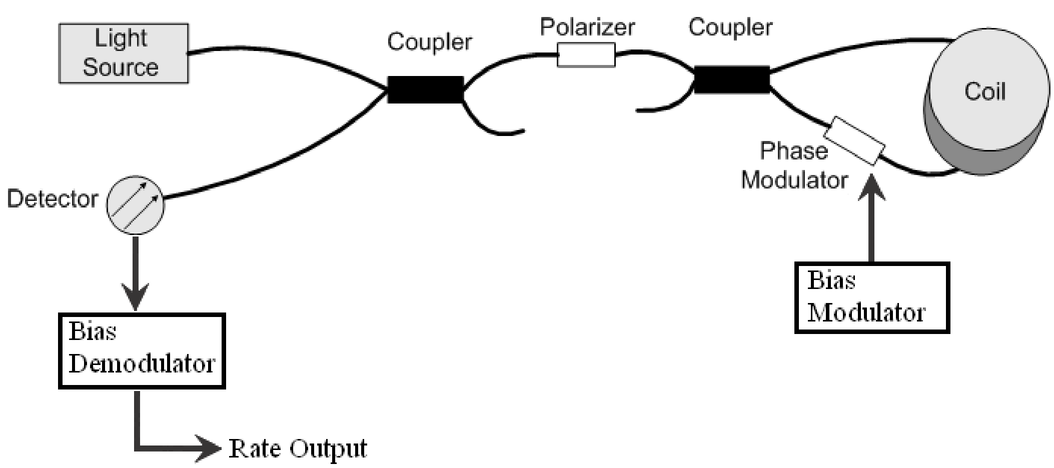

Figure 2.3: Open-loop FOG configuration.

2.4 Phase modulation/demodulation

Square wave modulation is a commonly used modulation technique for high performance FOGs. The objective of injecting phase bias is achieved by the use of a reciprocal phase modulator placed at one end of the coil that acts as a delay line (Figure 2.3). Both interfering waves carry exactly the same phase modulation due to the reciprocity, except for a shift in time. The time shift between the waves exactly equals the coil-loop transit time of the waves if the phase modulator is placed at one of the ends of the fiber loop. Two waves enter the coil in counter directions after their split at the coupler. One of the waves experiences the phase shift injected at the phase modulator while the second one experiences after traveling the fiber coil. Coil transit time is calculated as

$$\tau = \frac{nL}{c} \tag{2.15}$$

where L is the fiber coil length, c is the light velocity and n is the refractive index of the medium. Induced phase shift is

$$\Delta\phi_m(t) = \phi_m(t) - \phi_m(t-\tau) \tag{2.16}$$

A square wave with coil transit time half period and $\Delta\phi_m/2$ amplitude can be used.

$$\phi_m(t) = \begin{cases} \dfrac{\Delta\phi_m}{2}, 0 \le t < \tau \\ -\dfrac{\Delta\phi_m}{2}, \tau \le t < 2\tau \end{cases} \tag{2.17}$$

$$\Delta\phi_m(t) = \begin{cases} \Delta\phi_m, 0 \le t < \tau \\ -\Delta\phi_m, \tau \le t < 2\tau \end{cases} \tag{2.18}$$

Equation (2.6) can be rewritten for the two cases,

$$P_0 = \frac{I_0}{2}[1 + \cos(\Delta\phi_s(t) + \Delta\phi_m)] \tag{2.19}$$

$$P_1 = \frac{I_0}{2}[1 + \cos(\Delta\phi_s(t+\tau) - \Delta\phi_m)] \tag{2.20}$$

The Sagnac phase shift can be reconstructed by square wave demodulation.

$$\Delta P = P_1 - P_0 \tag{2.21}$$

The Sagnac phase shift change can be assumed to be much slower than the transit time so $\Delta\phi_s(t+\tau) \cong \Delta\phi_s(t)$ can be assumed.

$$\Delta P = \frac{I_0}{2}[2sin(\Delta\phi_s)sin(\Delta\phi_m)] \tag{2.22}$$

$$\Delta\phi_s = arcsin\left(\frac{\Delta P}{I_0 sin(\Delta\phi_m)}\right) \tag{2.23}$$

2.5 Closed-Loop Configuration

Scale factor of FOG should be linear (i.e. independent of the input) and stable under environmental effects. Equation (2.23) is a nonlinear function due to arcsin. Furthermore, optical power could fluctuate easily with temperature. Closed-loop operation is introduced to overcome these effects. Phase modulator can also be used as a feedback device to cancel out the measured Sagnac phase shift between the counter-propagating waves.

$$P(t) = \frac{I_0}{2}\left[1 + cos(\Delta\phi_s(t) + \Delta\phi_m(t) - \Delta\phi_f(t))\right] \tag{2.24}$$

The modulator must inject a feedback phase shift

$$\Delta\phi_f(t) = \phi_f(t) - \Delta\phi_f(t-\tau) = -\Delta\phi_s(t) \tag{2.25}$$

This equation can be implemented with a digital ramp signal. Ramp dwells at each feedback level for coil transit time duration.

$$\phi_f(t) = \phi_f(t-\tau) - \Delta\phi_s(t) \tag{2.26}$$

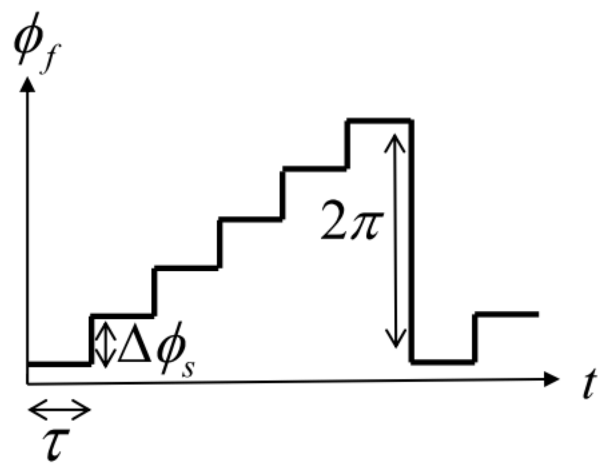

Figure 2.4: Digital ramp for loop closure.

Figure 2.4 shows the digital ramp which must be reset as the voltage level cannot increase indefinitely. These resets may create an error unless the reset amplitude equals to an integer multiple of 2π. If $\Delta\phi_f(t) = -(\Delta\phi_s \pm 2\pi)$, then the cosine term in Equation (2.24) nulls the reset term. Reset amplitude can be set to any multiplicand of 2π up to the maximum applicable voltage to the phase modulator. Any gain error in the feedback path results in an error on the reset amplitude [23]. This can be solved with double closed-loop algorithms [24], [25] and four state bias modulation techniques [26].

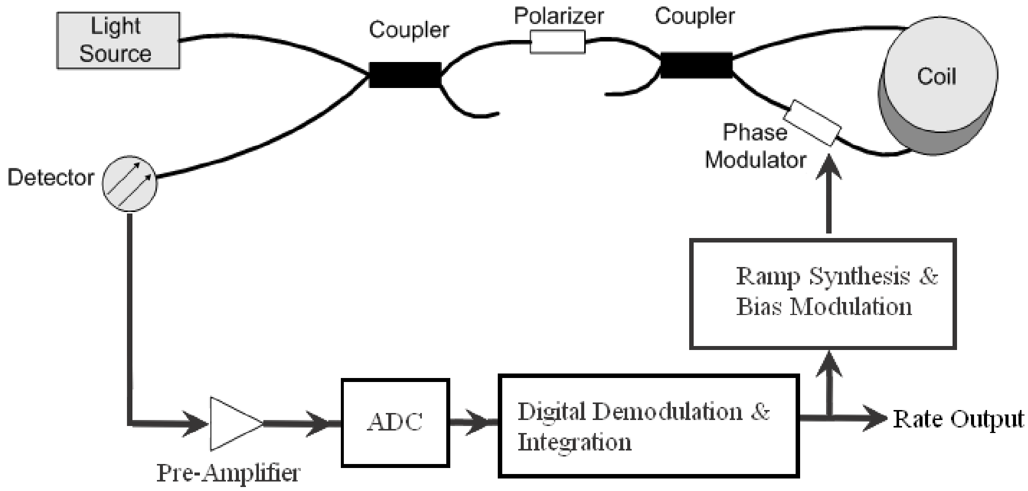

Figure 2.5: Closed-loop FOG configuration.

The closed-loop FOG scheme is given in Figure 2.5. Optical power measured from the photodiode is amplified and converted into voltage by a pre-amplifier. Then an analog to digital converter (ADC) is used to demodulate the signal. The demodulated Sagnac phase is integrated and fed back to the phase modulator. The rotation rate output is the feedback signal. Different controller designs can be used for the loop closure.

2.6 Performance Parameters

Many performance parameters can be defined for FOG as an inertial sensor [27], [28]. Three of the parameters are the most widely referred and directly related to the environmental effects: Bias Error, Scale Factor Stability, and ARW.

2.6.1 Bias Error

Bias error is simply the measurement offset of the sensor. The offset is independent of the rotation rate input as a part of the definition. Gyroscope overall performance is usually defined by the bias error performance. Tactical grade gyroscopes have around 1 °/h bias stability and navigation grades are less than 0.01 °/h. Bias error of

FOG is highly sensitive to the environmental effects. Main bias error mechanisms are phase modulator nonlinearity, intensity modulation, Kerr Effect, Faraday Effect, secondary waves due to backscattering and polarization cross coupling, and Shupe Effect [29]. The last one is one of the main concerns in this dissertation.

2.6.2 Scale Factor Stability

Scale factor of a FOG is the ratio of the output per input rotation rate. The scale factor is desired to be perfectly constant, i.e. gyro signal changes linearly with rotation rate and independent of the environmental effects. Any mechanism that results in an error relative to the input could be classified as the scale factor error. Closed-loop configuration increases the scale factor linearity and stability as mentioned in Chapter 2.5. Mean wavelength is a multiplicative term in Equation (2.7), the Sagnac scale factor. The wavelength stability of the light source is one of the main scale factor instability mechanisms for FOG.

2.6.3 Angle Random Walk (ARW)

Noise consists of statistical, non-deterministic, high frequency fluctuations on FOG rotation rate measurement output. Noise is named as ARW as it results in a random walk in the angle estimation. In early fiber gyros major source of noise was due to Rayleigh backscattering. A portion of the light is scattered backward and is captured by the fiber and propagated back to the detector. The advent of broadband (low coherence) light sources permitted the elimination of this type of noise source [30]. Relative intensity (RIN), TIA, shot, thermal, and driver electronics can be named as the main noise sources.

CHAPTER 3

THERMAL SENSITIVITY

Performance of FOG has been shown to be sensitive to the thermal gradients across the fiber sensing coil by Shupe [31] in 1980 and this phenomenon is called the Shupe effect since then. The second major step was the introduction of the bias error due to the elastooptical interactions [13]. Thermal sensitivity is suppressed to a degree by various winding methods [32], [33]. Novel fiber technologies are introduced to FOG for lower thermal sensitivity [34], [35]. Despite all these attempts, today, the thermal sensitivity of FOG is still a concern. There are plenty of works in the literature about modeling the error [36], [37], [38], [39], [40], [41], [42]. Obtaining a verified simulation environment opens the road for easier analysis of different types of fiber sensing coil schemes, improvement methods or optimum adhesive selection. We present an advanced modeling approach after revisiting a method in the literature by simulations. We give numerical results of various bias error contributions inside the fiber coil. We propose an approach for reducing the strain inhomogeneity inside the fiber coil to reduce the bias error. A coil design performance, which is comparable to the latest developments, is reached and demonstrated by laboratory experiments.

3.1 Review of Theory

3.1.1 Shupe Bias Drift

Light wave experiences a phase shift, Δφ, inside a fiber optic cable with length L and refractive index n, due to a change in the corresponding parameter, ΔL or Δn.

$$\Delta\varphi = \beta_0 n\Delta L + \beta_0 \Delta n L \tag{3.1}$$

where $\beta_0 = \frac{2\pi}{\lambda_0}$, free space propagation constant, λ_0 is the wavelength of the light wave at vacuum.

The change can be induced by environmental effects like temperature [31], vibration [15], or moisture [5]. The total phase shift due to the temperature change is the integral of all infinitesimal fiber portions under the varying temperature field.

$$\Delta\phi = \beta_0 \frac{\partial n}{\partial T}\int_0^L \Delta T(z)dz + \beta_0 n\alpha \int_0^L \Delta T(z)dz \tag{3.2}$$

$$\Delta\phi = \beta_0 \left(\frac{\partial n}{\partial T} + n\alpha\right)\int_0^L \Delta T(z)dz \tag{3.3}$$

$\frac{\partial n}{\partial T}$, refractive index thermal coefficient

α, thermal expansion coefficient

$\Delta T(z)$, Temperature change along the fiber portion z

and $n\alpha$ is negligible with respect to $\frac{\partial n}{\partial T}$. [32]

A fiber loop geometry is given in Figure 3.1, where the CW and CCW light waves travel the loop. CW wave passes a fiber section dz at time $t' = t - \frac{(L-z)}{c}$, with $c = \frac{c_0}{n}$.

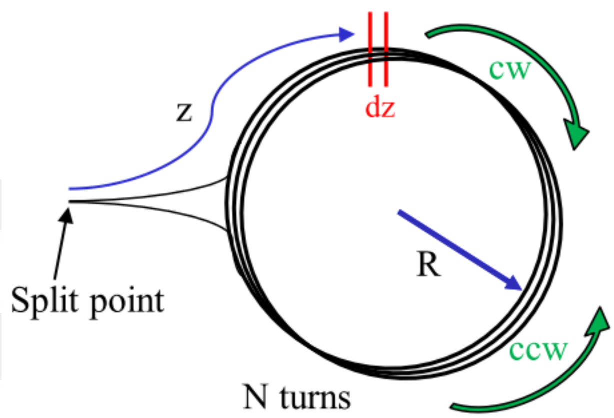

Figure 3.1: Shupe effect.

Integrating over all fiber loop results in extra phase shift due to temperature change for the CW wave, and the CCW,

$$\Delta\phi_{CW}(t) = \beta_0(\frac{\partial n}{\partial T} + n\alpha)\int_0^L \Delta T(z, t - \frac{(L-z)}{c})dz \tag{3.4}$$

$$\Delta\phi_{CCW}(t) = \beta_0(\frac{\partial n}{\partial T} + n\alpha)\int_0^L \Delta T(z, t - \frac{z}{c})dz \tag{3.5}$$

The phase difference between the counter-propagating waves becomes,

$$\Delta\phi(t) = \phi_{cw}(t) - \phi_{ccw}(t) \tag{3.6}$$

$$\Delta\phi(t) = \beta_0(\frac{\partial n}{\partial T} + n\alpha)\int_0^L \left[\Delta T\left(z, t - \frac{(L-z)}{c}\right) - \Delta T\left(z, t - \frac{z}{c}\right)\right] dz \tag{3.7}$$

Using the definition of the time derivative: $\dot{\mathrm{f}} = \lim_{\Delta t \to 0} \frac{[f(t+\Delta t)-f(t)]}{\Delta t}$

$$\Delta\phi(t) = \frac{\beta_0}{c_0}(\frac{\partial n}{\partial T} + n\alpha)\int_0^L \dot{T}(z,t)(L-2z)dz \tag{3.8}$$

can be written.

The FOG works on the Sagnac principle, which states that the rotation of the fiber loop creates a phase difference between the waves with the following relation.

$$\Delta\phi = \frac{2\pi LD}{\lambda c}\Omega \tag{3.9}$$

where D, is the diameter of the fiber loop,

λ, the light wavelength,

c, speed of light,

and Ω, the rotation rate.

$$\Omega(t) = \frac{1}{LD}n(\frac{\partial n}{\partial T} + n\alpha)\int_0^L \dot{T}(z,t)(L-2z)dz \tag{3.10}$$

Equation (3.10) gives the relation between the gyroscope rate error and refractive index change due to temperature drift. Some comments are valuable for this relation: If there is no temperature derivative with respect to time, $\dot{T}(z,t) = 0$, there will be no error; and if there is a temperature derivative with respect to time but same through the fiber, $\dot{T}(z,t) = \dot{T}(t)$, then there will be no error as the integral along dz goes to zero.

3.1.2 Elastooptic Bias Drift

It is shown that temperature fluctuation may result in a change of the refractive index or the expansion of the medium, both increase/decrease the path traveled by the counter-propagating waves. Stress on the fiber also changes the refractive index and the path length [13]. Strain/stress has the relation

$$\begin{bmatrix}\varepsilon_x\\ \varepsilon_y\\ \varepsilon_z\end{bmatrix} = \frac{1}{E}\begin{bmatrix}1 & -\mu & -\mu\\ -\mu & 1 & -\mu\\ -\mu & -\mu & 1\end{bmatrix}\begin{bmatrix}\sigma_x\\ \sigma_y\\ \sigma_z\end{bmatrix} \tag{3.11}$$

where, σ denotes the normal stress along the corresponding axis,

ε, the normal strain,

E, modulus of elasticity,

and μ, the Poisson's ratio.

For an isotropic material, the strain and change of dielectric permeability is related with

$$\begin{bmatrix}\Delta B_x\\ \Delta B_y\\ \Delta B_z\end{bmatrix} = \begin{bmatrix}p_{11} & p_{12} & p_{12}\\ p_{12} & p_{11} & p_{12}\\ p_{12} & p_{12} & p_{11}\end{bmatrix}\begin{bmatrix}\varepsilon_x\\ \varepsilon_y\\ \varepsilon_z\end{bmatrix} \tag{3.12}$$

where, p_{11} and p_{12} are photo-elastic coefficients. The change in the dielectric permeability is:

$$\Delta B_i = B_i - B_0 = \frac{1}{(\Delta \mathrm{n_i} + n)^2} - \frac{1}{n^2} \tag{3.13}$$

Assuming $\Delta \mathrm{n_i}$ is small and using Taylor expansion to the first order term,

$$\Delta B_i \approx -\frac{2\Delta \mathrm{n_i}}{n^3} \tag{3.14}$$

Refractive index change and strain relation becomes

$$\begin{bmatrix} \Delta \mathrm{n_x} \\ \Delta \mathrm{n_y} \\ \Delta \mathrm{n_z} \end{bmatrix} = -\frac{n^3}{2} \begin{bmatrix} p_{11} & p_{12} & p_{12} \\ p_{12} & p_{11} & p_{12} \\ p_{12} & p_{12} & p_{11} \end{bmatrix} \begin{bmatrix} \varepsilon_x \\ \varepsilon_y \\ \varepsilon_z \end{bmatrix} \tag{3.15}$$

We can define the z axis as the direction of the wave propagation and x and y as the radial axes (Figure 3.2). In a polarization maintain (PM) fiber only one polarization state is preserved which can be assumed as the x axis for further derivations.

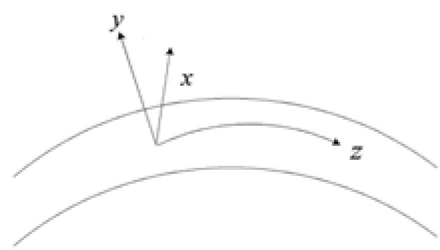

Figure 3.2: Axis definition through the fiber

So refractive index change for the primary axis is

$$\Delta \mathrm{n} = -\frac{n^3}{2}(p_{11}\varepsilon_x + p_{12}\varepsilon_y + p_{12}\varepsilon_{prop}) \tag{3.16}$$

Stress changes the length of the fiber as well. Strain on the z axis elongates the path of the propagating wave,

$$\Delta L = \varepsilon_{prop} L \tag{3.17}$$

The phase shift between the counter-propagating waves can be obtained by using Equation (3.1),

$$\Delta\varphi = \beta_0 \mathrm{n}\varepsilon_{prop}L + \beta_0\left[-\frac{n^3}{2}(p_{11}\varepsilon_x + p_{12}\varepsilon_y + p_{12}\varepsilon_{prop})\right]\mathrm{L} \quad (3.18)$$

Reference [13] states that ε_x and ε_y are the radial strains in a fiber coil geometry, $\varepsilon_x = \varepsilon_y = \varepsilon_r$. Integrating the phase difference over all fiber length gives

$$\Delta\phi(t) = \frac{\beta_0}{c_0}n\int_0^L(\mathrm{A}\dot{\varepsilon}_{prop} - B\dot{\varepsilon}_r)(L-2z)dz \quad (3.19)$$

where, $\mathrm{A} = \mathrm{n}\left(1-\frac{n^2}{2}p_{12}\right)$ and $B = \frac{n^3}{2}(p_{11}+p_{12})$.

Phase error can be turned into gyroscope bias error by incorporating the Sagnac relation.

$$\Omega(t) = \frac{n}{LD}\int_0^L(\mathrm{A}\dot{\varepsilon}_{prop} - B\dot{\varepsilon}_r)(L-2z)dz \quad (3.20)$$

The elastooptic effect is additive to the pure Shupe error and can be combined in a single integral.

$$\Omega(t) = \frac{n}{LD}\int_0^L(\frac{\partial n}{\partial T}\dot{T}(z,t) + \mathrm{A}\dot{\varepsilon}_{prop} - B\dot{\varepsilon}_r)(L-2z)dz \quad (3.21)$$

Strain parameters in Equation (3.21) are the strain fields on the fiber core. The fiber core is surrounded by fiber cladding and coating. The fiber coating is surrounded by adhesive. Lastly, the fiber is wound on a spool usually made by a metal to form the fiber coil. All these surrounding materials with different thermal expansion coefficients create stress on the fiber core. Fiber is wound on the coil with initial stress. This built-in stress creates the same phase shift for both of the counter-propagating waves so this phase shift is reciprocal and does not result in a phase difference. However, any change in the stress field results in phase error. Stress field may change due to temperature [38], vibration [15] or moisture [5].

3.2 Modeling Approaches in the Literature

Calculating the thermally induced bias error of a fiber coil is vital for high performance (navigation or strategic grade) coil designs. Equation (3.21) states that the temperature and strain fields through the fiber coil should be obtained to calculate the total bias error. Second important parameter to be concerned is the $(L - 2z)$ parameter that defines the distance of the fiber portion from the end of the fiber coil. This multiplicative term is very important to reduce the thermal sensitivity. Coil winding method should also be modeled in order to obtain a realistic thermally induced bias error calculation.

3.2.1 Obtaining the Temperature and Strain Fields

The earliest works in the literature [32], [43] define detailed approaches for the calculation of the Shupe error for different coil winding types. These works do not cover the elastooptic effect and the temperature fields are obtained by mathematical derivations. Mathematical modeling of the temperature field may be effective under certain assumptions of symmetric and homogeneous coil structures. On the other hand, using a finite element method (FEM) tool gives the opportunity of modeling all the surrounding elements of the fiber core, even it is neither symmetric nor linear.

Reference [36] models the temperature field with a FEM simulation but stress as a linear function of the temperature. It is stated that the main stress source is the high expansion coefficient of the fiber coating with respect to core and cladding. Expansion of the coating creates stress through the two radial axes of the fiber core under thermal fluctuations (Figure 3.3).

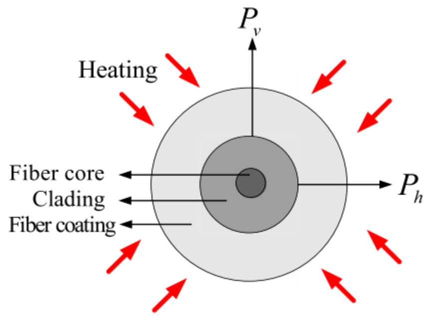

Figure 3.3: Thermal stress on the fiber core due to coating expansion [36].

The equation for the relation of temperature and the coating stress is given as,

$$P_h = P_v = -E_{coating} \times \alpha_{coating} \times \Delta T(t) \tag{3.22}$$

where $E_{coating}$, is the Young's modulus of the coating,

and $\alpha_{coating}$, the thermal expansion coefficient of coating.

From this relation, the effect of the coating stress can be calculated but it is limited only to the coating stress and does not include other sources like the spool or adhesive. Bias error is written by using Equation (3.15) with the assumptions that the cross sectional stresses are the same for x and y axes, without any longitudinal stress.

$$\begin{bmatrix} \sigma_x \\ \sigma_y \\ \sigma_z \end{bmatrix} = \begin{bmatrix} -P(T) \\ -P(T) \\ 0 \end{bmatrix} \tag{3.23}$$

$$\Omega(t) = \frac{n}{LD} \int_0^L \frac{2\mu}{E} + \frac{n^2}{2E} [(1-\mu)p_{11} + (1-3\mu)p_{12}] \dot{P}(T(l,t))(L - 2z)dz \tag{3.24}$$

Another paper [38] presents a model that is verified with experiments. The model includes FEM results for the stress distribution. However, the paper gives a one-dimensional stress distribution where Equation (3.21) states that the stress and the strain should be considered in three dimensions for a better model.

3.2.2 Winding Method

Fiber coil winding is an effective way to suppress the Shupe error. The error is reduced if the counter-propagating waves experience a similar thermal disturbance while traveling the loop. This concept can be seen in $(L - 2z)$ term of Equation (3.21). Any fiber segment located at $\frac{L}{2} - z$, having a distance z from the midpoint of the fiber coil, has a reciprocal point at $\frac{L}{2} + z$ that has the same multiplicative coefficient but with a negative sign. So, if these two points experience the same thermal fluctuation, there will be no Shupe error. The symmetric winding methods (symmetric, dipole, quadrupole, etc.) purposed to locate the symmetric fiber segments as close as possible (Figure 3.4).

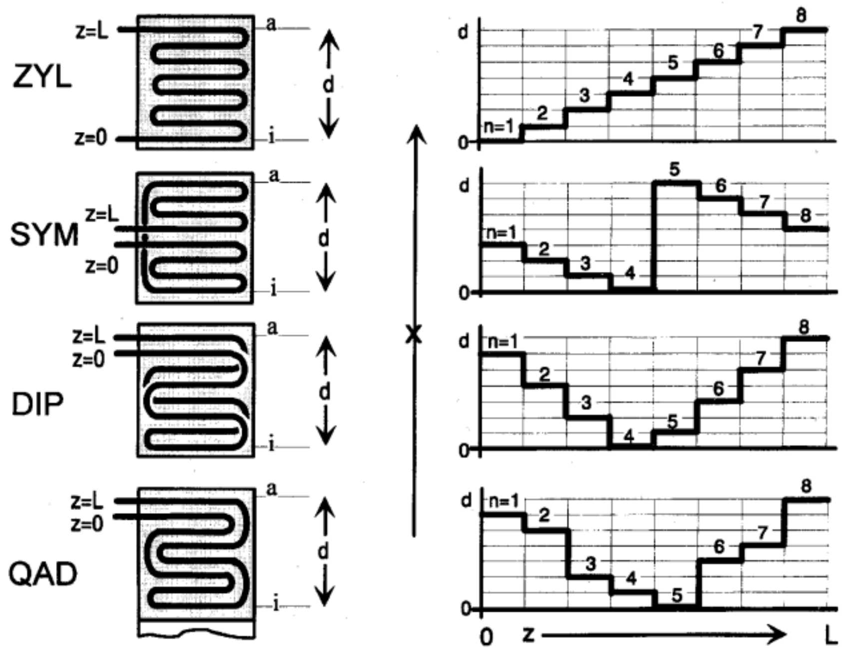

Figure 3.4: Four different fiber coil winding methods, ZYL: Cylinder, SYM: symmetric, DIP: dipole, QAD: Quadrupole [32].

Reference [32] uses a layer by layer integration for the calculation of the bias error. Paper assumes all turns on a layer experiences exactly the same temperature and discretize the equation as

$$\Omega(t) = \frac{L}{D} n \frac{\partial n}{\partial T} \frac{N+1}{N^2} \sum_{\upsilon=1}^{N} \dot{T}(x_\upsilon, t)\,(1 - \frac{2\upsilon}{N+1}) \tag{3.25}$$

where N is the fiber loop turn number and υ is the corresponding fiber coil layer. The coiling scheme enters the equation through x_υ which is substituted from Table 3.1. Layers are radial layers of the fiber coil and layer by layer integration has the assumption that there is no error mechanism through the axial axis of the fiber coil. However, winding patterns can be asymmetric in axial axis due to practical necessities, adhesive application can result in inhomogeneity.

Table 3.1: Layer formulation for different coil types

Coil Type	Layer Number	
	$1 \leq v \leq N/2$	$N/2+1 \leq v \leq N$
ZYL	$v-1$	$v-1$
SYM	$(N-v)-N/2$	$(N-v)+N/2$
DIP	$-\frac{1}{2}+\frac{2N+1}{2}-2v$	$-\frac{1}{2}-\frac{2N+1}{2}+2v$
QAD	$\frac{(-1)^{v}-1}{2}+(N-2v+1)$	$\frac{(-1)^{v}-1}{2}-(N-2v+1)$

Quadrupole winding method is widely used in many FOG configurations. The process steps for winding a quadrupole coil are shown in Figure 3.5. The fiber is pre-wound onto two transfer spools (left and right) (Figure 3.5-a) and the midpoint of the fiber is placed on the coil form. The first layer of the coil is wound by using one of the supply spools (Figure 3.5-b). Then the second and third layers are wound from the second supply spool (Figure 3.5-c). The fourth and fifth layers are wound again from the first spool (Figure 3.5-d). This pattern repeats itself at every fourth layer, so named as quadrupole [44].

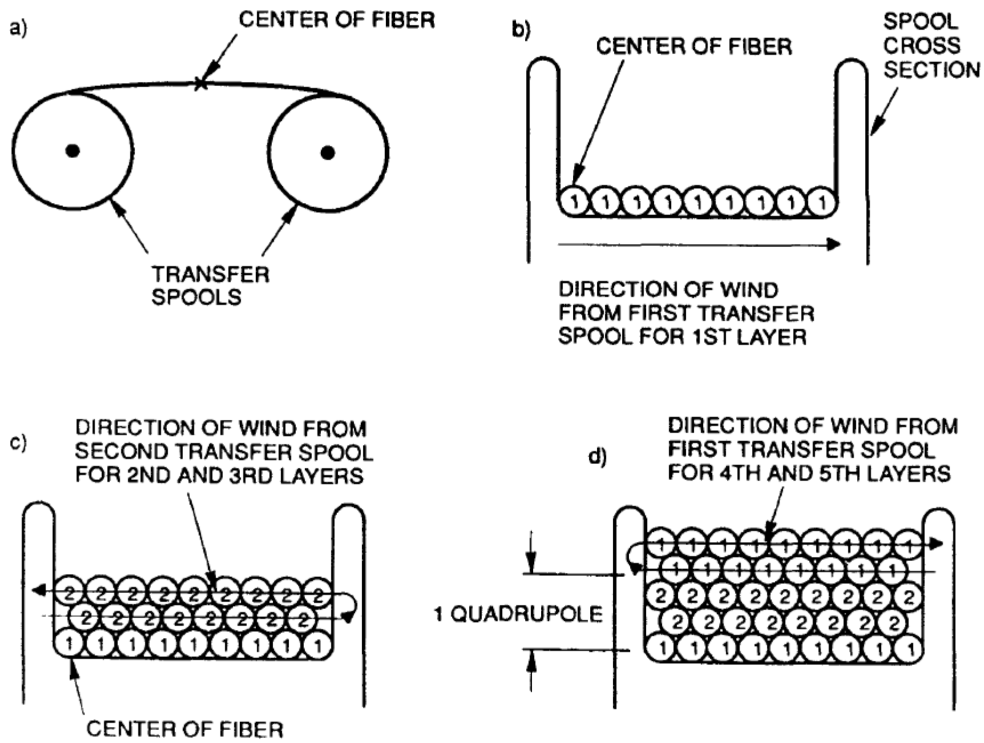

Figure 3.5: Steps in the winding of a quadrupole coil [44].

3.2.3 Repetition of a Literature Model

One of the main approaches to the coil modeling in the literature is obtaining the temperature fields from a FEM model and estimating the stress and strain values, and then the bias errors. In this chapter, we present simulation results of a model similar to a literature work to underline the differences with advanced approaches.

3.2.3.1 Coil Modeling

FEM model includes fiber coil, spool, air environment, and heat source (Figure 3.6). The fiber coil is wounded on a spool and surrounded by the air. The heat source encapsulates the air and provides a temperature profile. Material properties of the spool are well-known so that its modeling is straight forward. On the other hand, fiber coil properties are calculated as a composite material by taking the weighted average of the fiber core, clad, coat and adhesive. FEM provides a simulation with the geometry in two dimensions and estimates a three-dimensional structure. Coil cross-section is divided into meshes, each representing a fiber turn.

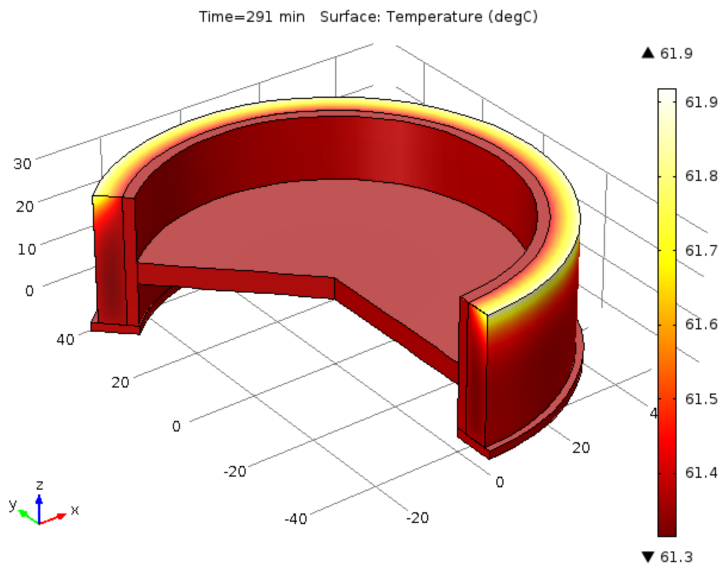

Figure 3.6: Coil model.

3.2.3.2 Analysis Method

Simulation outputs the temperature and stress values for each mesh and time instant. Algorithm 3.1 calculates the temperature derivative from the temperature field; strain fields from stress fields; and strain derivative from the strain fields. The distance of the fiber turn from the one end of the fiber changes for different winding patterns (like cylindrical and quadrupole, Figure 3.7). Lastly, bias errors are calculated.

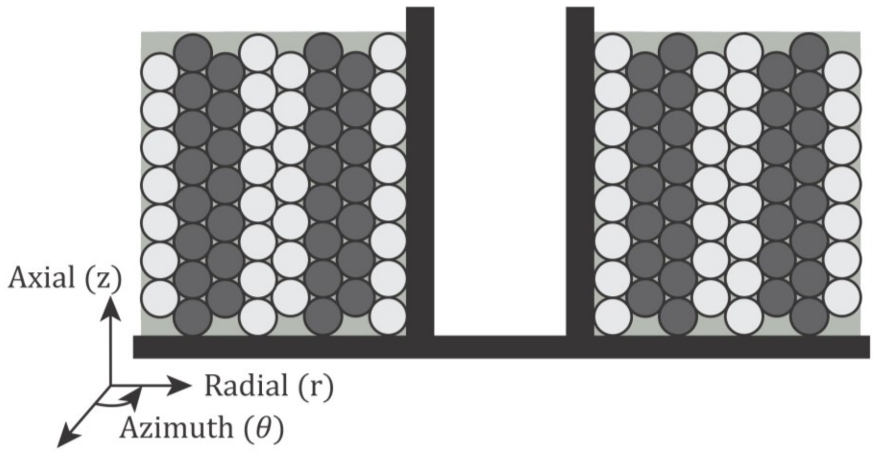

Figure 3.7: Quadrupole winding pattern.

Algorithm 3.1: Matlab code for bias error calculations

```
l_turn_init = data_TempStress(1,1) * 2*pi / 1000;
l_turn_fin = data_TempStress(end-axe_layer,1) * 2*pi / 1000;
l_turn = l_turn_init:(l_turn_fin-l_turn_init)/(layer-1):l_turn_fin; % one turn length, meter
l_turn_ave = (l_turn_fin+l_turn_init)/2;
d_turn = l_turn/pi;
L = l_turn_ave * turns; % total fiber length
xs = data_TempStress(:,1)-data_TempStress(1,1);
ys = data_TempStress(:,2);
Temp = data_TempStress(:,3:4:end); % Temperature
M_stress_s11 = data_TempStress(:,4:4:end); % Stress R
M_stress_s22 = data_TempStress(:,5:4:end); % Stress Phi
M_stress_s33 = data_TempStress(:,6:4:end); % Stress Z


n = 1.46;
ndot = 1.6*1e-5;
t = 0:dt:tfin;
sz = size(Temp);


%% Stress
% Elastooptic coeffs
```

```
p11 = 0.121;
p12 = 0.270;
poisson = 0.17;
E_core = 73.1e9; % Composite, Pa
 eps_x = 1/E_core * (M_stress_s11 -poisson*M_stress_s22 -poisson*M_stress_s33);
eps_y = 1/E_core * (-poisson*M_stress_s11 +M_stress_s22 -poisson*M_stress_s33);
eps_z = 1/E_core * (-poisson*M_stress_s11 -poisson*M_stress_s22 +M_stress_s33);
eps_propaxis  = eps_y;

C1 = n;
C2 = -n^3/2 * p11;
C3 = -n^3/2 * p12;
C4 = -n^3/2 * p12;

%% Coating induced Stress
Ecoat = 1.820e9; %Pa
alpha_coat = 1.5e-4;
Pcoat = -Ecoat * alpha_coat * (Temp-35);
stress_coat = -Pcoat;
eps_coat_x = 1/E_core * (stress_coat          - poisson*stress_coat + 0);
eps_coat_y = 1/E_core * (-poisson*stress_coat + stress_coat          + 0);
eps_coat_z = 1/E_core * (-poisson*stress_coat - poisson*stress_coat + 0);

%% Derivatives
Tempdot = zeros(turns, length(t)-1);
Grad_Tempdot = zeros(turns-1, length(t)-1);
eps_radialX_dot = zeros(turns, length(t)-1);
eps_propaxis_dot = zeros(turns, length(t)-1);
eps_axialZ_dot = zeros(turns, length(t)-1);
eps_coat_x_dot = zeros(turns, length(t)-1);
eps_coat_y_dot = zeros(turns, length(t)-1);
eps_coat_z_dot = zeros(turns, length(t)-1);

for i=1:turns
```

```
  for j = 1:length(t)-1
     Tempdot(i,j) = (Temp(i,j+1) - Temp(i,j)) / dt /60;
     Grad_Tempdot(i,j) = (Tempdot(i+1,j) - Tempdot(i,j)) / dt /60;
     eps_radialX_dot(i,j) = (eps_x(i,j+1) - eps_x(i,j)) / dt /60;
     eps_propaxis_dot(i,j) = (eps_propaxis(i,j+1) - eps_propaxis(i,j)) / dt /60;
     eps_axialZ_dot(i,j) = (eps_z(i,j+1) - eps_z(i,j)) / dt /60;
     eps_coat_x_dot(i,j) = (eps_coat_x(i,j+1) - eps_coat_x(i,j)) / dt /60;
     eps_coat_y_dot(i,j) = (eps_coat_y(i,j+1) - eps_coat_y(i,j)) / dt /60;
     eps_coat_z_dot(i,j) = (eps_coat_z(i,j+1) - eps_coat_z(i,j)) / dt /60;
  end
end
% %Fiber turn Location FOR CYL (CYLINDIRICAL) COIL GEOMETRY
%
% Turn_loc = zeros(turns,1);
% for k=1:layer
%    seri = (k-1)*axe_layer*l_turn + cumsum(ones(axe_layer,1))*l_turn  - l_turn/2;
%    if mod(k,2)==1
%       Turn_loc((k-1)*axe_layer+1:k*axe_layer) = seri;
%    end
%    if mod(k,2)==0
%       Turn_loc((k-1)*axe_layer+1:k*axe_layer) = seri(end:-1:1);
%    end
% end


% QUAD COIL GEOMETRY
Turn_loc = zeros(turns,1);
for k=1:2:layer
    seri = (k-1)/2*axe_layer + cumsum(ones(axe_layer,1))  - 1/2;
    if mod(k,4)==1
        Turn_loc((k-1)*axe_layer+1 : k*axe_layer) = L/2 +
seri*l_turn(k);
        Turn_loc((k)*axe_layer+1 : (k+1)*axe_layer) = L/2  -
seri*l_turn(k+1);
    end
    if mod(k,4) == 3
        Turn_loc((k-1)*axe_layer+1 : k*axe_layer) = L/2  -
seri(end:-1:1)*l_turn(k);
        Turn_loc(k*axe_layer+1 : (k+1)*axe_layer) = L/2  +
seri(end:-1:1)*l_turn(k+1);
    end
```

```
end

%%  Bias Error Calculation
d = 15e-3; %meter
eps_R_dot = (eps_axialZ_dot*0+eps_radialX_dot*1);
eps_coat_R_dot = (eps_coat_x_dot*0.5+eps_coat_y_dot*0.5);
tot_shupe_out = zeros(length(t)-1,1);
tot_eo_out = zeros(length(t)-1,1);
tot_eo_coat_out = zeros(length(t)-1,1);


for j = 1:length(t)-1
    tot_shupe = 0;
    tot_eo = 0;
    tot_eo_coat = 0;
    for i = 1:turns
        layer_no = ceil(i/axe_layer);
        tot _shupe = tot _shupe_ZYL + ndot*Tempdot(i, j) * (L-2*Turn_loc(i)) /l_turn(layer_no) /
d_turn(layer_no);
        tot _eo = tot _eo_ZYL + (C1*eps_propaxis_dot(i,j) + C2*eps_R_dot(i,j) ...
            +C3*eps_R_dot(i,j) + C4*eps_propaxis_dot(i,j) ) * (L-2*Turn_loc(i)) / l_turn(layer_no) /
d_turn(layer_no);
        tot _eo_coat = tot _eo_coat_ZYL + (C1*eps_coat_z_dot(i,j) + C2*eps_coat_R_dot(i,j) ...
            +C3*eps_coat_R_dot(i,j) + C4*eps_coat_z_dot(i,j) ) * (L-2*Turn_loc(i)) /
l_turn(layer_no) / d_turn(layer_no);
end
    tot _shupe_out(j) = tot _shupe/turns*L; % divide turns and multiply by L for discretization of
the integral
    tot _eo_out(j) = tot _eo/turns*L;
    tot _eo_coat_out(j) = tot _eo_coat/turns*L;
end
rate_err_shupe = 1/L * l_turn_ave * n* toplam_shupe_out* 180/pi * 3600;
rate_err_eo = 1/L * l_turn_ave * n* toplam_eo_out* 180/pi * 3600;
rate_err_eo_coat = 1/L * l_turn_ave * n* toplam_eo_coat_out* 180/pi * 3600;
rate_err = rate_err_shupe + rate_err_eo + rate_err_eo_coat;
```

3.2.3.3 Simulations

A simulation environment similar to the literature work [38] is built. Parameters for the coil model are given in Table 3.2 and Table 3.3. Reference [38] models Young's modulus and the thermal coefficient of the coating and glue changing over the temperature. We used the room temperature values steady with respect to temperature for these parameters in the simulations.

Table 3.2: Coil Parameters [38]

Fiber Length (m)	992.79
Clockwise fiber length (m)	469.38
Anticlockwise fiber length (m)	496.41
Number of winding layer	40
Number of loop per layer	68
Inner radius of the coil (m)	0.0550
Outer radius of the coil (m)	0.0605
Coil Height (m)	0.013

Table 3.3: Modeling Parameters (Adapted from [38])

Parameter	Al-alloy	Silica	Coating	Glue
Density (kg/m^3)	2740	2203	1190	970
Specific Heat (J/kg/K)	896	703	1400	1600
Thermal Conductivity (W/K/m)	221	1.38	0.21	0.21
Poisson's Ratio	0.35	0.186	0.4	0.49947

Young's modulus (GPa)	70	76	1.585	1 x 10^{-3}
Thermal expansion coefficient (1/K)	2.3 x 10^{-5}	0.55 x 10^{-6}	7 x 10^{-5}	2.3 x 10^{-4}

The input temperature profile is given in Figure 3.8. The resulting temperature profiles are similar to each other. The model's temperature diffusion shows a little bit slower than the reference with the minimum temperature point is higher.

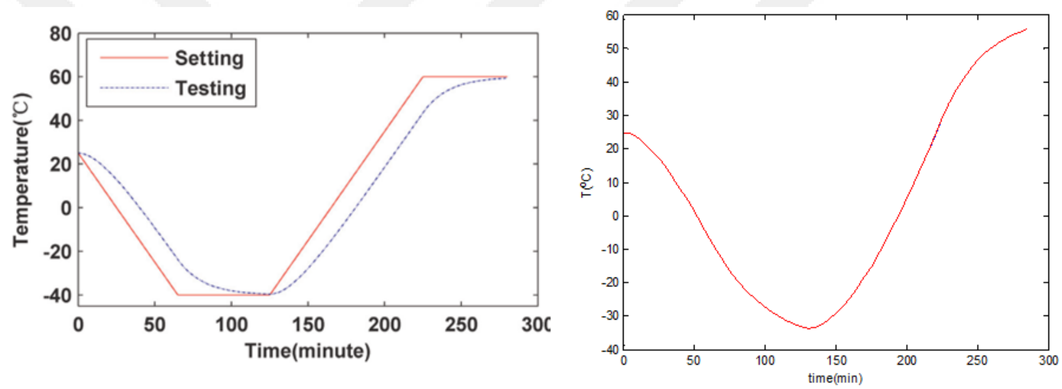

Figure 3.8: Temperature profiles. Reference [38] (left) and the simulation (right).

Temperature and the derivative of the temperature of each fiber turn through the coil are given in Figure 3.9 and Figure 3.10. The gradient along the fiber coil is much slower than the derivative with respect to time. In other words, the temperature is diffused through the fiber coil faster relative to the temperature change. This phenomenon supports the layer by layer integration approximation for the Shupe error calculation made by Reference [32].

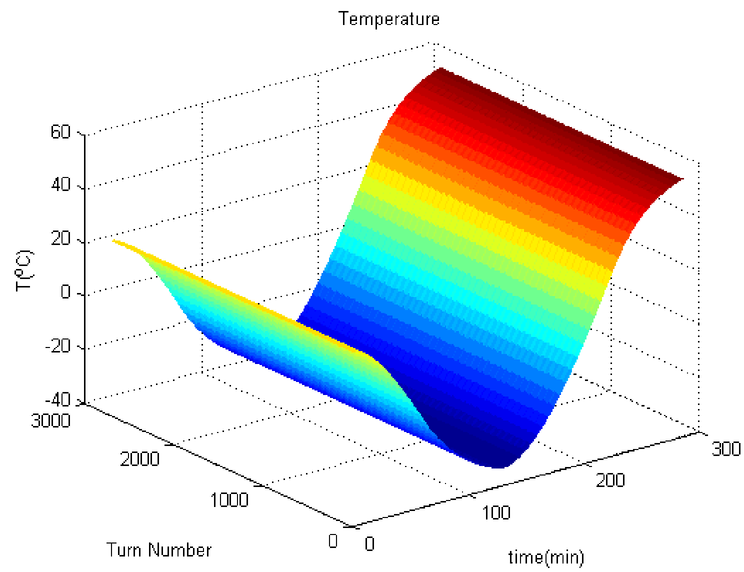

Figure 3.9: Temperature distribution through the fiber coil.

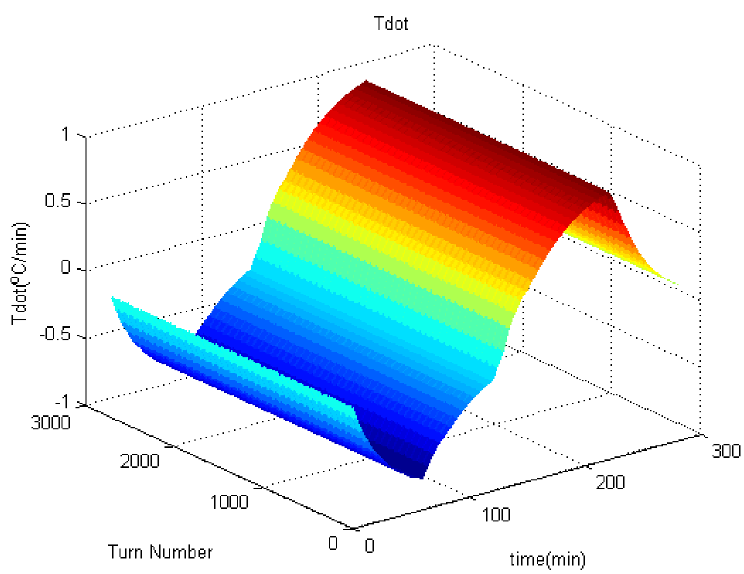

Figure 3.10: Temperature derivative distribution through the fiber coil.

Stress is a disturbance with the components on three directions: Radial, axial, and propagation axis. Stress distributions show different characteristics than the temperature (Figure 3.11, Figure 3.12, and Figure 3.13). Distributions are inhomogeneous which may result in higher bias error than the homogeneous temperature field. Stress gradients are high relative to the time derivative and the graphs get sharper at the edges of the coil.

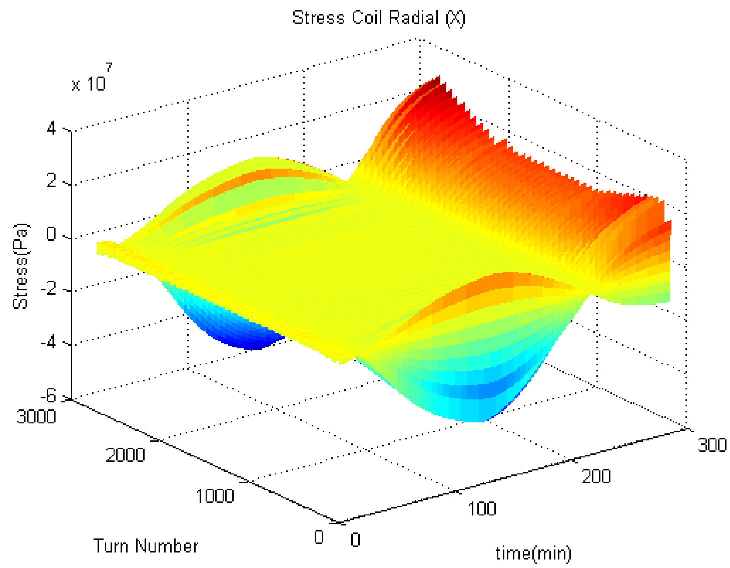

Figure 3.11: Stress distribution through the coil radial axis.

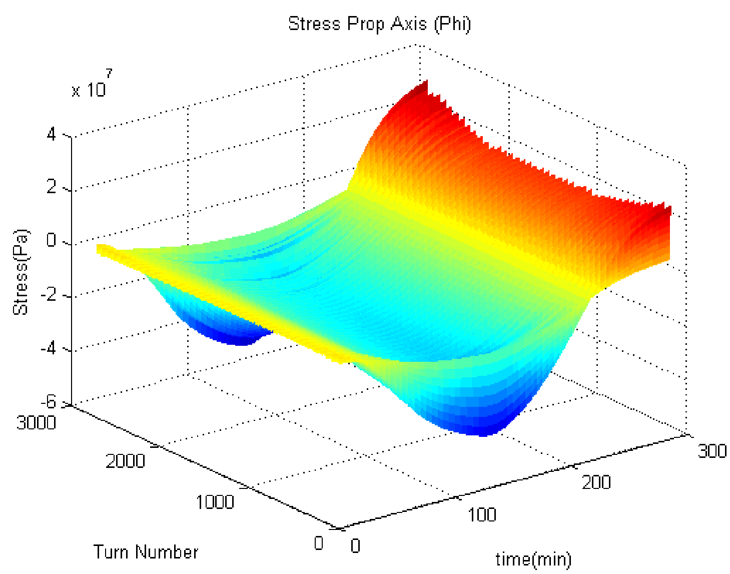

Figure 3.12: Stress distribution through the coil fiber propagation axis.

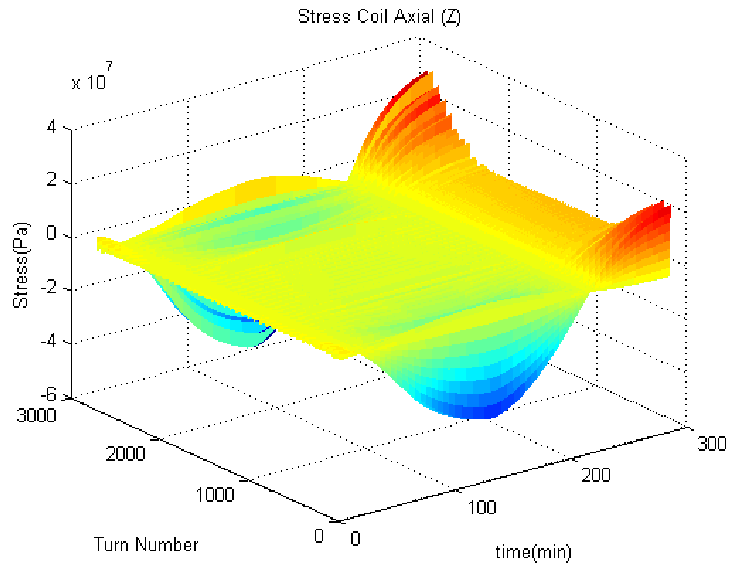

Figure 3.13: Stress distribution through the coil axial axis.

Lastly, bias error estimations are calculated and given with respect to coil temperature in Figure 3.14. Coil temperature starts to decrease from the room temperature to -35°C and turns to increase up to +55°C. Fiber coil visits the temperatures below room temperature twice. Bias error is negative while decreasing and vice versa during the increase phase. This is the effect of the temperature derivative which is aligned with the theory. The Shupe error is nearly twice the elastooptic error. They have the same sign and adds up.

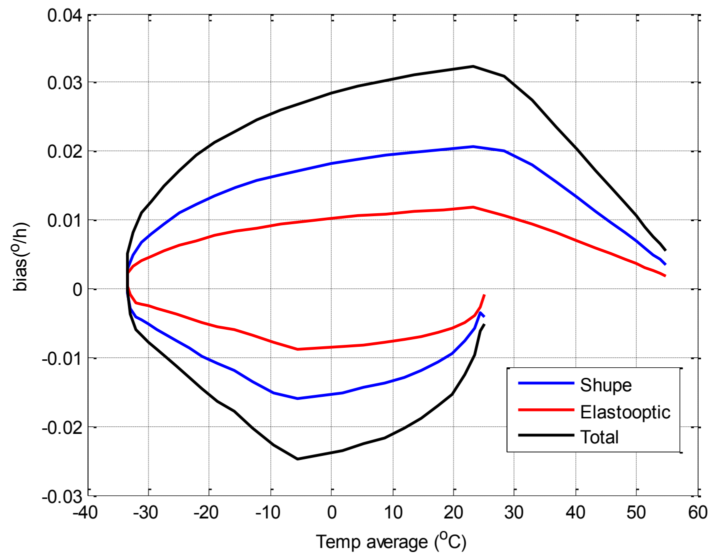

Figure 3.14: Bias error estimations vs the coil temperature.

A comparison of the bias error estimations is given in Figure 3.15. Bias errors are in the same order of magnitude, have the same sign, and trends are similar. Bias error of the reference model rapidly goes to a steady point while our model does not. This is due to the slower diffusion of the temperature for our model. The relatively slow temperature diffusion results in greater derivative and gradient for the temperature field.

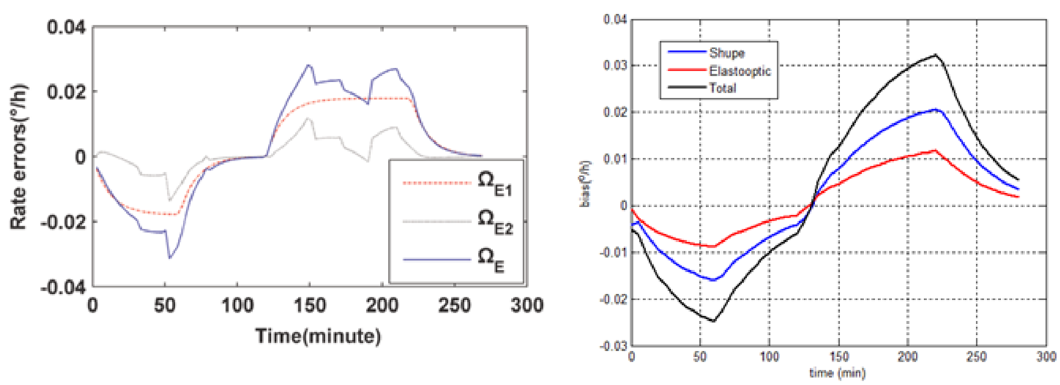

Figure 3.15: Bias error estimations. Reference [38] (left) and the simulation (right).

3.3 Advanced Modeling of the Fiber Coil

Classical modeling approaches give insight and valuable conclusions; however, an advanced model is needed for further analysis. We improved the model in two manners: Detailed thermo-mechanical interactions, and the definition of the winding pattern.

Latest approaches in the literature provide more reliable models [14], [39], [40], [41]. The fiber coil is modeled in two steps. The first one is the modeling of the representative volume element (RVE) of the fiber coil by the homogenization process. RVE includes the fiber core, cladding, coating, and adhesive. The second step is the combined model of the homogenous fiber coil defined by the RVE parameters, together with the spool and all other surrounding elements. This two-step approach provide much higher mesh resolutions for the boundaries inside the fiber while running the simulation long enough for thermal diffusion.

Secondly, trimming of the fiber coil is investigated. Quadrupole winding is used for reducing the thermal effects inside the fiber coil. However, the reduction may be decreased if the position of the midpoint of the fiber coil is changed from the ideal case. Midpoint position may shift during the winding of the fiber coil or splicing the phase modulator to the ends of the coil. That shift should be trimmed by shortening the one end of the fiber coil for better performance.

Thirdly, the definition of the quadrupole fiber coil is revised. The practical quadrupole is presented for a better representation of the fiber turn locations. The practical quadrupole is a practical solution for passing the fiber from a layer to the next one. It results in a non-ideal pattern of the quadrupole coil but eliminates the uncontrolled fiber portions between the layers. The pattern also includes the turn length difference between the layers. The model is validated by comparing the simulation results with a laboratory FOG setup.

3.3.1 Homogenization / Dehomogenization Procedure

Fiber coil consists of fiber turns, potting material between the turns, and a spool. Fiber itself consists of the core, cladding, and coating. Fiber coil structure, excluding the spool, is an anisotropic, but transversely isotropic composite material (Figure 3.16). The analysis is extended to the composite model for the temperature and stress field formations.

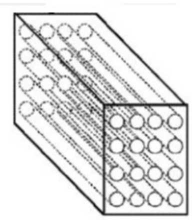

Figure 3.16: Fiber coil is a transversely isotropic composite material [39].

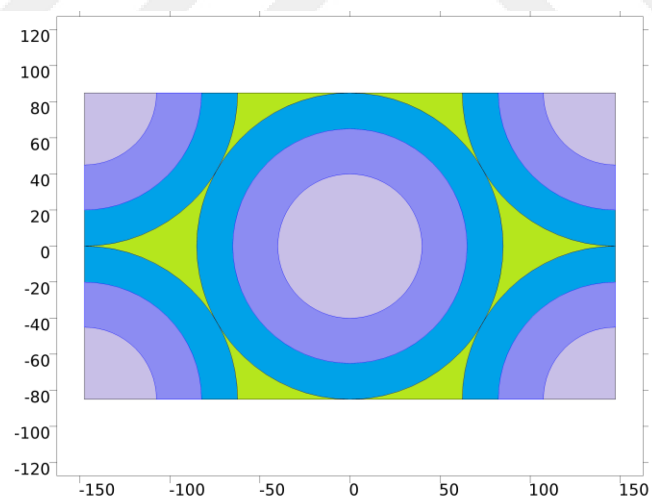

Figure 3.17: Fiber coil RVE. Fibers are located in an orthocyclic manner with adhesive in between. All dimensions are in µm.

Modeling of the whole fiber coil consists of two main steps. Fiber coil is taken as a composite material which is composed of the fiber core, cladding, coating, and adhesive material (Figure 3.17). A model of RVE is simulated (Figure 3.18) to identify the composite material properties. Simulation solves the composite material properties for an orthotropic homogeneous material by using the boundary conditions. A property set (Young's modulus, Poisson's ratio, thermal expansion coefficient, all in two dimensions, radial and axial) of an orthotropic homogeneous material representing the fiber coil is obtained. This first step is named homogenization.

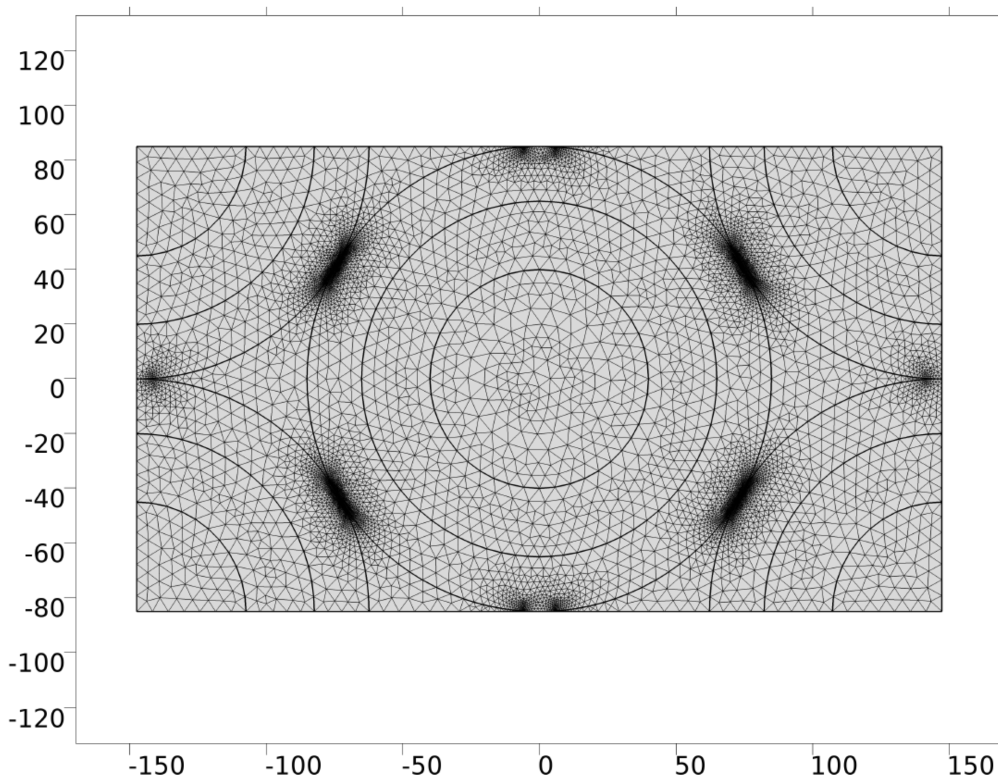

Figure 3.18: Simulation of RVE with high resolution meshed.

FEM simulation is reduced to three components, after the homogenization process: Fiber coil as an anisotropic composite material, spool as a homogeneous metal, and air as the surrounding environment. Temperature, stress, and strain fields are obtained by using FEM simulation. These macro-scale fields represent the thermo-mechanical interactions inside and between the spool, fiber coil and environment.

The dehomogenization process is carried, after obtaining macro-scale fields. In this process, macro strain fields are mapped to the micro fields. Temperature fields and strain fields at the macro-level results as radial and axial strains inside the fiber. These micro-level strains are used to calculate the bias error calculations.

$$\begin{pmatrix} \bar{\varepsilon}_{r,F} \\ \bar{\varepsilon}_{z,F} \end{pmatrix} = \begin{pmatrix} M_{rx} & M_{ry} & M_{rz} & M_{rT} \\ 0 & 0 & 1 & 0 \end{pmatrix} \begin{pmatrix} \bar{\varepsilon}_{xx} \\ \bar{\varepsilon}_{yy} \\ \bar{\varepsilon}_{zz} \\ \Delta T \end{pmatrix} \tag{3.26}$$

where $\bar{\varepsilon}_{r,F}$ and $\bar{\varepsilon}_{z,F}$, are the radial and axial strain fields inside the fiber,

M_{rx}, M_{ry}, M_{rz}, M_{rT}, are the transformation matrix elements,

and $\bar{\varepsilon}_{xx}$, $\bar{\varepsilon}_{yy}$, $\bar{\varepsilon}_{zz}$, are the macro-level strain fields in x, y, z axis respectively.

3.3.2 Coil Winding Pattern

Today, quadrupole and octupole patterns are the most widely used winding methods for tactical and higher grade FOGs. Quadrupole pattern is faster, easier to apply, and provides sufficient performance for many applications. On the other hand, the octupole pattern promises better performance in theory. However, the winding procedure must be undertaken carefully to prevent any non-homogeneity created during the winding.

FEM simulation provides the temperature and stress fields for each fiber turn and time step. Bias error is calculated by using the fields as given in Equation (3.21). In the equation, the parameter 'z' defines each turn's distance from the one end of the fiber loop so that each turn's location in two-dimensional plane must be specified for any type of winding geometry. A quadrupole pattern is given in Figure 3.7. Fiber turns are located in an orthocyclic manner, by which the fiber turns of each layer is located as close as possible to the next layer. This reduces the distance between the locations of the symmetric fiber portions and provides better thermal performance.

Passing the fiber from one layer to the next one, especially from the first layer to the fourth or from the third to the sixth, can be problematic in this pattern. Uncontrolled fiber segments, which are highly susceptible to thermal variations, between the layers exist. This issue can be solved by the practical quadrupole winding pattern (Figure 3.19). The first turn of each layer is wound either CW or CCW and the last turn vice versa. This practical solution for passing the fiber from one layer to the next one changes the locations of the fibers and creates an asymmetry in the axial direction of the coil.

All coil geometry calculations include turn length asymmetry and diameter asymmetry. These asymmetries arise from winding the fiber turns on top of each other. Inner layer turns are shorter and upper ones longer. Innermost and outermost layers have the length difference of (D-d)/π. This length difference changes the error equations in two manners. Firstly, the counter-propagating waves always travel in different layers of the coil, mostly in the next layer. That reduces the quadrupole performance. Secondly, as the Sagnac scale factor is a linear combination of the fiber length and the coil diameter, each layer's contribution to the bias shift is different from the other. The outermost layers are more sensitive to the rotation rate while the innermost layers less. That phenomenon is also added to the bias error calculation approach.

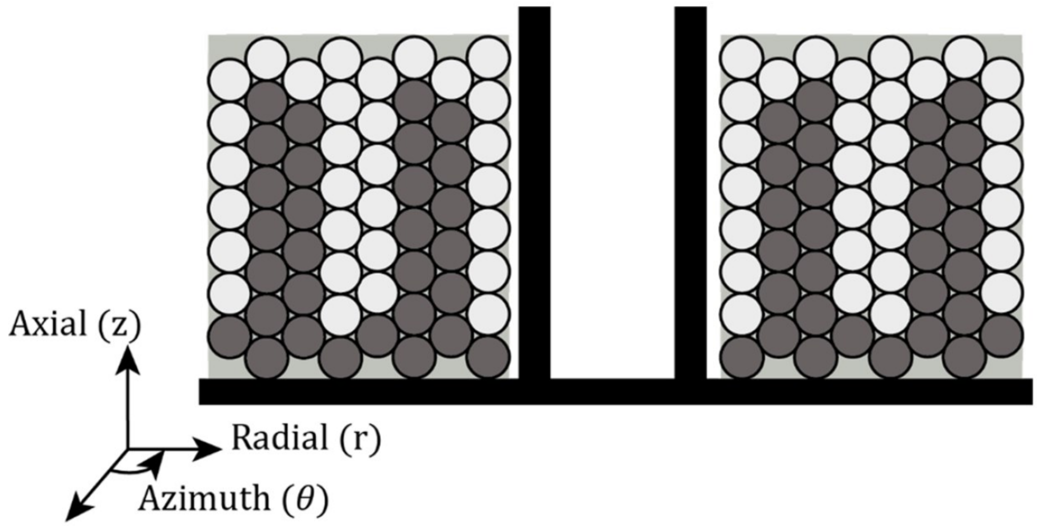

Figure 3.19: Practical Quadrupole Pattern.

3.3.3 Bias Error Calculation Approach

Equation (3.10) is discretized for the calculation of the bias error. The fiber coil is a cylindrical structure and the integral can be represented in radius, azimuth, and height (r,θ,z). Light travels only in the fiber core so that the integral is taken through the fiber core that is only continuous through the azimuth and discrete for axial and radial directions. Equation (3.10) is reduced into two dimensions and discretized.

$$\Omega_S(t) = \frac{n}{\pi N}\sum_{i=1}^{N_r}\frac{1}{{d_i}^2}\sum_{j=1}^{N_a}\int_0^{2\pi}\frac{\partial n}{\partial T}\dot{T}\left(r_i,\theta,z_j,t\right)(L-2s)d\theta\,\Delta s \qquad (3.27)$$

where d_i is the diameter of each turn, N_r, N_a are the radial and axial layer numbers, respectively, and $N = N_r \times N_a$ is the total number of turns. Using the relation $\Delta s = \frac{L}{N} = \frac{\pi d_i N}{N} = \pi d_i$, and taking the integral over $d\theta$ results as,

$$\Omega_S(t) = \frac{n}{N} \sum_{i=1}^{N_r} \frac{1}{d_i} \sum_{j=1}^{N_a} \frac{\partial n}{\partial T} \dot{T}(r_i, z_j, t)(L - 2s - l_i) \tag{3.28}$$

where l_i is the length of each fiber turn that is different for every radial layer. This equation is the two-dimensional approximation for the calculation of the bias error due to temperature fluctuation.

3.3.4 Simulations and Results of the Advanced Model

3.3.4.1 Modeling of a Laboratory FOG Coil

A laboratory FOG coil proposed to be navigation grade with 9 cm diameter and 1100 meter length (Table 3.4) is modeled. FEM simulation is built for obtaining the temperature and strain fields. The model consists of the homogenized fiber coil which is wound on a spool, air surrounding the coil, and heat source encapsulating the air (Figure 3.20). Heat source provides a temperature profile ranging from -40 °C to 60 °C. FEM simulation calculates the heat flow according to the material properties of the spool and coil.

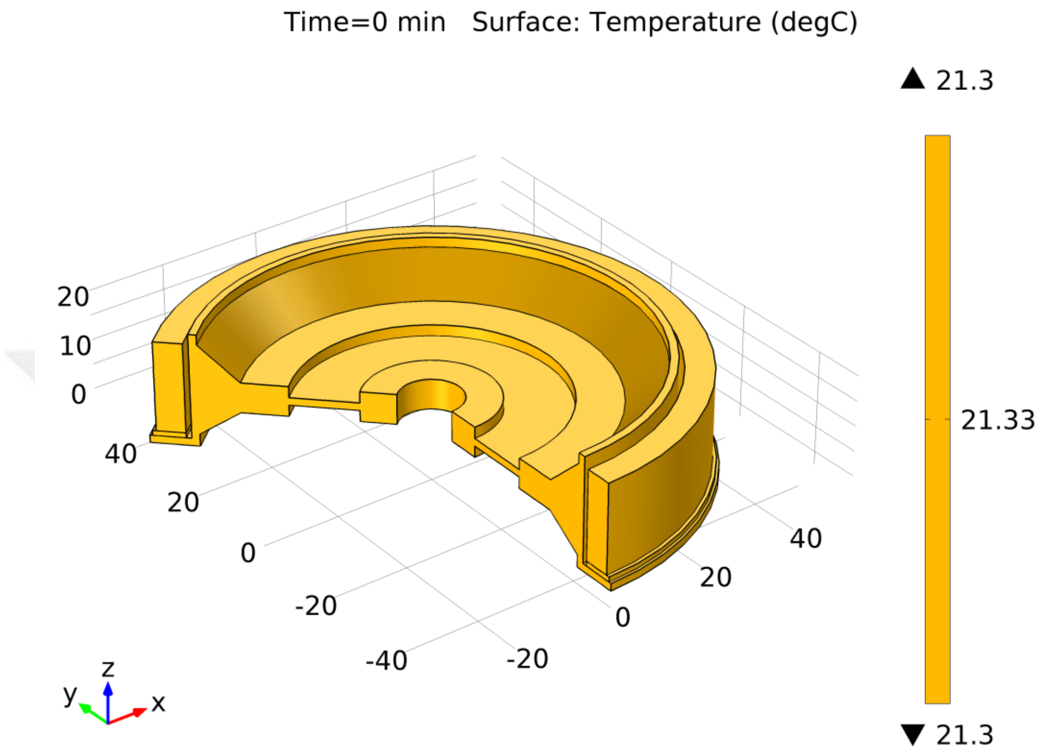

Figure 3.20: FEM model of the fiber coil.

Table 3.4: Coil parameters

Fiber length (m)	1101
Number of winding layer	36
Number of loops per layer	106
Inner diameter of the coil (mm)	87.00
Outer diameter of the coil (mm)	97.65
Coil height (mm)	18.02

Fiber coil structure is homogenized by defining RVE and calculating the composite material properties by using the boundary conditions as described in Part 3.3.1. Calculated parameters for the design are given in Table 3.5.

Table 3.5: Coil parameters obtained by homogenization

Parameter	Direction	Value
Elastic moduli	E_z (GPa)	14.5
	E_r (MPa)	95.2
	G_{zr} (MPa)	24.1
Poisson's ratio	ν_{zr}	0.392
	ν_r	0.979
	ν_{rz}	0.003
Thermal expansion coefficient	α_z ($\times 10^{-6}/K$)	3.36
	α_r ($\times 10^{-6}/K$)	193
Thermal conductivity	k_z (W/mK)	0.51
	k_r (W/mK)	0.34

FEM simulation outputs macroscopic temperature and strain fields. Strain fields inside the core are calculated by the dehomogenization process. Transformation matrix elements are obtained along with the homogenization process. Calculated matrix elements are given in Table 3.6.

Table 3.6: Dehomogenization parameters

M_{rx}	2.74×10^{-6}
M_{ry}	2.70×10^{-6}
M_{rz}	-0.17
M_{rT}(1/K)	9.98×10^{-6}

Input temperature profile given in Figure 3.21 spans a range from -40 °C to +60 °C for both increasing and decreasing cases of the temperature. This profile reveals all temperature and temperature time derivative dependent errors in the interval.

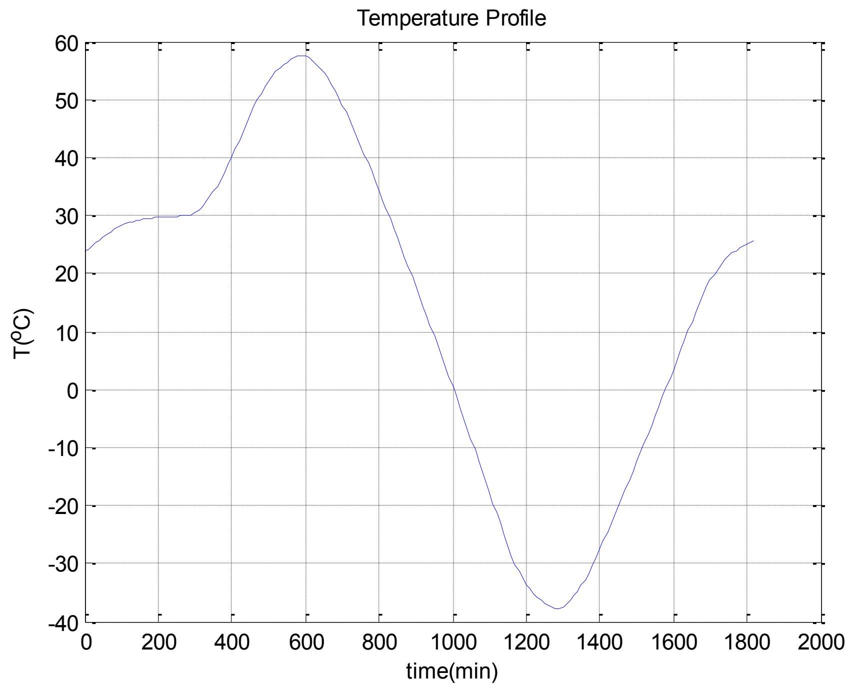

Figure 3.21: Input temperature profile is obtained from the laboratory experiments.

The temperature and derivative of the temperature versus time for each fiber turn through the coil are given in Figure 3.22 and Figure 3.23, respectively. From the graphs, it is seen that the gradient along fiber turns is much slower than the derivative with respect to time. In other words, the temperature is diffused through the fiber coil much faster than the temperature change for this scenario.

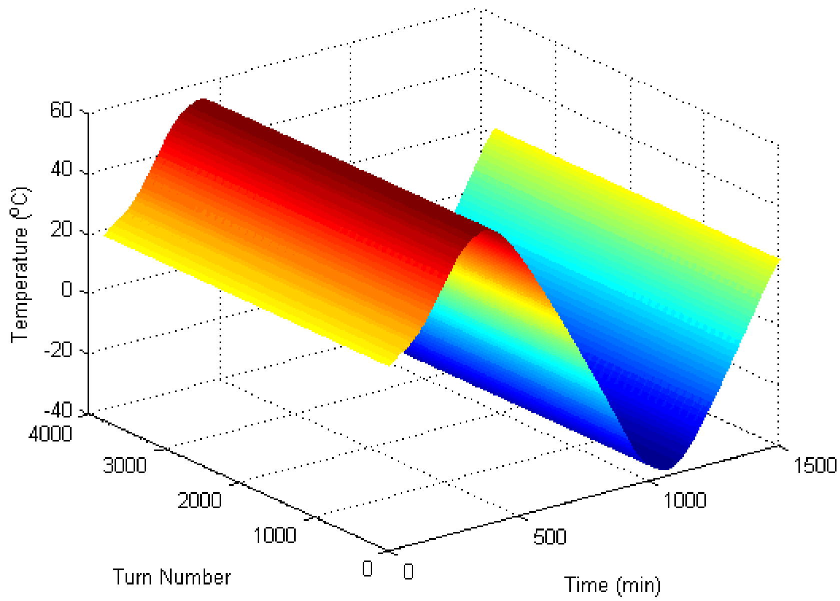

Figure 3.22: Temperature distribution through the fiber coil.

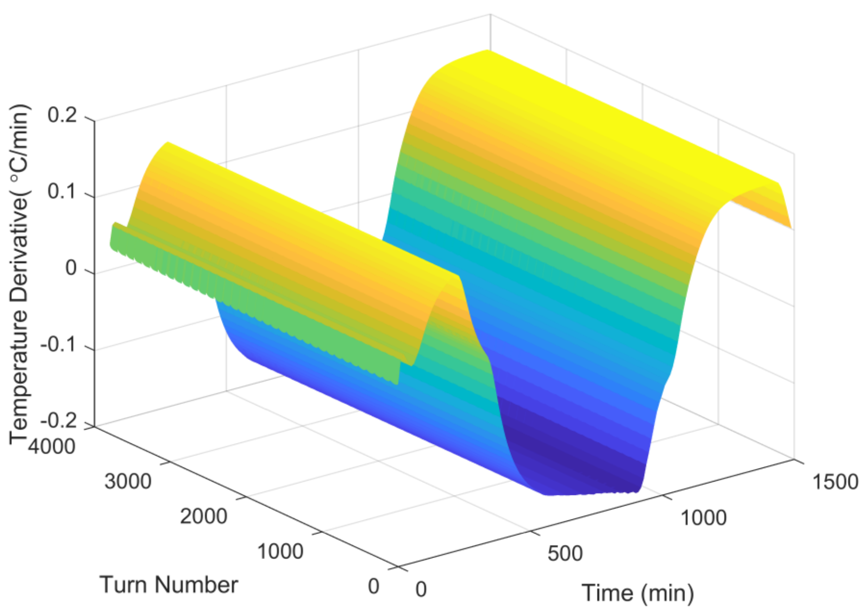

Figure 3.23: Temperature derivative distribution through the fiber coil.

Microscopic strain fields obtained after the dehomogenization are given in Figure 3.24 and Figure 3.25. The time derivatives of the fields are used in the calculation of the elastooptical bias error. From the figures, it can be seen that the stress distribution differs from the temperature distribution, that the gradient in the stress is higher than the time derivative.

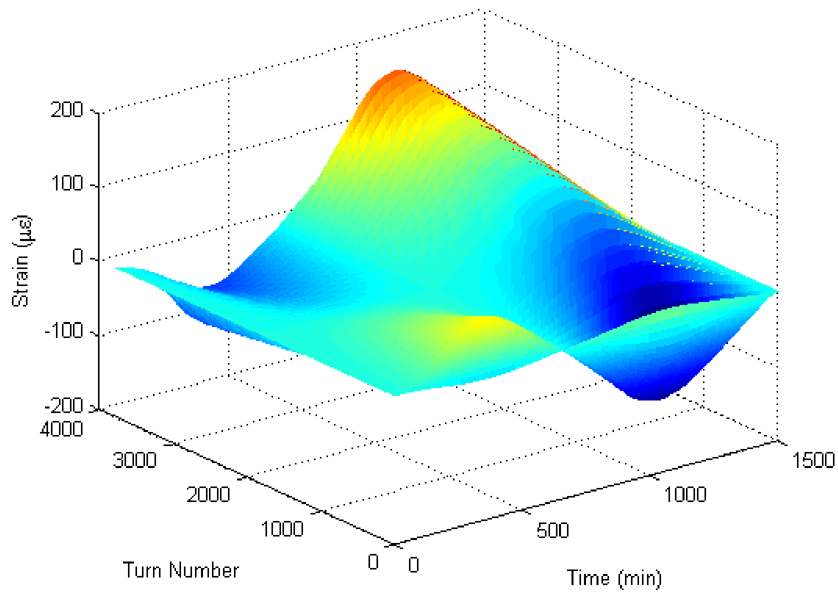

Figure 3.24: Strain (radial) distribution through the fiber coil.

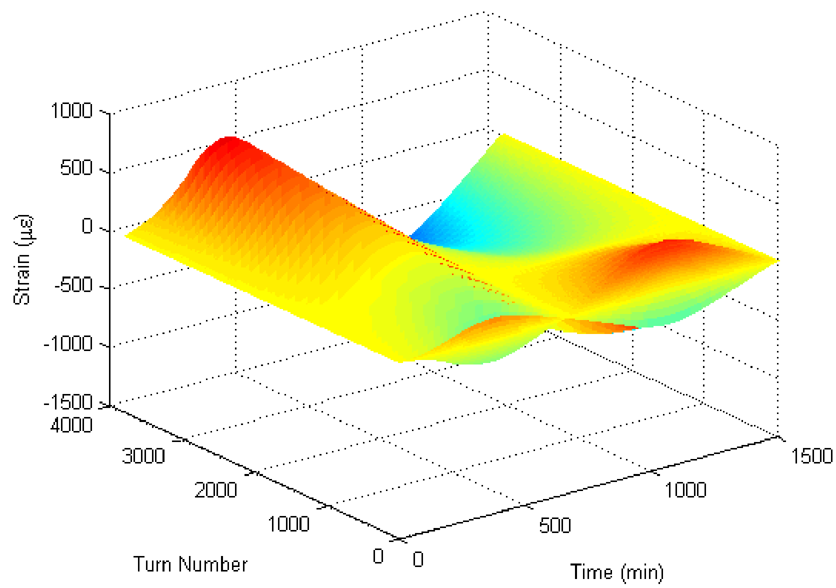

Figure 3.25: Strain (axial) distribution through the fiber coil.

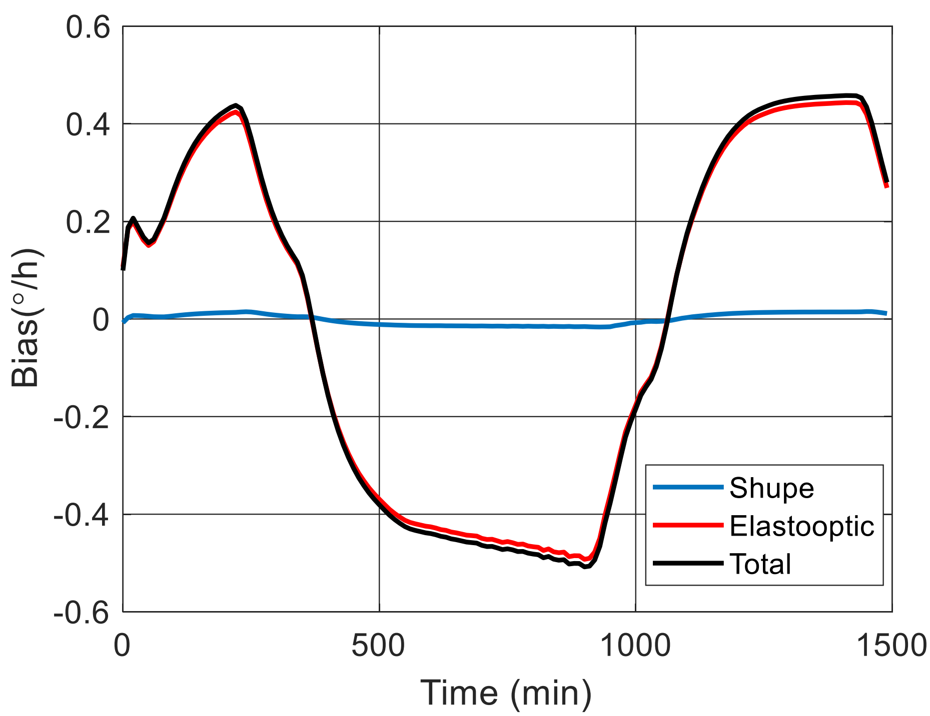

Figure 3.26: Bias error estimations.

Lastly, bias estimations are calculated (Figure 3.26). Coil temperature starts to decrease beginning from the room temperature to -40°C, turns to increase up to +55°C, and again returns to room temperature. Coil visits all temperatures twice. While the temperature is decreasing, the bias error is positive, and in the increasing part vice versa. The pure Shupe effect is negligibly small with respect to the elastooptic effect, which is contrary to the result obtained in Part 3.2.3.

3.3.4.2 Experiments

A closed-loop FOG setup is built for laboratory experiments (Figure 3.27). This setup consists of one ASE light source, two MIOC - fiber coil pairs, and digital and analog electronic boards. The setup is placed in a temperature chamber during temperature tests. Temperature sensors are mounted on each coil spool to monitor the coil temperature.

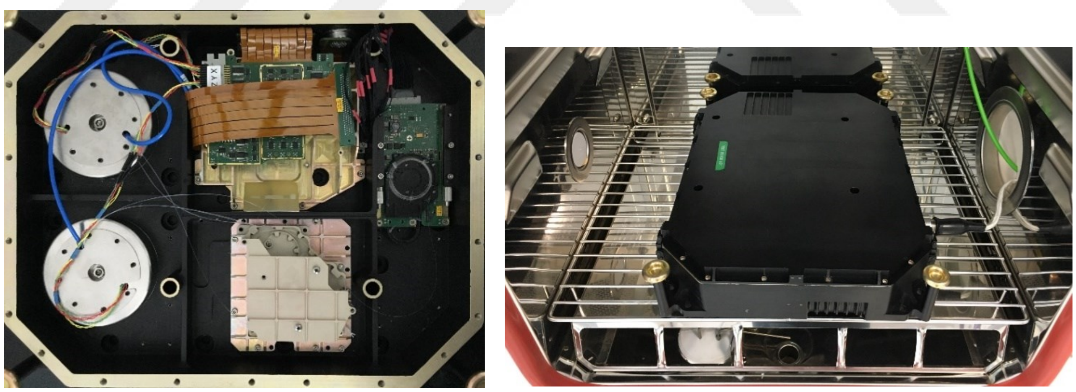

Figure 3.27: Setup for FOG thermal sensitivity experiments.

Experiments are carried with three fiber coils having the same design parameters as in simulations. Temperature profile ranging from -40 °C to +60 °C is applied to the fiber coils while temperature and rotation rate measurements are collected. Collected rotation rate data is processed to eliminate the earth rotation and gyro noise. Collected FOG data and simulation results are plotted in Figure 3.28. Calculated temperature derivative sensitivity coefficients are given in Table 3.7.

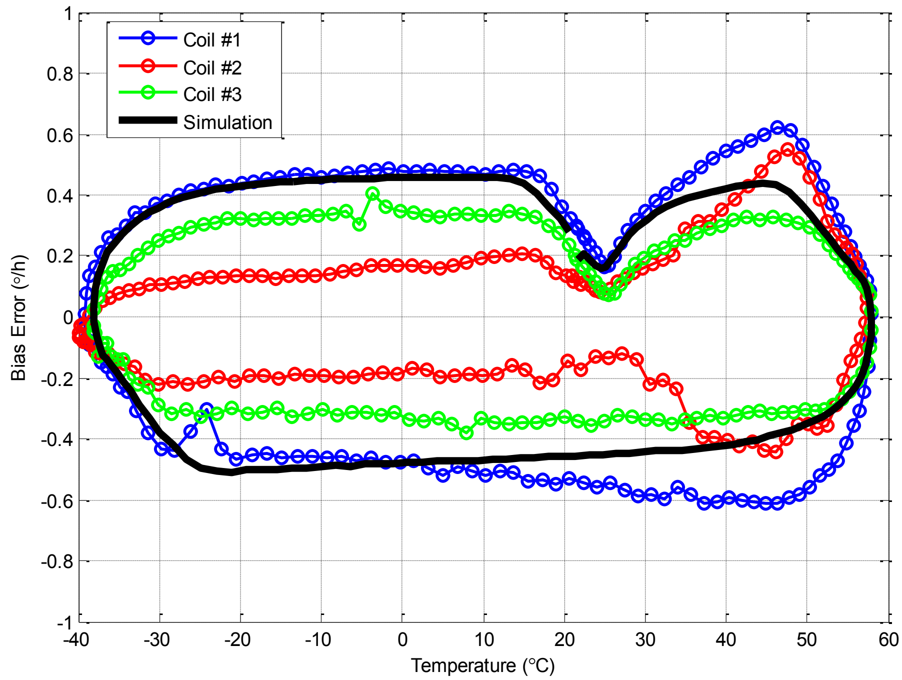

Figure 3.28: Bias error measurements and simulation estimation vs fiber coil temperature.

Table 3.7: Temperature derivative sensitivity coefficients

Coil No	***Sensitivity Coefficient (°/h / °C/min)***
Coil #1	3.01
Coil #2	1.39
Coil #3	1.98
Theoretical Model	2.71

Bias error characteristics for three fiber coils are consistent with the theoretical model. The difference between the sensitivity coefficients of the coils could be a result of fiber tail length asymmetry during the production of coils. Also, a change in the amount of adhesive during the production could be another reason. It is also seen that the sensitivity coefficients of Coil #1 and Coil #2 change for different temperatures. This phenomenon is called as the racket effect.

3.3.5 Trimming

3.3.5.1 Background

Integral in Equation (3.21) converges to zero at z = L/2, which is the midpoint of the fiber coil. The equation is symmetric around the midpoint that the similar temperature derivatives through the coil at symmetric fiber segments cancel each other. However, in practice, the coil could not be wound perfectly symmetric and the position of the midpoint could change (Figure 3.29). Midpoint position may shift during the coil manufacturing or the splicing of the phase modulator to the ends of the fiber coil.

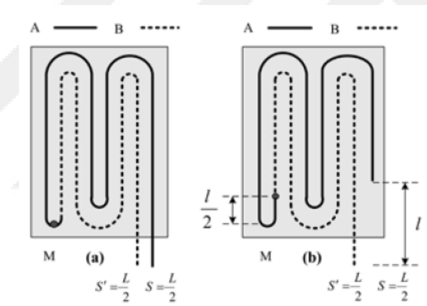

Figure 3.29: (a) Perfect trimming case for quadrupole winding (b) imperfect case, the position of the midpoint is changed [42].

If the position of the midpoint is changed, the symmetry defined by the quadrupole degrades. That results in an asymmetry for both radial and axial derivatives. Reference [42] defines a new parameter called pointing error thermal sensitivity, γ_T, of the coil and gives a direct proportion to coil asymmetric length.

$$\gamma_T = \gamma(\frac{L}{N^2} - \frac{N-1}{N} l_{eff}) \tag{3.29}$$

where N is the layer number,

L is the total length of the fiber coil,

$\gamma = \frac{n}{2D}\frac{\delta n}{\delta T}$,

and l_{eff}, is the effective turn length asymmetry.

It is also stated that for a quadrupole coil, there exists an intrinsic trimming length which should be trimmed also for a perfectly wound one. This intrinsic asymmetry zeroing Equation (3.29) has the solution,

$$l_{eff} = \frac{L}{N(N-1)} \tag{3.30}$$

For 24 turn layer, 1000 m length fiber coil this ratio stands for 1.8 meters of fiber to be trimmed.

3.3.5.2 Trimming Simulations

Trimming can be implemented by subtracting (or adding) some fiber portion from one end of the fiber coil. This process also changes the total length, so that the midpoint position changes half of the subtracted fiber length. We present the discrete trimming approach for the simulations by subtracting one or more fiber turns completely from the simulation. The total fiber length is shortened, which changes the limits of the Shupe integral and the Sagnac scale factor. Subtracted fiber turn is not calculated as a bias source, i.e. all thermal variation and stress effects on top of that fiber turn are ignored, however, it continues to be a part of the fiber coil simulation creating stress on the rest of the fiber turns. The last one can be counted as a drawback of this approach. The second drawback is that the minimum trim length is one turn length.

Two different coil geometries are used for the simulations (Table 3.8). Simulation results are calculated for different trim lengths, for each coil design. Elastooptic, pure Shupe, and total bias errors are plotted with respect to each trimming step. Trimming is applied to the fiber turns at the outermost layer, which is way more applicable than any other coil part.

Table 3.8: Coil parameters for trimming simulations

	Coil Design #1	Coil Design #2
Fiber length (m)	1101	1101
Number of winding layer	56	36
Number of loops per layer	77	106
Inner diameter of the coil (mm)	73.00	87.00
Outer diameter of the coil (mm)	89.53	97.65
Coil height (mm)	13.09	18.02

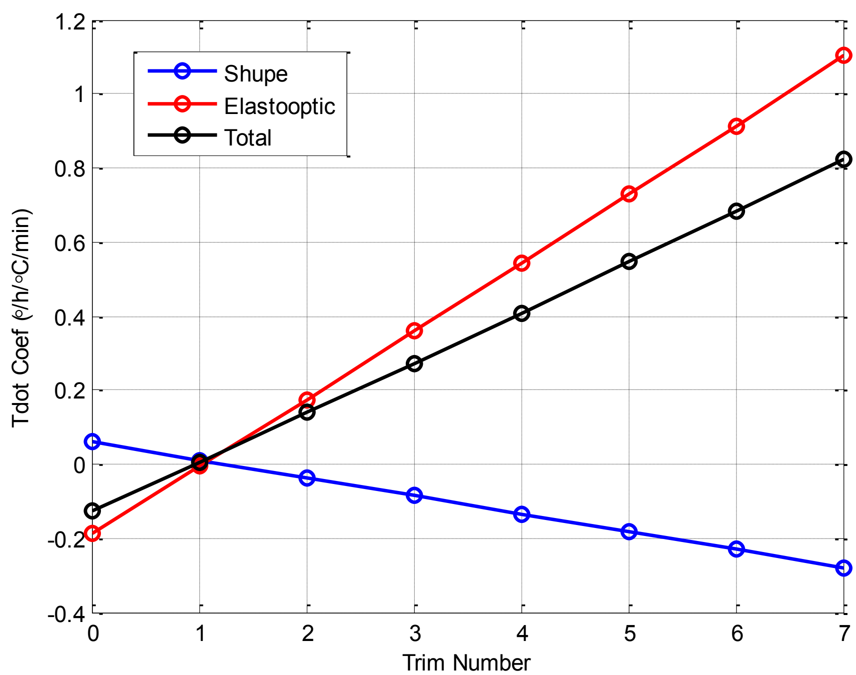

Figure 3.30: Trimming results for Coil Design #1, with ideal quadrupole pattern.

It is seen from Figure 3.30 that one trim turn gives the optimum solution for Coil Design #1 with ideal quadrupole. In that point, the pure Shupe error, elastooptic error, and total error become zero. Theoretical optimum Shupe trim point is calculated as 35 cm by using Equation (3.30) with Coil Design #1 parameters, where the simulation result is 1 turn, which is 26 cm. It is concluded that they are consistent especially in the order of magnitudes.

Optimum trim point shifts to 4 turns for the practical quadrupole case, given in Figure 3.31. Although the characteristic of the pure Shupe error does not change, the elastooptic error becomes larger and its trim point is optimum somewhere between 3 and 4 turns. This shift is due to the axial asymmetry because of the practical winding technique.

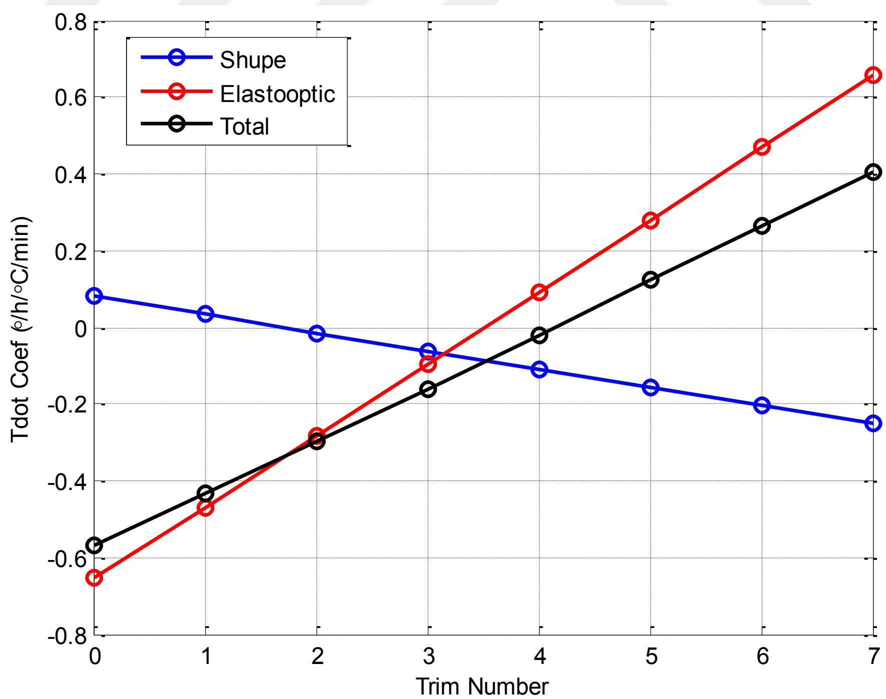

Figure 3.31: Trimming results for Coil Design #1, with practical quadrupole pattern.

Figure 3.32 gives the results of Coil Design #2 for the ideal quadrupole winding pattern. It is seen that Coil Design #2 has an optimum trim point far away with respect to Coil Design #1. That difference arises as Coil-2 has lesser radial layers, 56 vs. 36 layers. Increasing the radial layer number reduces the quadrupole errors and decreases the intrinsic trim length. Theoretical optimum Shupe trim point is calculated as 2 meters by using Equation (3.30) for Coil Design #2. We found this point as 7 turns which corresponds to 1.8m. It is concluded that they are consistent in the order of magnitudes.

Lastly, the practical quadrupole pattern for Coil Design #2 results are given in Figure 3.33. It is seen that the elastooptic error characteristic has a major change while the pure Shupe error shows none. The elastooptic error increases as the trim length increases. So the optimum coil trim length should be on the other side of the graph, which means that the other end of the fiber coil should be trimmed. This could be problematic during the application of the trimming as the other end of the fiber turns may not be accessible after the production of the fiber coil (Figure 3.19).

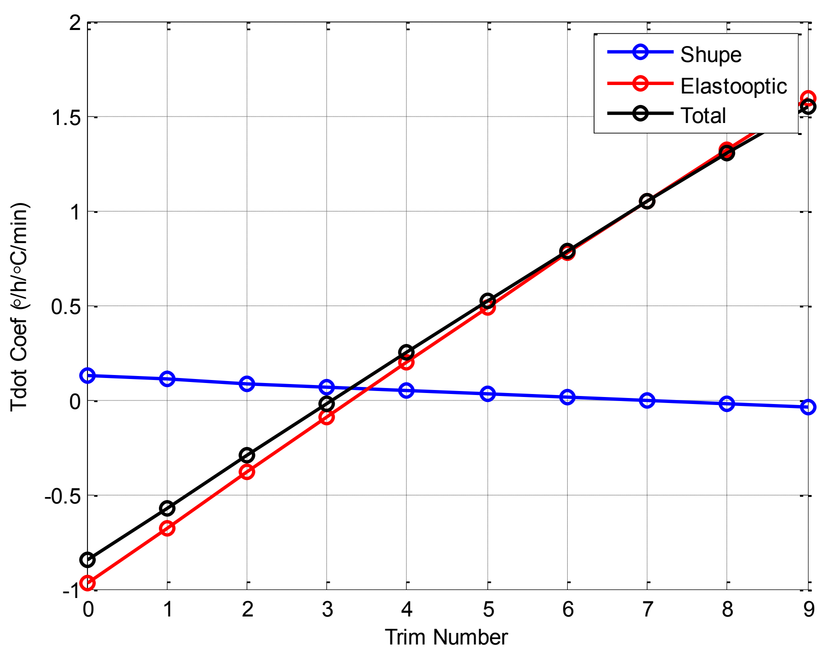

Figure 3.32: Trimming results for Coil Design #2, with practical ideal pattern.

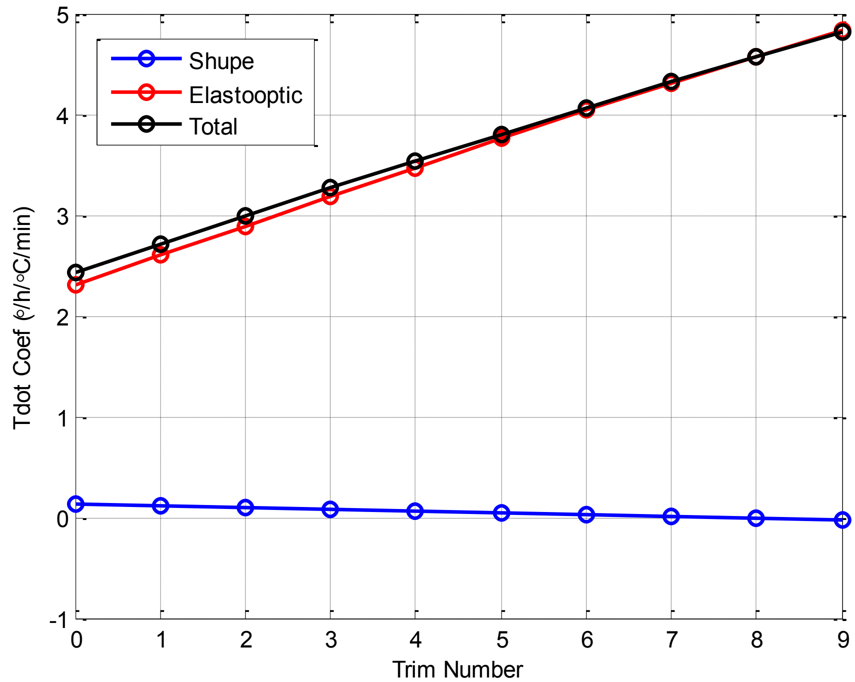

Figure 3.33: Trimming results for Coil Design #2, with practical quadrupole pattern.

3.4 Strain Distribution through the Coil

This chapter is a reproduction of Reference [45].

3.4.1 Strain Analysis Approach

In Chapter 3.3.4, it is concluded that the elastooptic effect is much stronger than the pure Shupe error for that coil design. Thermally induced stress/strain is the source of the elastooptical bias error. Several works in the literature indicate the relation between the stress/strain and the bias error and try to reduce the total stress/strain as a whole [40], [41]. This approach is effective up to a point. The discussion in this chapter is that the reduction of the bias error by controlling the strain distribution through the fiber coil, although the total stress is not reduced significantly.

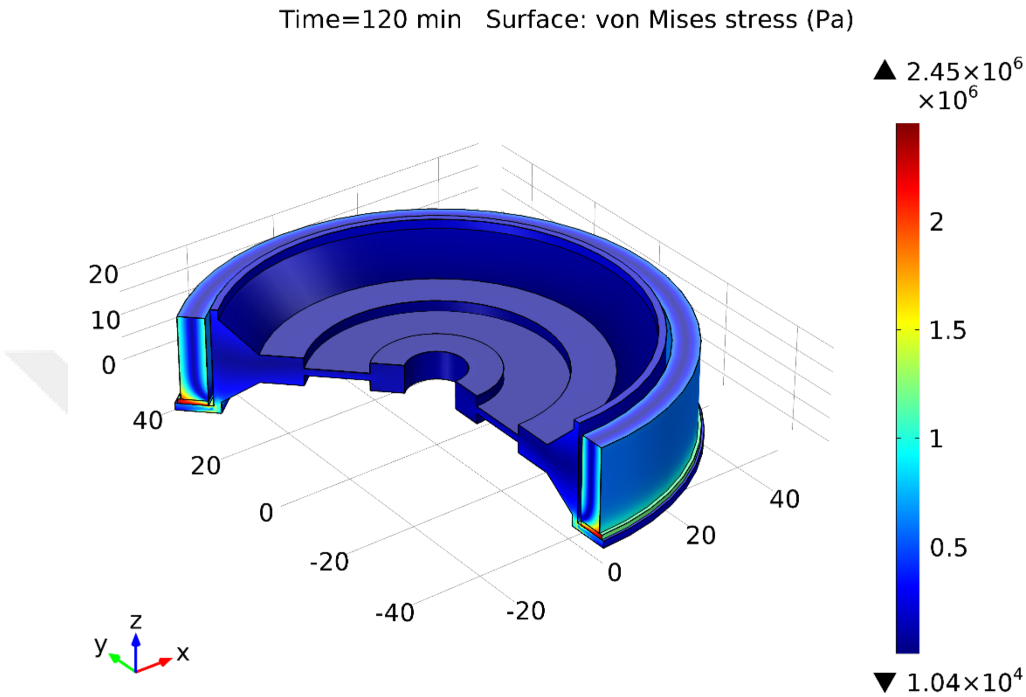

Figure 3.34: FEM simulation of the fiber coil model. Fiber coil dimensions are in mm. High stress region is in the coil spool intersection.

Figure 3.34 shows the von Mises stress distribution through the model for a time instant of the simulation. The highest stress is located in the intersection area of the fiber coil, which is modeled as a homogeneous composite material, and the spool. Different thermal expansion coefficients of the materials result in a high stress in the intersection area. Figure 3.35 shows the von Mises stress distribution for each fiber turn with respect to time. Temperature changes as time progresses and the von Mises stress increases dramatically for the highest and lowest turn numbers, which are located in the intersection area.

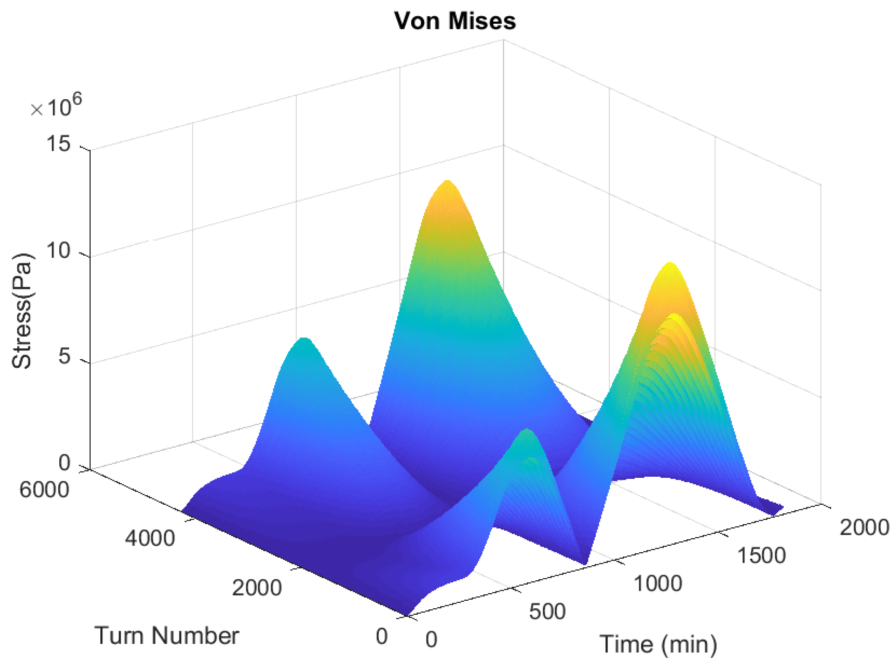

Figure 3.35: Stress distribution through the fiber coil. Temperature changes as time progresses.

In order to analyze the effect of the stress, we designed a new fiber coil without spool and with a titanium spool. Stress values are obtained from the model and given in Table 3.9. Although the von Mises stress characteristics and values stay the same, the bias error is significantly reduced. The stress/strain inhomogeneity in the fiber coil and the bias error calculations are significant.

Table 3.9: Von Mises stress values for different spool materials

Spool Material	Maximum Von Mises Stress (Pa)	Average Von Mises Stress (Pa)
Aluminum	1.34×10^7	2.15×10^6
Titanium	1.32×10^7	2.14×10^6
No spool	1.31×10^7	2.14×10^6

The elastooptical error is separated into two main sources: Error due to the elongation of the fiber (Ω_{EOl}) and error due to refractive index change (Ω_{EOn}). Both of the error sources are discretized as in Equation (3.28).

$$\Omega_{\mathrm{EO}}(t) = \Omega_{\mathrm{EOl}}(t) + \Omega_{EOn}(t) \tag{3.31}$$

$$\Omega_{EOl}(t) = \frac{n^2}{N}\sum_{i=1}^{N_r}\frac{1}{d_i}\sum_{j=1}^{N_a}\dot{\varepsilon}_f(r_i, z_j, t)(L - 2s - l_i) \tag{3.32}$$

$$\begin{aligned}\Omega_{EOn}(t) = -\frac{n^4}{2N}\sum_{i=1}^{N_r}\frac{1}{d_i}\sum_{j=1}^{N_a}\big[p_{12}\dot{\varepsilon}_f(r_i, z_j, t)\\ + (p_{11} + p_{12})\dot{\varepsilon}_p(r_i, z_j, t)\big](L - 2s - l_i)\end{aligned} \tag{3.33}$$

3.4.2 Simulations

The simulation environment is a powerful tool to obtain information about the interactions that cannot be measured directly, inside the fiber coil, like strain distribution, the dominant bias error source, or thermal sensitivity. Firstly, various bias error contributions of a model with the parameters of Coil Design #1 (Table 3.10) are obtained by simulations. Then, the strain inhomogeneity is presented for different spool types. Lastly, the simulations of two more coil designs are presented.

All simulations are run with an input temperature profile that spans a range from -40°C to +60°C while the temperature is increasing and then decreasing with a rate of 0.2°C/min.

Table 3.10: Coil design parameters for strain analyses

	Coil Design #1	Coil Design #2	Coil Design #3
Fiber length (m)	1101	1101	1101

Number of winding layer	36	56	56
Number of loops per layer	106	77	77
Inner diameter of the coil (mm)	87.00	73.00	73.00
Outer diameter of the coil (mm)	97.65	89.53	89.53
Coil height (mm)	18.02	13.09	13.09
Spool material	Aluminum	Aluminum	Titanium

3.4.3 Elongation vs. refractive index change

The different error contributions of Coil Design #1 are shown in Table 3.11, wherein the pure Shupe error is much smaller than the elastooptical error. Secondly, the elongation of the fiber dominates the elastooptical error. Although the error due to a refractive index change has a negative sign, it is not large enough to compensate for the error due to elongation. It is a significant conclusion that the strain through the fiber propagation axis is more significant than the perpendicular strain inside the fiber so the change of the strain through the fiber propagation axis ($\dot{\varepsilon}_f$) should be reduced. We mainly deal with the strain through the fiber propagation axis so it is hereinafter referred to as “strain”.

Table 3.11: Error contributions

Parameter $\left(\frac{°/h}{°C/min}\right)$	Coil Design #1	Coil Design #2	Coil Design #3
Shupe	0.0847	0.0790	0.0790
Elastooptical (EO) Error	2.62	1.06	-0.398
EO error due to refractive index change	-0.594	-0.273	0.110

EO error due to elongation	3.30	1.34	-0.508
Total	2.70	1.14	-0.319

3.4.3.1 Strain inhomogeneity

Equation (3.32) shows that a fiber coil subjected to temperature fluctuation results in a gyroscope bias error if the strain through the fiber changes and the strain change rate is inhomogeneous. A simulation output, as shown in Figure 3.36, shows the strain distribution through the fiber coil while the temperature is fluctuating. This strain field can be studied in two dimensions: The total strain change with respect to time, and the distribution of the strain change rate, i.e. the thermal expansion coefficient, for each fiber turn.

The integral through the fiber turn number gives the total strain in the fiber coil at each time interval. The total strain change with respect to temperature is plotted in Figure 3.37 (a). A fiber coil in the laboratory is subjected to a temperature change from -40°C up to +60°C and the flight time inside the fiber coil is measured continuously with an optical time-domain reflectometer (OTDR). The flight time includes the fiber refractive index change due to temperature which is compensated by using the coefficient. Refractive index change is found to be $7 \times 10^{-6}\ ℃^{-1}$ which is close to the temperature coefficient of the refractive index for fiber core material, $10^{-5}\ ℃^{-1}$.

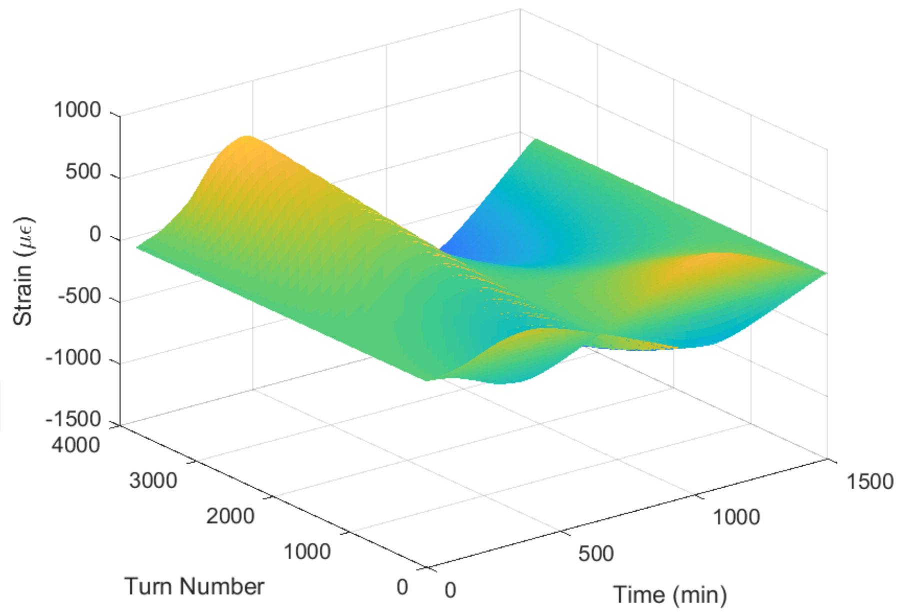

Figure 3.36: Strain (through the fiber propagation axis) distribution with respect to time and the turn number.

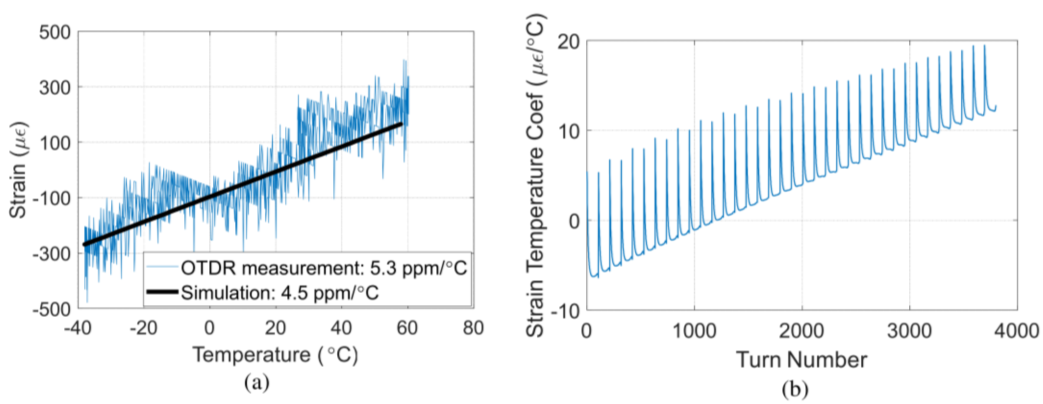

Figure 3.37: (a) Total strain change of the fiber coil. Simulation output for each temperature point is compared with the OTDR measurement of a fiber coil. (b) Calculated strain temperature coefficient for each turn number.

Distribution of the strain change rate can be obtained by calculating the temperature coefficient for each fiber turn. Strain temperature coefficient versus turn location, as shown in Figure 3.37 (b), is a serrated line where the serration indicates the axial strain and the line indicates the radial strain. The strain coefficients of each turn in the same radius are averaged and named as the axial strain coefficients (α_a), and the brackets indicate averaging over all t. This gives the inhomogeneity in the fiber coil in the axial direction.

$$\alpha_a(z_j) = \frac{1}{N_r}\sum_{i=1}^{N_r}\langle\dot{\varepsilon}_f(r_i, z_j, t)\rangle \tag{3.34}$$

A similar method is carried out in order to obtain the radial strain coefficients:

$$\alpha_r(r_i) = \frac{1}{N_a}\sum_{j=1}^{N_a}\langle\dot{\varepsilon}_f(r_i, z_j, t)\rangle \tag{3.35}$$

Radial strain temperature coefficient change is a straight line, while the axial strain coefficients show an asymmetric characteristic (Figure 3.38). A quadrupole pattern dictates the location of the fiber turns in order to be placed next to each other. Therefore, the symmetric strain distribution is important to reduce the total bias error. Although the value of the radial coefficient change is higher than the axial coefficient, the asymmetry of the axial distribution is the main bias error source. The asymmetric and rapid change in the axial coefficients of the inner layers results in a bias error, which is not compensated by the symmetric fiber turns.

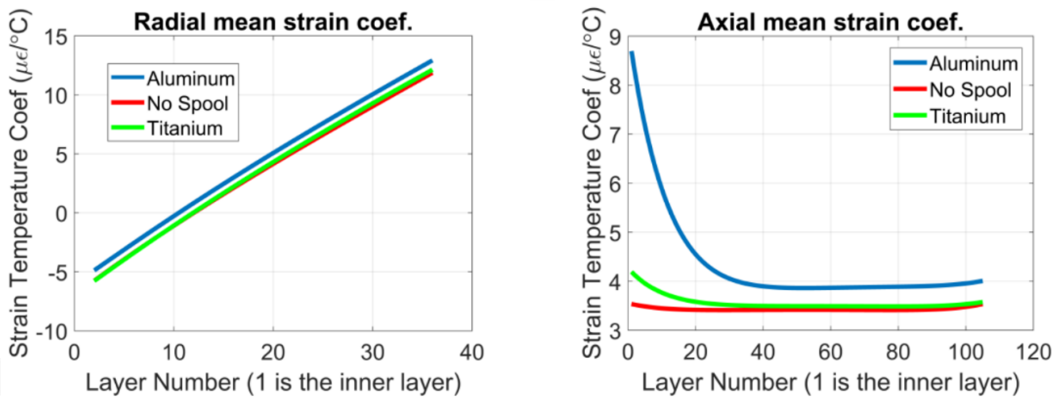

Figure 3.38: Radial and axial mean strain temperature coefficients for different spool configurations.

The calculations for two other simulations of the fiber coil, with a titanium spool and without a spool cases, are shown in Figure 3.38. The radial strain coefficients do not differ too much for different spool configurations. The axial strain coefficients are reduced, especially for the innermost layers. Titanium spool performs nearly as well as the no spool configuration.

The bias error contribution of the axial asymmetry can be reduced by changing the design of the fiber coil cross-section. Coil Design #2 has a fiber coil with a cross-section that looks more like a square (Table 3.10) to balance the bias error contribution of the asymmetries (Figure 3.39). The significant reduction in the axial strain coefficients reduces the bias error although the asymmetry in the radial strain coefficient increases. The new coil design is smaller than the existing one. A better bias error performance is achieved, although the smaller coil results in a 12% reduction in the Sagnac scale factor (Table 3.11). Simulations show that the main bias error contribution is still the elastooptical error due to elongation. The Shupe error stays nearly the same.

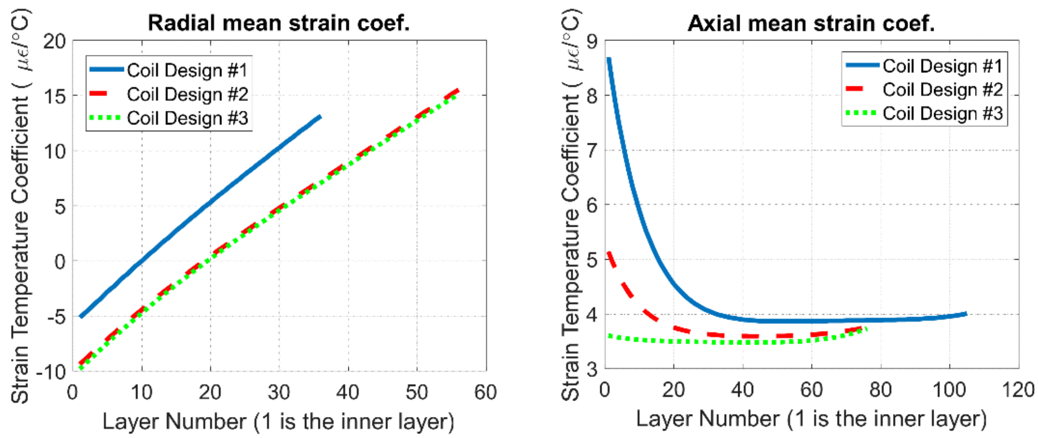

Figure 3.39: Radial and axial mean strain temperature coefficients for Coil Design #1, 2, and 3.

Further improvement can be achieved by changing the spool material. Aluminum is a widely used material because of its low cost and abundant usage in mechanical fabrication. Titanium is a more convenient material for high performance fiber coil design. The titanium thermal expansion coefficient is closer to the fiber itself than the aluminum. The third fiber coil design is presented with the same cross-section of the second design but with a titanium spool (Table 3.10). Simulations show that the axial strain coefficient asymmetry is reduced without any significant change in the radial asymmetry (Figure 3.39). Coil Design #2 and 3 have more radial layers and fewer axial layers than Coil Design #1. Change in the spool material reduces the axial asymmetry, while almost does not affect the radial. The elastooptical error is reduced more than sixfold relative to the first coil design, changes the sign, and becomes the inverse of the Shupe error (Table 3.11). The Shupe error stays nearly the same as in the second coil design. Shupe error and the elastooptical error cancel each other so that the total bias error is less than one-eighth of the first coil design.

3.4.3.2 Experiments

A FOG coil is produced with the parameters of Coil Design #3 for the validation of the simulation outcomes. The closed-loop FOG setup defined in Chapter 3.3.4.2 is used for the laboratory experiments. The setup is placed in a temperature chamber and a temperature profile ranging from -40°C to +60°C with temperature rates of ±0.2°C/min is applied to the fiber coil. The mean value of the collected data is subtracted to eliminate the earth rotation rate. A one-minute averaging filter is applied to data to filter out the gyroscope noise. Collected FOG data and the simulation results are plotted in Figure 3.40 along with the calculated temperature sensitivity coefficients. Bias error correlates mostly with the time derivative of the temperature so that the thermal sensitivity of the fiber coil is calculated with respect to it. The bias error characteristic of the FOG is shown to be highly consistent with the theoretical model.

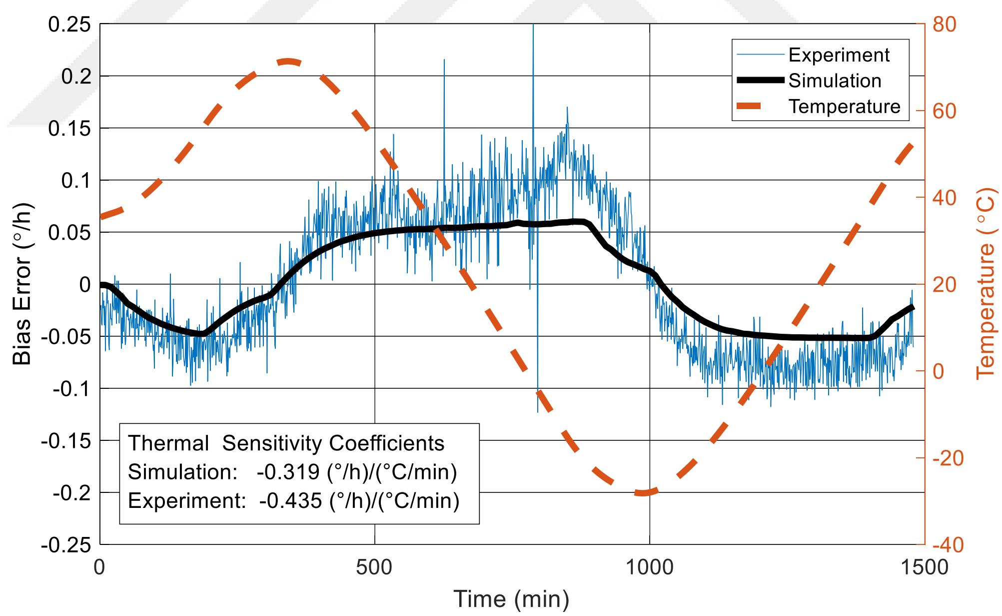

Figure 3.40: Simulated and experimental bias error curves.

Bias error can be decreased more than eightfold by reducing the strain inhomogeneity although the total stress on the fiber coil stays nearly the same. Two more conclusions can be very useful for the thermal modeling of a FOG coil: The elastooptical error is the dominant effect relative to the pure Shupe error, and the bias error due to elongation is greater than the refractive index change.

CHAPTER 4

VIBRATION ERROR

In this chapter, a modeling approach to the bias error due to the optical power fluctuation under vibration is presented. The interference and square wave modulation/demodulation equations are reviewed. Error equations are derived for optical power disturbances and rotation rate inputs. It is shown that optical power fluctuations result in bias error and also Shupe like error. Optical power fluctuation is estimated by using the closed-loop model output and the bias shift. In the last part, interferogram nonlinearity is proposed as an error source that decreases the ARW performance of FOG under random vibration input.

4.1 Optical Power Fluctuation

Square wave phase modulation/demodulation (Chapter 2.4) can be configured to higher modulation depths for RIN suppression [46]. However, the derivations for the optical power fluctuations are carried with $\pm\frac{\pi}{2}$ depth for simplicity.

$$\Delta\phi_m(t) = \begin{cases} +\frac{\pi}{2}, 0 \le t < \tau \\ -\frac{\pi}{2}, \tau \le t < 2\tau \end{cases} \tag{4.1}$$

$$P_0(t) = \frac{I_0}{2}\left[1 + \cos(\Delta\phi_s(t) + \frac{\pi}{2})\right] = \frac{I_0}{2}[1 - sin(\Delta\phi_s(t))] \tag{4.2}$$

$$P_1(t+\tau) = \frac{I_0}{2}[1 + sin(\Delta\phi_s(t+\tau))] \tag{4.3}$$

Ordinary demodulation algorithm is,

$$\Delta \mathrm{P} = P_1 - P_0 = I_0 sin(\Delta\phi_s) \tag{4.4}$$

Optical power fluctuation can be modeled as a sinusoidal disturbance. The optical power fluctuation and Sagnac phase can be modeled as having the same frequency as the source of the disturbance for both terms is generally the same vibration input. However, the phase difference between the optical power fluctuation and the rate error is important. We analyze the optical power fluctuation for two different phase cases: in phase and out of phase with the rotation rate.

4.1.1 Optical Power Fluctuation and Rate Error are in Phase

The optical power fluctuation can be modeled as sinusoidal.

$$I_0(t) = I_0 + \alpha I_0 \sin(\omega t) \tag{4.5}$$

where, α is the ratio of the fluctuation.

Then,

$$P_0(t) = \frac{I_0}{2} - \frac{I_0}{2}\sin(\Delta\phi_s(t+\tau)) + \alpha\left[\frac{I_0}{2}\sin(\omega t) - \frac{I_0}{2}\sin(\omega t)\sin(\Delta\phi_s(t))\right] \quad (4.6)$$

$$P_1(t+\tau) = \frac{I_0}{2}[1 + \sin(\Delta\phi_s(t+\tau))] + \alpha\left[\frac{I_0}{2}\sin(\omega(t+\tau)) + \frac{I_0}{2}\sin(\omega(t+\tau))\sin(\Delta\phi_s(t+\tau))\right] \quad (4.7)$$

The first term is the Sagnac phase part, where the second term is the error raised due to optical fluctuation. Here, it is assumed that $\Delta\phi_s(t) \cong \Delta\phi_s(t+\tau)$. High bandwidth closed-loop operation is needed for this assumption to be satisfied. The demodulation can be calculated by,

$$\Delta \mathrm{P}_{10} = P_1 - P_0 \quad (4.8)$$

$$\Delta \mathrm{P}_{10} = I_0 \sin(\Delta\phi_s) + \alpha\frac{I_0}{2}[\sin(\omega t + \omega\tau) - \sin(\omega t)] + \alpha\frac{I_0}{2}\sin(\Delta\phi_s)[\sin(\omega t + \omega\tau) + \sin(\omega t)] \quad (4.9)$$

By using the trigonometric identity: $\sin(\omega t + \omega\tau) = \sin(\omega t)\cos(\omega\tau) + \cos(\omega t) sin(\omega\tau)$

The term becomes,

$$[\sin(\omega t + \omega\tau) - \sin(\omega t)] = -\sin(\omega t)[1 - \cos(\omega\tau)] + \cos(\omega t) sin(\omega\tau) \quad (4.10)$$

For a navigation grade FOG coil with length 1 km, $\tau = 5\mu s$, and with input vibration at frequency $f = 2\,kHz$ and $\omega = 2\pi f$, $sin(\omega\tau) = 0.0628$ and $1 - \cos(\omega\tau) = 0.0020$ so that the following approximation becomes valid.

$$sin(\omega\tau) \gg [1 - \cos(\omega\tau)] \tag{4.11}$$

$$[\sin(\omega t + \omega\tau) - \sin(\omega t)] = \cos(\omega t) sin(\omega\tau) \tag{4.12}$$

Similarly, for the term,

$$\begin{aligned} &[\sin(\omega t + \omega\tau) + \sin(\omega t)] \\ &\qquad = \sin(\omega t)\,[\cos(\omega\tau) + 1] + \cos(\omega t) sin(\omega\tau) \end{aligned} \tag{4.13}$$

$$sin(\omega\tau) \ll [\cos(\omega\tau) + 1] \cong 2 \tag{4.14}$$

$$[\sin(\omega t + \omega\tau) + \sin(\omega t)] = 2\sin(\omega t) \tag{4.15}$$

is obtained. So the difference equation becomes,

$$\begin{aligned} \Delta \mathrm{P}_{10} = I_0 \sin(\Delta\phi_s) + \alpha \frac{I_0}{2} \cos(\omega t) sin(\omega\tau) \\ + \alpha I_0 \sin(\Delta\phi_s) \sin(\omega t) \end{aligned} \tag{4.16}$$

Summation of the two optical powers is:

$$\begin{aligned} \Sigma \mathrm{P}_{10} = I_0 + \alpha \frac{I_0}{2} [\sin(\omega t + \omega\tau) + \sin(\omega t)] \\ + \alpha \frac{I_0}{2} \sin(\Delta\phi_s)\,[\sin(\omega t + \omega\tau) - \sin(\omega t)] \end{aligned} \tag{4.17}$$

and again by using the same approximations,

$$\Sigma \mathrm{P}_{10} = I_0 + \alpha I_0 \sin(\omega t) + \alpha \frac{I_0}{2} \sin(\Delta\phi_s) \cos(\omega t) sin(\omega\tau) \tag{4.18}$$

is obtained. Two approaches can be considered to the optical power normalization for the demodulation. High bandwidth optical power estimation can be obtained by the summation, or low bandwidth optical power fluctuation can be used. Low bandwidth estimation is more robust than the high bandwidth case as the summation is susceptible to the high frequency variations in the Sagnac phase.

The first case is using the high bandwidth normalization.

$$\frac{\Delta \mathrm{P}_{10}}{\Sigma \mathrm{P}_{10}} = \frac{I_0 \sin(\Delta\phi_s) + \alpha \frac{I_0}{2} \cos(\omega t) sin(\omega\tau) + \alpha I_0 \sin(\Delta\phi_s) \sin(\omega t)}{I_0 + \alpha I_0 \sin(\omega t)} \tag{4.19}$$

$$\frac{\Delta \mathrm{P}_{10}}{\Sigma \mathrm{P}_{10}} = \sin(\Delta\phi_s) + \frac{\alpha \frac{sin(\omega\tau)}{2} \cos(\omega t)}{1 + \alpha \sin(\omega t)} \tag{4.20}$$

$$\mathrm{error} = \frac{\alpha \frac{sin(\omega\tau)}{2} \cos(\omega t)}{1 + \alpha \sin(\omega t)} \tag{4.21}$$

$$\mathrm{error} \cong \alpha \frac{sin(\omega\tau)}{2} \cos(\omega t) \tag{4.22}$$

For navigation grade fiber coil with a length of 1000 m the flight time, τ, is 5 μs, and with 11 cm coil diameter and 1550 nm wavelength, the Sagnac scale factor is,

$$\mathrm{SF} = \frac{2\pi L D}{\lambda c} = 1.486s \tag{4.23}$$

$$\text{error} = \alpha \frac{sin(\omega\tau)}{2} \times \frac{180}{\pi} \frac{1}{\text{SF}} \times 3600 = 4357\alpha \ {}^{\circ}\!/_{h} \tag{4.24}$$

where $f = 2\ kHz$. Actually, this error is linearly proportional to the input frequency. Let $sin(\omega\tau) = \omega\tau$,

$$\text{error} = \alpha \frac{sin(\omega\tau)}{2} \times \frac{180}{\pi} \frac{1}{\text{SF}} \times 3600 = 0.35\alpha \times \omega \ {}^{\circ}\!/_{h} \tag{4.25}$$

This type of error can be classed as a Shupe type error for FOG. Mechanical Shupe error has the same characteristic for which the error increases linearly with the input frequency. For tactical grade fiber coil with a length of 200 m the flight time, τ, is 1 μs, and with 3 cm coil diameter and 1550 nm wavelength, the Sagnac scale factor is,

$$\text{SF} = \frac{2\pi LD}{\lambda c} = 0.081s \tag{4.26}$$

$$\text{error} = \alpha \frac{sin(\omega\tau)}{2} \times \frac{180}{\pi} \frac{1}{\text{SF}} \times 3600 = 1.3\alpha \times \omega \ {}^{\circ}\!/_{h} \tag{4.27}$$

We can formulate the error by using $\tau = \frac{n \times L}{c}$ as,

$$\text{error} = \alpha \times \omega \times \frac{1}{2} \frac{nL}{c} \frac{180}{\pi} \frac{\lambda c}{2\pi LD} \tag{4.28}$$

$$\text{error} = \alpha \times \frac{180 \times \lambda n}{(2\pi)^2 D} \times \omega \tag{4.29}$$

The error is inversely proportional with the diameter but independent of the length of the fiber coil.

The second case is the low bandwidth normalization:

$$\frac{\Delta P_{10}}{I_0} = \frac{I_0 \sin(\Delta\phi_s) + \alpha \frac{I_0}{2} \cos(\omega t) sin(\omega\tau) + \alpha I_0 \sin(\Delta\phi_s) \sin(\omega t)}{I_0} \tag{4.30}$$

$$\frac{\Delta P_{10}}{I_0} = \sin(\Delta\phi_s) \left[1 + \alpha \sin(\omega t)\right] + \alpha \frac{sin(\omega\tau)}{2} \cos(\omega t) \tag{4.31}$$

$$\text{error} = \alpha \sin(\Delta\phi_s) \sin(\omega t) + \alpha \frac{sin(\omega\tau)}{2} \cos(\omega t) \tag{4.32}$$

The emerging error part due to low bandwidth normalization is the first term, which depends on the Sagnac phase shift. The Sagnac phase $sin(\Delta\phi_s)$ is also expected to have a sinusoidal characteristic as well as the optical fluctuation.

For a sinusoidal input with 1 °/s amplitude and 1% optical power fluctuation ($\alpha = 0.01$),

$$\text{error} = 0.01 \times 3600 \times \sin^2(\omega t) = 36 \frac{(1 - \cos(2\omega t))}{2} \tag{4.33}$$

resulting in a bias error of $18\ °/h$. This error is independent of the Sagnac scale factor as the rotation input is directly multiplicative with the error term: Higher scale factor creates higher phase shift, which is normalized by again the scale factor.

4.1.2 Optical Power Fluctuation and Rate Error are out of Phase

If the optical power fluctuation is out of phase with the input;

$$I_0(t) = I_0 + \alpha I_0 \cos(\omega t) \tag{4.34}$$

Then by using similar derivations and approximations we can obtain the difference equation as,

$$\Delta P_{10} = I_0 \sin(\Delta\phi_s) - \alpha \frac{I_0}{2} \sin(\omega t) sin(\omega\tau) + \alpha I_0 \sin(\Delta\phi_s) \cos(\omega t) \tag{4.35}$$

and the summation as,

$$\Sigma P_{10} = I_0 + \alpha I_0 \cos(\omega t) - \alpha \frac{I_0}{2} \sin(\Delta\phi_s) \sin(\omega t) sin(\omega\tau) \tag{4.36}$$

High bandwidth normalization results same as the in-phase scenario, where the error is Shupe like error. However, for the low bandwidth normalization case,

$$\frac{\Delta P_{10}}{I_0} = \frac{I_0 \sin(\Delta\phi_s) - \alpha \frac{I_0}{2} \sin(\omega t) sin(\omega\tau) + \alpha I_0 \sin(\Delta\phi_s) \cos(\omega t)}{I_0} \tag{4.37}$$

$$\frac{\Delta P_{10}}{I_0} = \sin(\Delta\phi_s) \left[1 + \alpha \cos(\omega t)\right] - \alpha \frac{sin(\omega\tau)}{2} \sin(\omega t) \tag{4.38}$$

$$\text{error} = \alpha \sin(\Delta\phi_s) \cos(\omega t) - \alpha \frac{sin(\omega\tau)}{2} \sin(\omega t) \tag{4.39}$$

and with sinusoidal out of phase input,

$$\Delta\phi_s = \sin(\omega t) \, {}^{\circ}/_{s} \tag{4.40}$$

$$\text{error} = \frac{\alpha}{2} \sin(2\omega t) - \alpha \frac{sin(\omega\tau)}{2} \sin(\omega t) \tag{4.41}$$

where no bias term emerges.

4.1.3 Rate Error for a Closed-Loop FOG

Error equations are directly related to the Sagnac phase shift, which can be suppressed in closed-loop configuration of FOG. Closed-loop is generally assumed to eliminate the Sagnac phase shift totally, which is valid under steady rotation rates. However, under high frequency input, like vibration, FOG error response limits the suppression magnitude. A discrete system model for a closed-loop FOG with a controller is given in Figure 4.1.

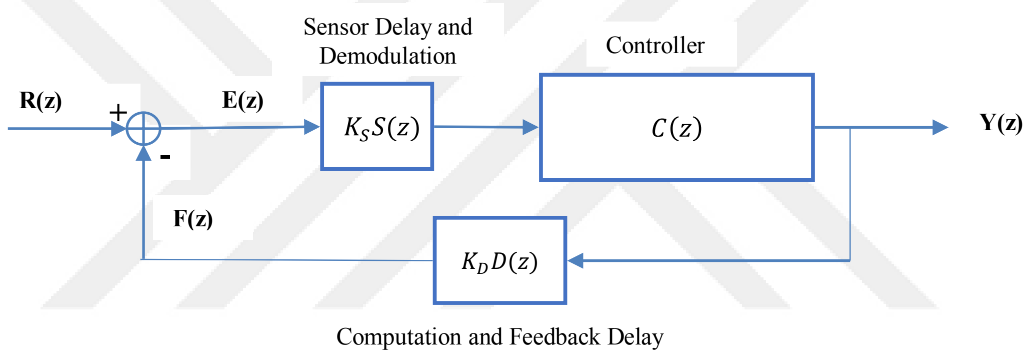

Figure 4.1: FOG discrete time model and controller diagram.

$R(z)$ is the Sagnac phase shift experienced by the counter-propagating waves in the fiber coil. $E(z)$ is the uncompensated phase difference between the waves, the difference between $R(z)$ and $F(z)$. $F(z)$ is the feedback applied to the electro-optic phase modulator for the injection of the phase difference between the waves. $E(z)$ is sensed by the photodetector, receiver electronics, and square wave demodulation algorithm, all together as $K_S S(z)$. Square wave demodulation is the main delay mechanism defined by Equation (4.4). The controller, $C(z)$, is a pure integrator calculates the feedback and the output $Y(z)$. The feedback mechanism, $K_D D(z)$, including all drive electronics and feedback ramp algorithm, has a single step size delay. The responses are defined as follows.

$$C(z) = \frac{1}{1 - z^{-1}} \tag{4.42}$$

$$S(z) = \frac{1}{2}(z^{-1} + z^{-2}) \tag{4.43}$$

$$D(z) = z^{-1} \tag{4.44}$$

$$H_Y(z) = \frac{Y(z)}{R(z)} = \frac{K_s S(z) C(z)}{1 + K_s S(z) C(z) K_D D(z)} \tag{4.45}$$

$$H_E(z) = \frac{E(z)}{R(z)} = \frac{1}{1 + K_s S(z) C(z) K_D D(z)} \tag{4.46}$$

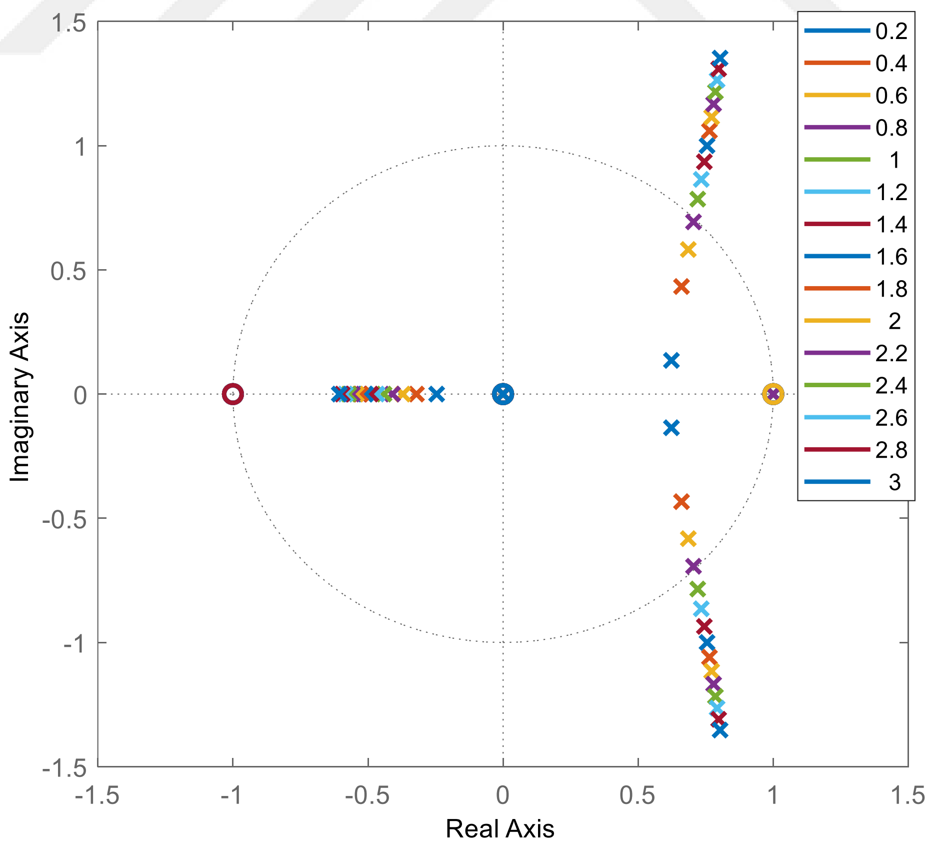

Figure 4.2: Stability of the system for different controller gains.

Stability analyses of the output response, $H_Y(z)$, for different gains are given by the pole-zero diagram in Figure 4.2. The system is unstable for gains larger than 0.8. The maximum gain should be selected for the bandwidth to be as high as possible. Error response $H_E(z)$ is obtained by using $K_s K_D = 0.8$, as,

$$H_E(z) = \frac{E(z)}{R(z)} = \frac{2z^4 - 2z^3}{2z^4 - 2z^3 + 0.8z^2 - 0.8z} \tag{4.47}$$

Bode diagrams of the output and error responses for 200 kHz sampling rate (navigation grade fiber coil with 1000 meter fiber length) are given in Figure 4.3 and Figure 4.4. Highest frequency band for the vibration disturbance is 2 kHz for most military applications [47]. Magnitude and phase of the output response are flat up to 10 kHz. Error response suppression is nearly -20 dB for 2 kHz and injects 90° phase shift to rate error which is flat with respect to frequency up to 10 kHz.

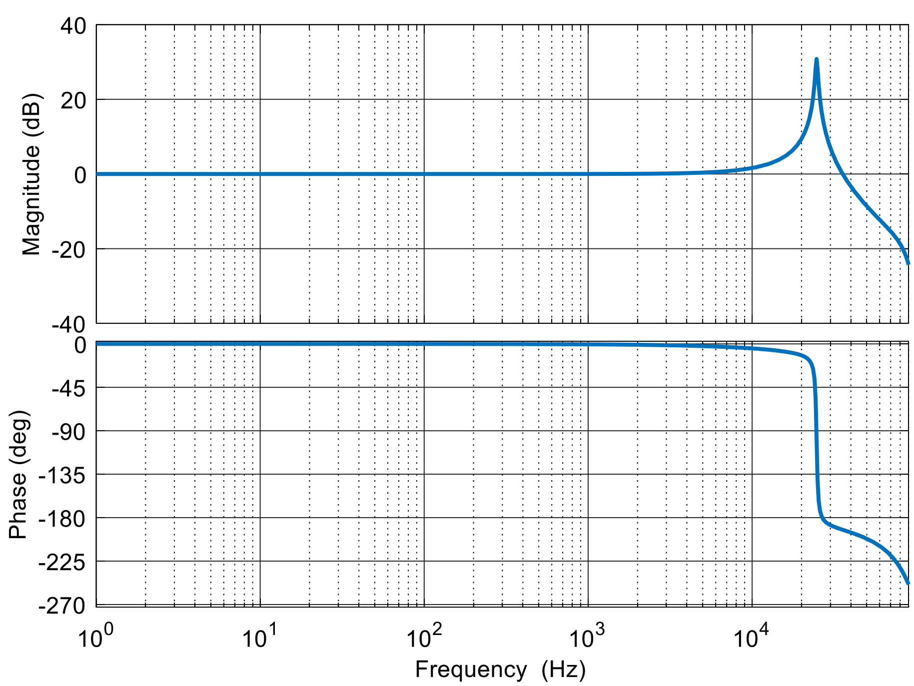

Figure 4.3: Output response.

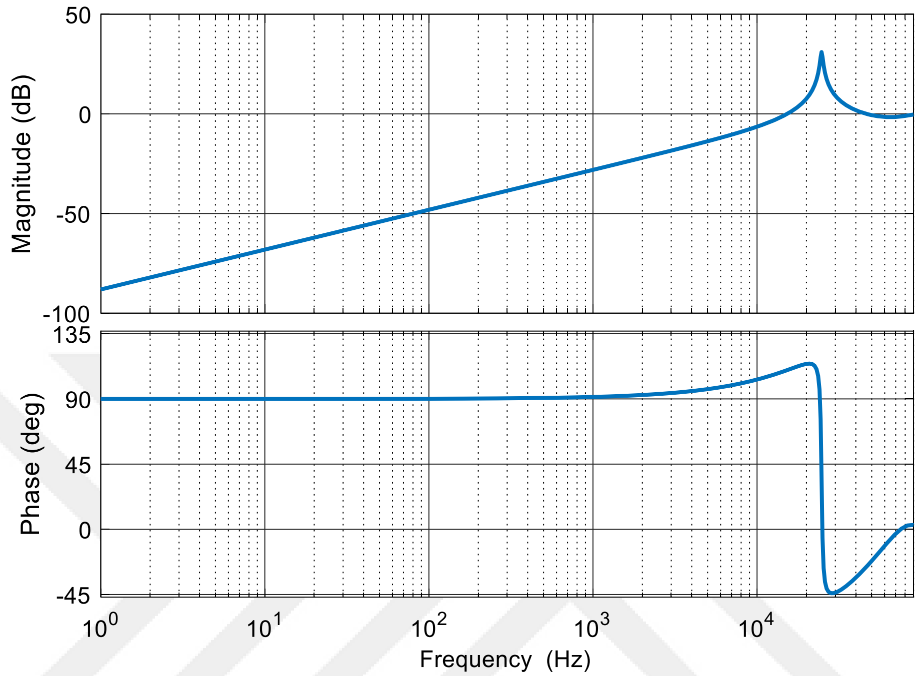

Figure 4.4: Error response.

4.1.4 Optical Power Fluctuation Estimation with Simulation and Test

Bias estimation of a FOG may need several minutes of data due to the gyroscope noise. Navigation grade gyroscopes generally offer less than 0.01 $°/h$ bias error and 0.002 $°/\sqrt{h}$ ARW, which results in 0.0035 $°/h$ uncertainty on the bias estimation for 20 minutes of data. On the other hand, phase error computations are carried at 200 kHz which is a very high frequency for simulations relative to the data collection time. Algorithm 4.1 is given to overcome this issue. Algorithm 4.1 up-samples the gyroscope data collected at 2 kHz to 200 kHz and then applies the transfer functions of the closed-loop system and calculates the standard derivation of the phase error, which is used for bias estimations.

Algorithm 4.1: Controller response

```
% upsample data from 2 kHz to 200 kHz.

Rd = resample(data, 100,1);
```

```
% find the error response
Ts = 1e-6;
KD = 1;
KS = 1;
S = tf([1 1], [2 0 0] ,Ts);
D = tf([1]  , [1 0]   ,Ts);
C1 = tf([1 0], [1 -1] ,Ts);
E1 = 1 / (1 + 0.8*KS*S*C1*KD*D);
[NUM,DEN] = tfdata(E1);
rd_filtered_E1_G08 = fitler(NUM{1},DEN{1},rd);
% calculate 82eviation
std(rd_filtered_E1_G08(1e6:end))
```

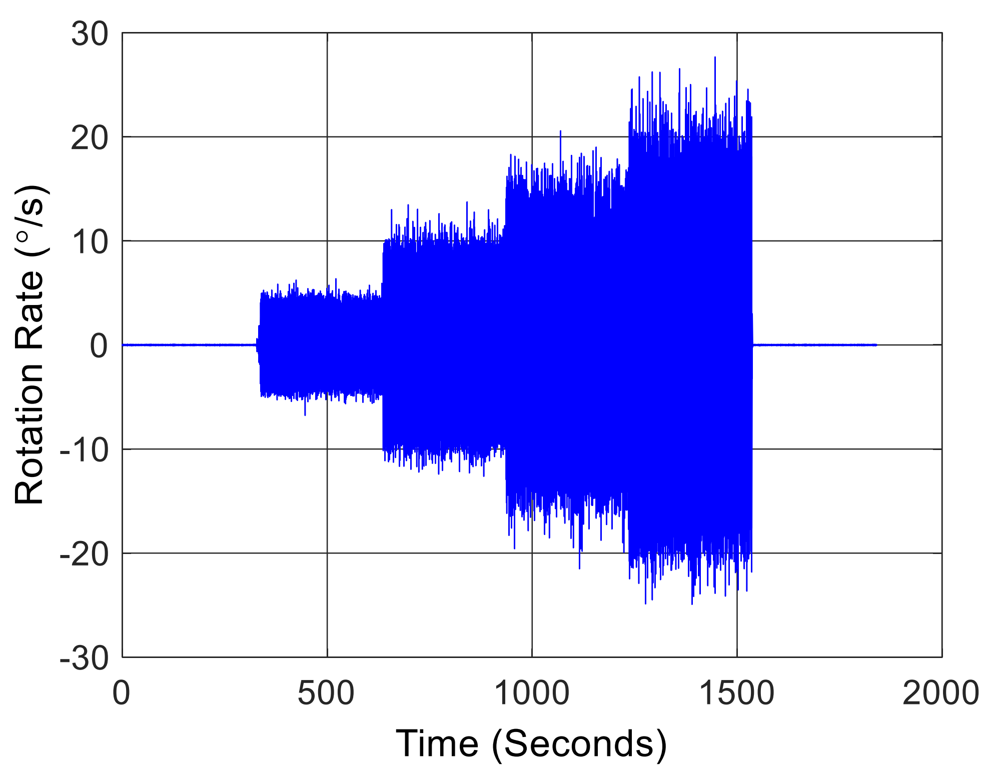

Figure 4.5: FOG data under vibration test.

Navigation grade FOG data is collected at 2 kHz sampling rate under the vibration. Vibration input has a flat frequency profile between 20 Hz to 2 kHz and magnitude 2 g_{rms}. Test procedure has the steps approximately 5 minutes long starting from no vibration to 100% energy with 25% steps and then again no vibration (Figure 4.5). Rotation rate and bias errors are measured for each step (Table 4.1). Uncompensated phase error signal at 200 kHz is estimated with Algorithm 4.1. Bias errors are normalized to the measurement at the first step.

Table 4.1: Bias error and rotation rate measurements, and uncompensated phase error estimation

Vibration Input (g_{rms})	Bias Error (°/h)	Rotation Rate (°/s, @2kHz, 1σ)	Uncompensated Phase Error (°/s, @200 kHz, 1σ)
0	0	0.0156	4.53×10^{-4}
0.5	-0.207	1.35	0.036
1	-0.571	2.92	0.076
1.5	-0.963	4.13	0.114
2	-1.879	5.79	0.149
0	-0.011	0.0153	4.46×10^{-4}

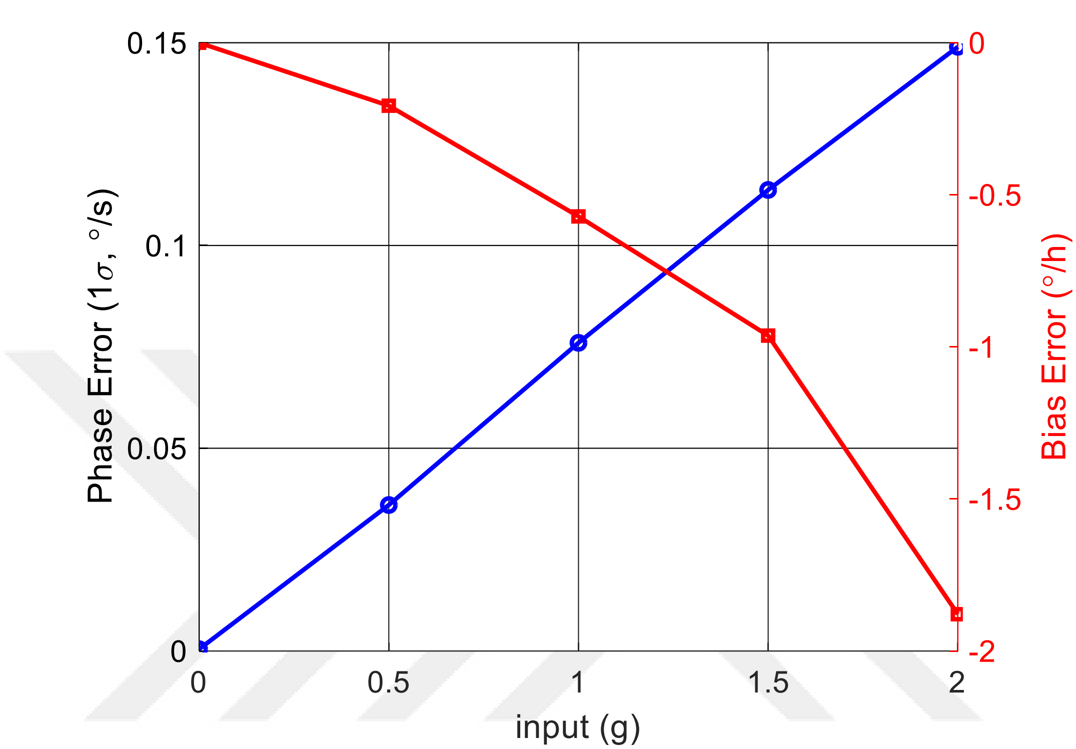

Figure 4.6: Phase and bias errors vs vibration input level.

Uncompensated phase error is linearly proportional to input level while bias error has a second-order relation (Figure 4.6). Optical power fluctuation (α) and uncompensated phase error can be modeled as linear relations $\alpha = \alpha_0 \times g$, and $e = e_0 \times g$, with respect to input g, and bias error as a quadratic relation bias $= b_0 \times g^2$. Bias error can be estimated by using the equation (4.32).

$$\text{bias} = \frac{1}{2} \times \alpha \times e \times 3600 \tag{4.48}$$

$$b_0 \times g^2 = 1800 \times \alpha_0 e_0 \times g^2 \tag{4.49}$$

$$\alpha_0 = \frac{b_0}{1800 e_0} \tag{4.50}$$

Optical power fluctuation, α_0 can be obtained as 0.34%/g_{rms} by using the least-squares estimation on the data provided in Table 4.1. Optical power fluctuation is assumed to be totally in phase with the input vibration profile. For a 0.01°/h bias performance, 0.0017% optical fluctuation should be achieved, which is clearly challenging. In this analysis, the closed-loop gain is assumed to be stable, well known, and exactly 0.8. However, this could not be the case. Uncompensated phase error estimations under 2 g_{rms} vibration input for different closed-loop gains are given in Table 4.2. The closed-loop gain behaves like a constant coefficient for the suppression of the phase error. Better loop gain provides less uncompensated phase error so less bias due to vibration.

Table 4.2: Controller error response vs controller gain

Loop Gain	Uncompensated Phase Error (°/s, @200 kHz, 1σ)
0.8	0.149
0.4	0.298
0.2	0.594
0.1	1.17

4.2 Mechanical Shupe Error

Mechanical Shupe error is an error source created in the fiber coil by rapid contraction and relaxation of the fiber coils and resulting in nonreciprocal phase shift. Vibration disturbance is a linear acceleration input to FOG. Counter-propagating waves inside the fiber coil are sensitive to rapid disturbances as discussed in Chapter 3.1. In the vibration condition, the force between the fibers can be defined for the radial axis and there is no stress along the propagation axis of the fiber [15]. Equation (3.11) can be rewritten as,

$$\begin{bmatrix}\varepsilon_x\\ \varepsilon_y\\ \varepsilon_z\end{bmatrix}=\frac{1}{E}\begin{bmatrix}1 & -\mu & -\mu\\ -\mu & 1 & -\mu\\ -\mu & -\mu & 1\end{bmatrix}\begin{bmatrix}\sigma_x\\ \sigma_y\\ 0\end{bmatrix} \tag{4.51}$$

$$\begin{bmatrix}\varepsilon_x\\ \varepsilon_y\\ \varepsilon_z\end{bmatrix}=\frac{1}{E}\begin{bmatrix}\sigma_x-\mu\sigma_y\\ -\mu\sigma_x+\sigma_y\\ -\mu\sigma_x-\mu\sigma_y\end{bmatrix} \tag{4.52}$$

And Equation (3.18) can be rewritten by using the mechanical stress.

$$\begin{aligned}\Delta\varphi=\frac{\beta_0 Ln}{E}\Bigg\{&\left[n^2\mu p_{12}-\frac{n^2}{2}p_{11}-\mu\right]\sigma_x\\ &+\left[\frac{n^2}{2}(\mu p_{11}+\mu p_{12}-p_{12})-\mu\right]\sigma_y\Bigg\}\end{aligned} \tag{4.53}$$

Integrating the mechanical stress change for all over the fiber coil results in the rate error due to the mechanical Shupe error:

$$\Omega(t)=\frac{n}{ELD}\int_0^L(\mathrm{C}\dot{\sigma}_x+D\dot{\sigma}_y)(L-2z)dz \tag{4.54}$$

where $\mathrm{C}=n^2\mu p_{12}-\frac{n^2}{2}p_{11}-\mu$,

and $D=\frac{n^2}{2}(\mu p_{11}+\mu p_{12}-p_{12})-\mu$.

This error is very similar to the thermal sensitivity of the coil. However, the temperature change is a very slow disturbance relative to the vibration. Thermal sensitivity is a slowly varying error mechanism that can be classified as bias instability for FOG. On the other hand, the vibration error mechanism can be classified as a linear coefficient for the relation between the rotation rate error and the vibration. The three-dimensional mechanical Shupe error can be represented in terms of the Shupe coefficients as,

$$\begin{bmatrix}\delta\omega_x(t)\\ \delta\omega_y(t)\\ \delta\omega_z(t)\end{bmatrix} = \begin{bmatrix}S_{xx} & S_{xy} & S_{xz}\\ S_{yx} & S_{yy} & S_{yz}\\ S_{zx} & S_{zy} & S_{zz}\end{bmatrix}\frac{d}{dt}\begin{pmatrix}f_x(t)\\ f_y(t)\\ f_z(t)\end{pmatrix} \tag{4.55}$$

where f_x, f_y, f_z are the specific force components experienced on the fiber gyros and $S_{xx}, S_{xy}, S_{xz}, S_{yx}, S_{yy}, S_{yz}, S_{zx}, S_{zy}, S_{zz}$ are the corresponding Shupe coefficients. If the specific force unit is taken as 'g', then the units of Shupe terms become $\frac{\frac{rad/s}{g}}{rad/s} = \frac{1}{g}$. Specifically, consider a linear sine vibration $f_x(t) = \mathrm{F}_x\sin(\omega t)$, then the induced angular rate becomes,

$$\delta\omega_x(t) = S_{xx}\frac{\mathrm{d}}{dt}(\mathrm{F}_x\sin(\omega t)) = F_x\omega S_{xx}\cos(\omega t) \tag{4.56}$$

The Shupe coefficient is generally defined in terms of the angular rate sine amplitude change per Hz as deg/hr/g/Hz instead of the angular frequency, ω. The relation between these definitions can be derived as,

$$\delta\omega_x(t) = F_x\omega S_{xx}\cos(\omega t) \tag{4.57}$$

$$\delta\omega_x(t) = F_x(2\pi S_{xx})f\cos(2\pi f t) \tag{4.58}$$

$$\delta\omega_x(t) = \bar{S}_{xx}F_x f\cos(2\pi f t) \tag{4.59}$$

where,

$$\bar{S}_{xx}(rad/s/g/Hz) = (2\pi)S_{xx}(1/g) \tag{4.60}$$

The mechanical Shupe effect can be realized with the FOG model under vibration simulation. Vibration input has an amplitude of 2 g_{rms} and a frequency range 20Hz to 2 kHz. The spurious rotation rate created by the fiber coil has the spectrum given in Figure 4.7. The Shupe coefficient is 3 °/h/g/Hz and the spectrum linearly increases with the input vibration frequency.

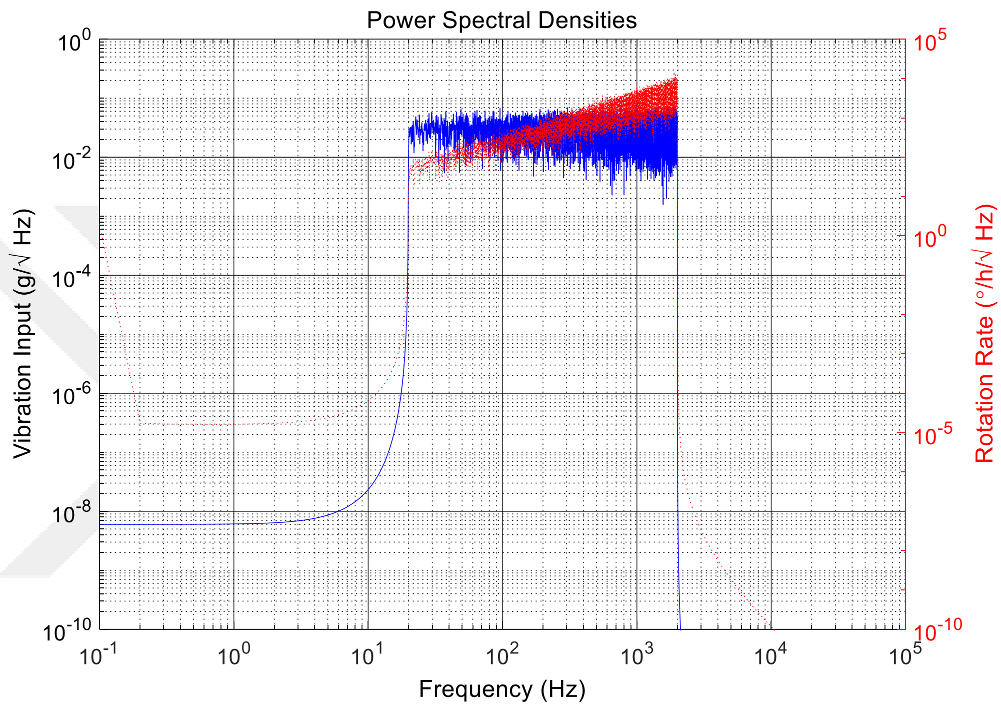

Figure 4.7: Mechanical Shupe error simulation. Linear vibration is transformed into spurious rotation rate due to mechanical Shupe error.

4.2.1 Tests for Mechanical Shupe Error

Power spectral density (PSD) graphs of an open-loop navigation grade FOG output for different vibration input energies are given in Figure 4.8. The vibration profile spans 20Hz to 2 kHz. Test data is collected at four vibration levels starting from 0.5 g_{rms} to 2 g_{rms}, with 0.5 g_{rms} steps. No vibration data has an almost flat spectrum up to 400 Hz which is the noise floor of the FOG. Energy from 400 Hz to 1 kHz is accepted as the disturbance created by the vibration table magnetic field. This part of the data is amplified at each vibration level and neglected in the Shupe coefficient calculations. The rotation rate spectrum increases linearly with respect to the input frequency and the vibration level which certainly defines the Shupe mechanism. The mechanical Shupe coefficient is estimated to be 2.87 °/h/g/Hz for this test sequence.

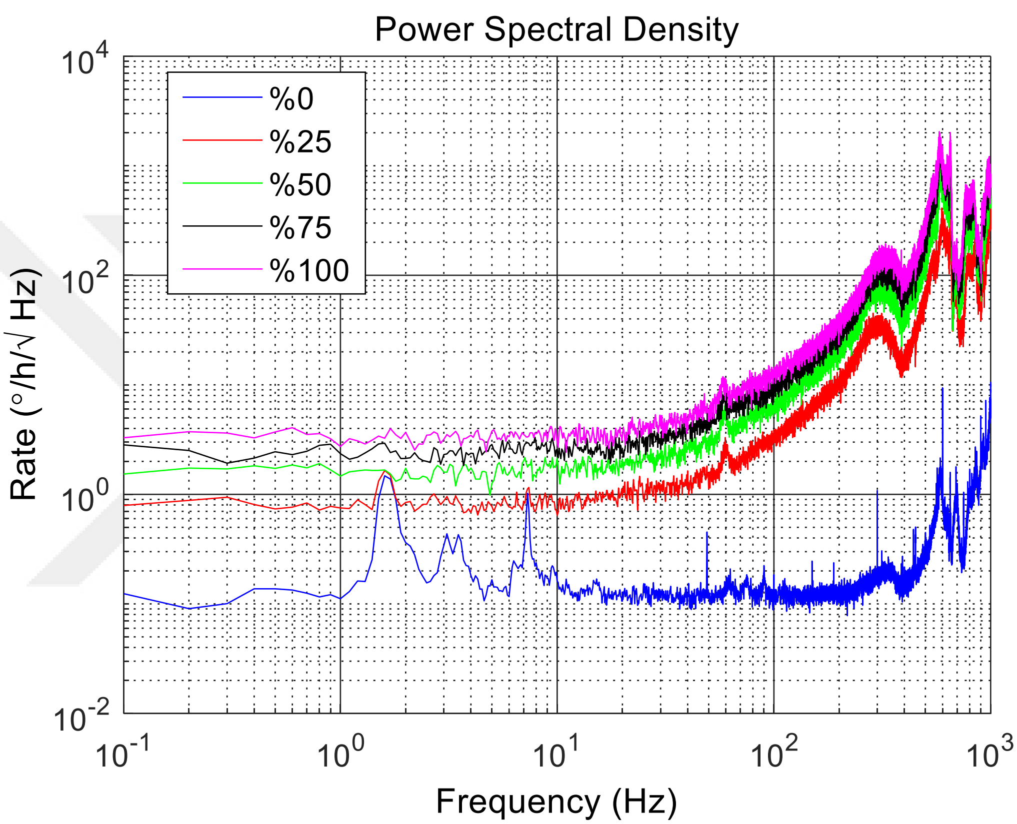

Figure 4.8: PSD of FOG output under different vibration energy levels.

4.3 Interferogram Nonlinearity

Square wave demodulation of a FOG measurement is given in Equation (4.4). The phase difference can be extracted from the difference of the odd and even samples as,

$$\Delta\phi_s = \arcsin(\frac{\Delta P}{I_0}) \tag{4.61}$$

High performance FOGs are usually configured to be closed-loop. The Sagnac phase difference between the counter-propagating waves becomes zero under the closed-loop operation, so small angle approximation can be applied.

$$\Delta\phi_s = \frac{\Delta \mathrm{P}}{I_0} \tag{4.62}$$

This approximation is valid under low dynamics. However, for high dynamic environments like the vibration, high frequency components of the input signal can be suppressed to some degree. Nonlinear components arise if the suppression is not perfect.

Taylor series expansion of the arcsin function is given as,

$$\arcsin(x) = x + \frac{1}{6}x^3 + \frac{3}{40}x^5 + \frac{5}{112}x^7 + \cdots \tag{4.63}$$

Let the phase difference between the waves is a sinusoidal function with amplitude A and frequency ω,

$$\Delta\phi_s = A\sin(\omega t) \tag{4.64}$$

then the 2nd term of the Taylor series results in a sinusoidal response at a frequency three times of the input.

$$\sin^3(\omega t) = \frac{3}{4}\sin(\omega t) - \frac{1}{4}\sin(3\omega t) \tag{4.65}$$

which can be obtained by using the trigonometric identities of $\sin^2(a) = \frac{1-\cos(2a)}{2}$ and $sin(a)cos(\mathrm{b}) = \frac{1}{2}[sin(a+b) + sin(a-b)]$.

It is seen that the nonlinearity does not create a bias shift for this case. This may be the reason that the nonlinearity is a neglected error source in the literature. However, if multiple sinusoidal inputs with different frequencies exist at the same time, lower frequency components emerge in the output. Let the input be a combination of two sinusoidal with frequency difference $\Delta\omega$,

$$\Delta\phi_s = A[\sin(\omega t) + \sin(\omega t + \Delta\omega t)] \tag{4.66}$$

The first two terms of the Taylor series of the arcsin of the phase $\Delta\phi_s$ becomes,

$$\begin{aligned} &A^3[\sin(\omega t) + \sin(\omega t + \Delta\omega t)]^3 \\ &= \mathrm{A}^3[\sin^3(\omega t) + 3\sin^2(\omega t)\sin(\omega t + \Delta\omega t) \\ &+ 3\sin(\omega t)\sin^2(\omega t + \Delta\omega t) + \sin^3(\omega t + \Delta\omega t)] \end{aligned} \tag{4.67}$$

After expanding the equation (4.67) by using the trigonometric identities, a large equation with 8 terms representing different frequency components are obtained. Table 4.3 shows the amplitude of each frequency component of the output. Nonlinear terms depend on the third order of the amplitude. The first row is the lower frequency part of the output than the input. The emergence of this frequency is important as it results in the increase of ARW. The resulting component may be a bias shift if one of the sinus frequencies is two times the other one.

Table 4.3: Amplitudes of frequency components

Frequency	**Amplitude**
$\omega - \Delta\omega$	$\frac{3}{24}A^3$
ω	$A + \frac{9}{24}A^3$
$\omega + \Delta\omega$	$A + \frac{9}{24}A^3$

$\omega + 2\Delta\omega$	$\frac{3}{24}A^3$
3ω	$-\frac{1}{24}A^3$
$3\omega + \Delta\omega$	$-\frac{3}{24}A^3$
$3\omega + 2\Delta\omega$	$-\frac{3}{24}A^3$
$3\omega + 3\Delta\omega$	$-\frac{1}{24}A^3$

Furthermore, the gyroscopes are subjected to random vibration profiles, i.e. many frequencies beat together. Input with a frequency band can end up with many different frequency components, especially the low frequencies. Low frequency error can be defined as the increase of the gyroscope noise i.e. degradation of the ARW performance. This error is also dependent on the Sagnac phase shift. Closed-loop configuration is expected to suppress the error. Simulations using a navigation grade FOG discrete model are discussed to show these relations.

4.3.1 FOD Discrete Model

All digital closed-loop navigation grade FOG model is given in Algorithm 4.2. Closed-loop gain can be changed, optical power fluctuation ratio can be set, and the demodulation can be selected as;

1) the ideal case, $\arcsin(x) = \arcsin(x)$,
2) model with $\arcsin(x) = x$,
3) model with $\arcsin(x) = x + \frac{1}{6}x^3$,
4) model with $\arcsin(x) = x + \frac{1}{6}x^3 + \frac{3}{40}x^5$.

Random vibration input which spans 20 Hz to 2 kHz with 2 g_{rms} energy is created and applied to the model. The Shupe mechanism results in a random rotation rate distribution as given in Figure 4.7 which is the input to the FOG model.

Algorithm 4.2: FOG discrete model

```
Fs      = 200e3;
tfin    = 21;
t = (1/Fs:1/Fs:tfin)';
sz = length(t);
Shupe = 3; % deg/h/g/Hz

RVSPEC.freqvec    = [20 2000];
RVSPEC.magvec     = [0.002 0.002];

rvgen3;
noise    = 0.001/60*sqrt(Fs) * randn(sz,1); % 1sigma,
deg/s

input = rot_y_randvib/3600 + noise; % deg/s

alpha = 0;
I0       = 200e-6 *(1 + alpha * y_randvib); %Watt
I0_DC = mean(I0)*ones(length(I0),1);

% FOG Params
Gain = 0.8;
SF       = 2*pi*1100*10e-2/1550e-9/3e8; %seconds, NG
faz = input * SF * pi/180 ; %rad
modulasyon = pi/2;

%% Closed Loop

tek = zeros(floor(sz/2),1);
cift = zeros(floor(sz/2),1);
faz_est = zeros(floor(sz/2),1);
FB = zeros(floor(sz/2),1);
I = faz_est;

j = 2;
k = 1;
for i=1:sz

    if mod(i,2) == 0 % cift
```

```
        cift(j)   = I0(i)/2 *(1+cos(faz(i) -
modulasyon - FB(j-1)));

        faz_est(j) = ( (cift(j) - tek(k-1) ) /
I0_DC(i)); % asin(x) = x

%         faz_est(j) = asin ((cift(j) - tek(k-1))  /
I0_DC(i)); % asin(x) = asin(x)


%         faz_est(j) = (cift(j) - tek(k-1))/I0_DC(i) +
(1/6)*((cift(j) - tek(k-1))/I0_DC(i))^3 ;  % asin(x) =
x + (1/6)*x^3

%                 faz_est(j) = (cift(j) - tek(k-
1))/I0_DC(i) + (1/6)*((cift(j) - tek(k-1))/I0_DC(i))^3
...
%             + (3/40)*((cift(j) - tek(k-
1))/I0_DC(i))^5; % asin(x) = x + (1/6)*x^3 +
(3/40)*x^5

        FB(j+1) = FB(j) + faz_est(j) * Gain;
        j = j+1;

    elseif mod(i,2) == 1 % tek

        tek(k)  = I0(i)/2 *(1+cos(faz(i) + modulasyon
- FB(j-1)));
        k = k+1;

    end

end
```

4.3.2 Simulations for ARW Performance

A flat spectrum vibration (20 Hz to 2 kHz, 2 g_{rms}) is created for the FOG discrete model. The flat spectrum is shaped by the mechanical Shupe effect and results in phase shift input to the model. Input vs. the open-loop FOG output is plotted in Figure 4.9. Although there is no input for frequencies below 20 Hz, interferogram nonlinearity results in a noise band. This noise level increases with respect to the input amplitude. The increase rate is linearly proportional to the input amplitude's cube which is aligned with the derivations presented for the nonlinearity.

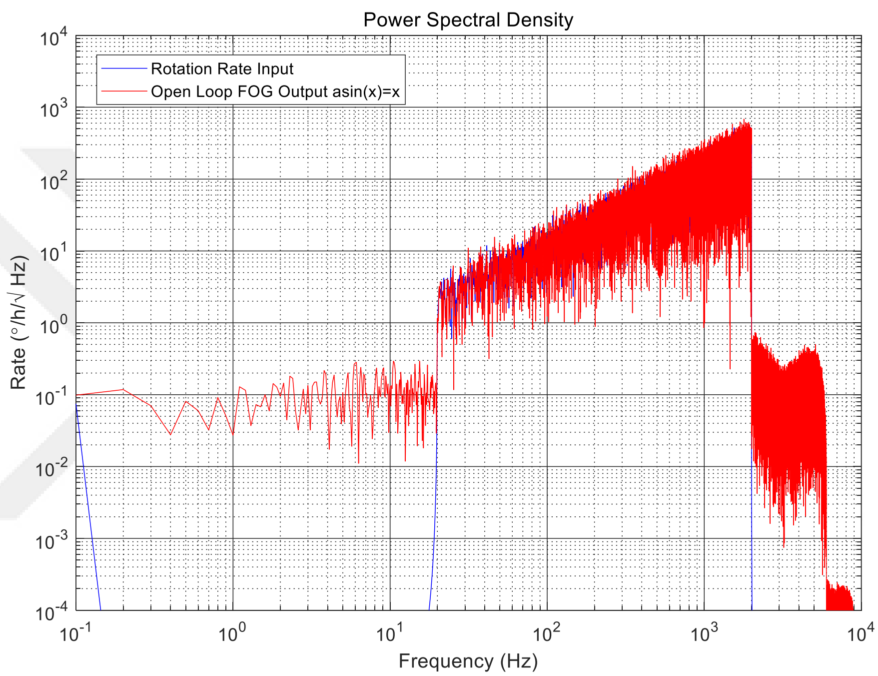

Figure 4.9: Input vs FOG model output. Here asin is modeled as asin(x) = x, i.e. with error.

Table 4.4: ARW of open-loop FOG configuration for different input amplitudes

Input energy (g_{rms})	**ARW (°/√h)**
0.2	1.1×10^{-6}
0.4	1.0×10^{-5}
0.8	6.6×10^{-5}
1.6	5.3×10^{-4}
3.2	4.7×10^{-3}
6.4	3.3×10^{-2}

Military standards dictate performance for inertial systems under certain vibration profiles. MIL-STD-810 is a widely referred military standard for environmental requirements. MIL-STD-810G Figure 514.6D-1 Category 12 is a standard for jet aircraft (Figure 4.10) [47].

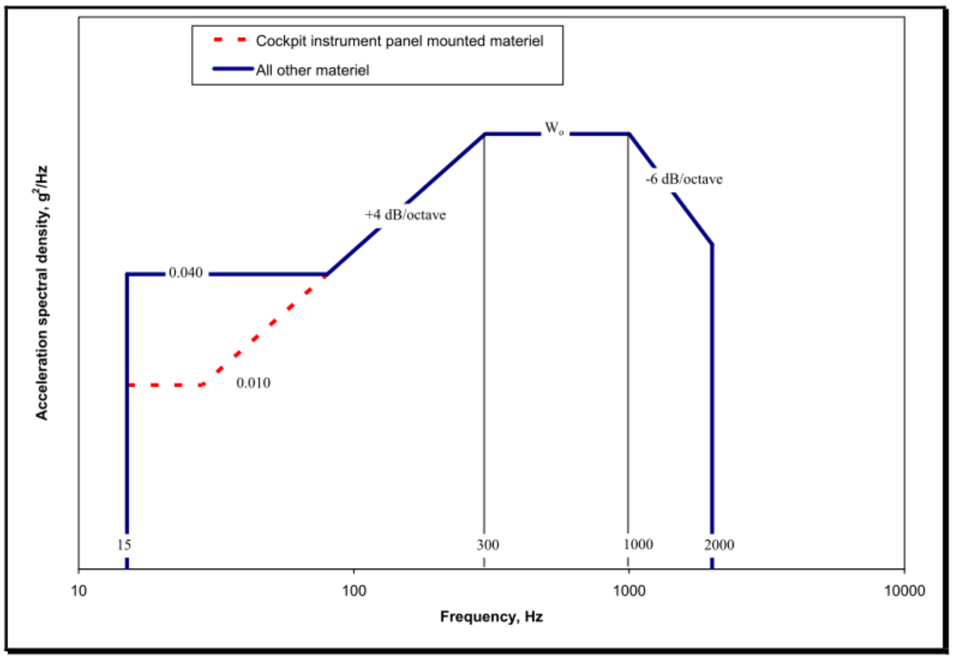

Figure 4.10: Power spectral density of MIL-STD-810G Figure 514.6D-1 Category12 [47].

This vibration profile is a linear acceleration input to the gyroscopes. The mechanical Shupe effect is used to obtain the power spectral density of the spurious rotation induced on the gyroscope. The Shupe coefficient is taken as 3 deg/h/g/Hz, and the cut-off frequency for the input vibration profile is taken as 60 Hz for the simulations. The resulting rotational power spectral density is given in Figure 4.11.

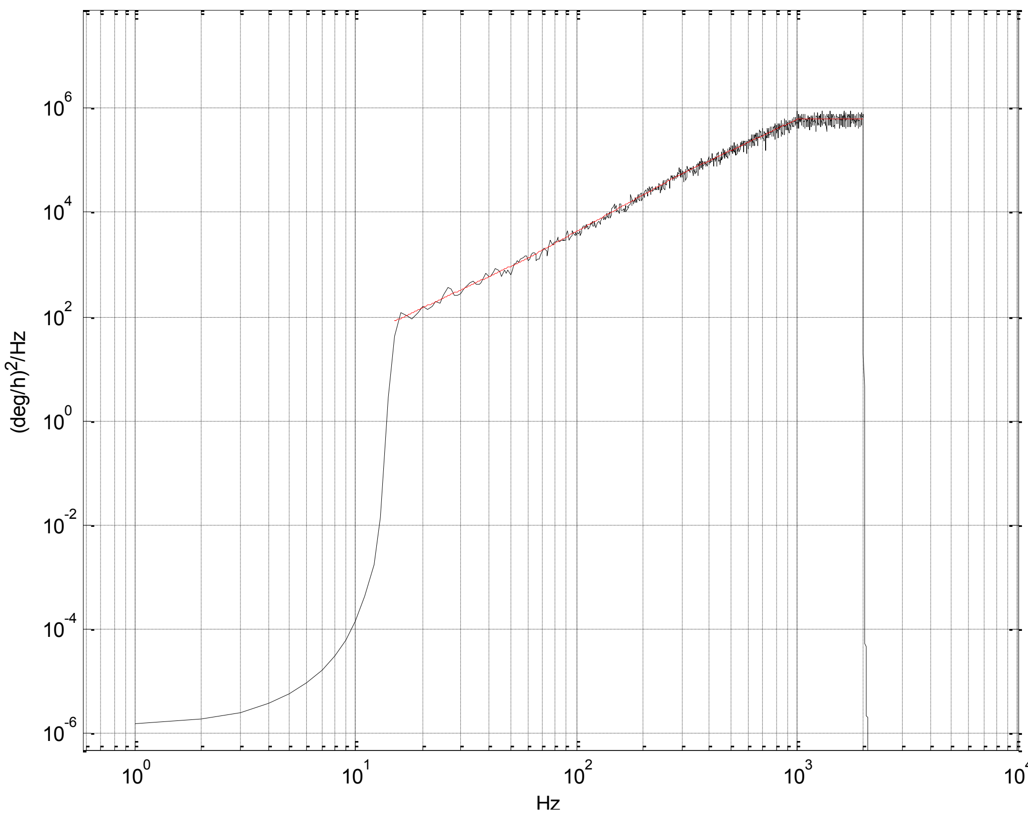

Figure 4.11: Power spectral density of the induced rotation

Open-loop configuration is more susceptible to rapid changes on the input than the closed-loop one. Some simulation results of open-loop FOG are presented in Table 4.5. Loop closure is a high frequency algorithm (around 100 kHz for navigation grade FOG). It may be challenging to implement the 'asin' function in the algorithm so that the 3rd and 5th order approximations are discussed. 7th order approximation promises navigation grade ARW performance for the open-loop configuration.

Table 4.5: ARW for different asin approximations

asin(x) approximation	**ARW (°/√h)**
asin(x)	0.0010 (Noise Floor)
1st order (x)	0.0755
3rd order	0.0134

5^{th} order	0.0035
7^{th} order	0.0015

Closed-loop suppresses the phase shift and that leads to the reduction of the nonlinearity error. Loop closure bandwidth should be as high as possible for better performance. Closed-loop simulation results are given in Figure 4.13 and Table 4.6. It is seen that the loop closure at Gain 0.1, which corresponds to approximately 10 kHz loop closing rate, performs enough for a navigation grade ARW performance.

Table 4.6: ARW for different FOG configurations

asin(x) approximation	**Gain**	**ARW (°/√h)**
1^{st} order (x)	0.8	0.0010 (Noise Floor)
1^{st} order (x)	0.5	0.0010
1^{st} order (x)	0.1	0.0131
1^{st} order (x)	0.05	0.0379
3^{rd} order	0.1	0.0017
5^{th} order	0.1	0.0010

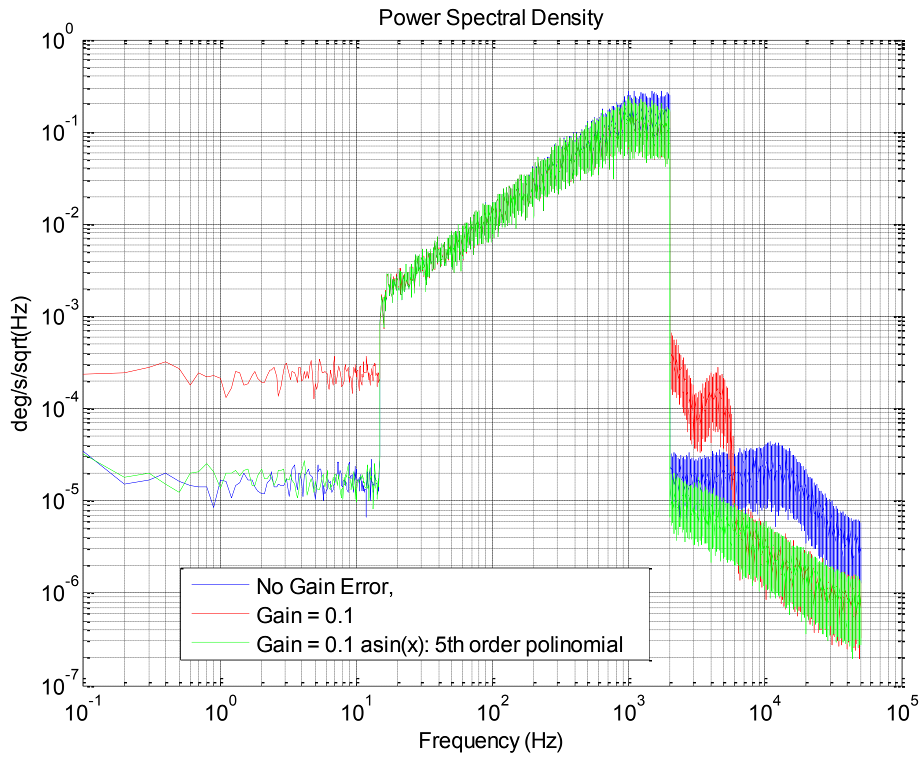

Figure 4.12: Gyroscope output power spectral density.

4.4 Vibration Tests at High Sampling Rate

Navigation grade FOG setup is produced for the vibration tests. The FOG consists of an ASE light source, MIOC, fiber coil, and electronics. FOG is configured to be open-loop. Setup is designed to sample at high frequencies. Fiber coil length is approximately 1 km, which corresponds to 100 kHz sampling rate for the odd and even samples. Vibration input is a white profile that spans 20Hz to 2 kHz with 2 g_{rms} amplitude. Average optical power is at the photodetector is measured as 56 μA by the read-out circuit, which is half of the maximum optical power (I_0) under π/2 modulation. Electronics has a limitation that only 1.75 seconds of high sampling rate data can be collected. "sumP", $\Sigma P = P_1 + P_0$, is the fast optical power fluctuation which should be scaled and added to slow maximum optical power. The standard deviation of the optical power fluctuation percentage can be estimated by

$$\alpha = \frac{\mathrm{std}(P_1 + P_0)}{I_0 + \mathrm{mean}(P_1 + P_0)} \times 100 \tag{4.68}$$

which is obtained to be 0.1% under 0.5 g_{rms} and 0.35% under 2 g_{rms}. Two tests are related by the square of the input vibration g_{rms}, which is aligned with the simulation results presented in Chapter 4.1.4. The coefficient of the optical power fluctuation vibration input dependency can be estimated as 0.19%/g_{rms} with these tests where simulations suggested 0.34%/g_{rms}. It can be concluded that these two values are consistent. Neglecting any other bias error source, assuming a flat response from 2 kHz to 200 kHz in the simulation part, and the instability of the side effects of the vibration test setup (the magnetic field, acoustic noise, etc.) during the experiments can be the factors for the difference.

There are 4 different rotation rate estimations for this test. RateEst is the standard odd - even algorithm.

$$\mathrm{RateEst} = \frac{P_1 - P_0}{I_0} \tag{4.69}$$

RateEst2 is the estimation including the fast optical power normalization and RateEst3 includes the arcsin function after the normalization.

$$\mathrm{RateEst2} = \frac{P_1 - P_0}{I_0 + P_1 + P_0} \tag{4.70}$$

$$\mathrm{RateEst3} = \mathrm{asin}\left(\frac{P_1 - P_0}{I_0 + P_1 + P_0}\right) \tag{4.71}$$

Lastly, RateEst4 is the version without fast optical power normalization but with arcsin.

$$\text{RateEst4} = \operatorname{asin}\left(\frac{P_1 - P_0}{I_0}\right) \tag{4.72}$$

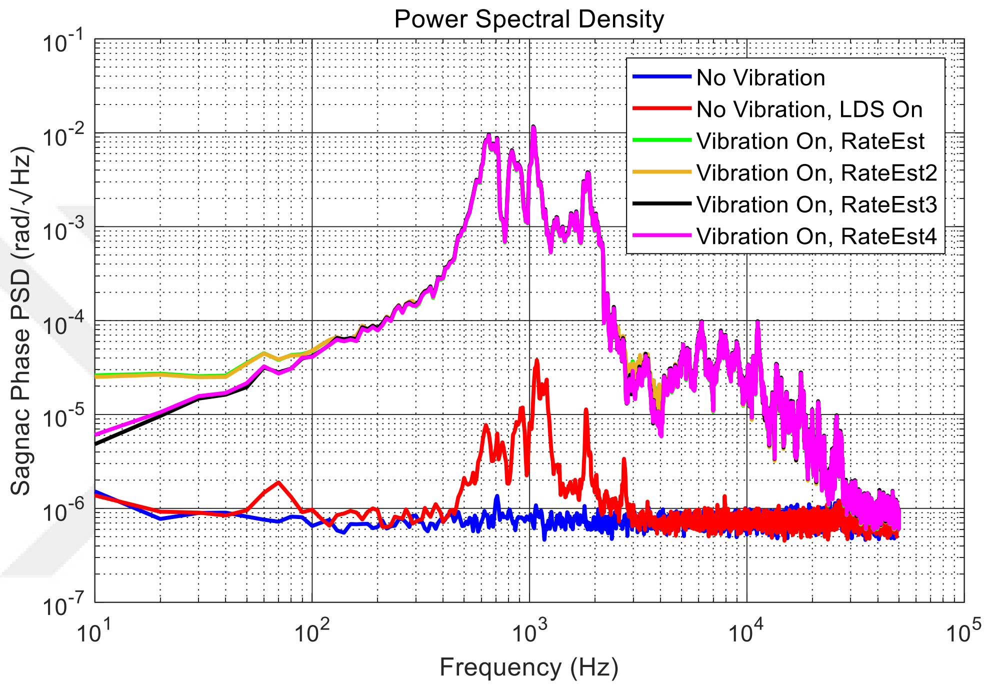

Figure 4.13: PSD for different rate estimations.

Test results are presented in Figure 4.13, which is a power spectral density graph where y-axis is the Sagnac phase difference density. The Sagnac scale factor of the FOG is 1.37 seconds so the rotation rate density can be calculated in °/s unit by multiplying the Sagnac phase with 44. The blue graph shows FOG output under stationary conditions, without any vibration. This is the FOG noise level which corresponds to 0.002 °/√h ARW value. The red graph is presented to show the disturbance generated by the vibration table, LDS. LDS On corresponds to the state of the air blower of the table. The disturbance is around 1 kHz spanning from 500 Hz to 2 kHz with spikes. This disturbance is not only additive to FOG output but also multiplicative to the input vibration level as seen on the rate estimation graphs. All rate estimation graphs share the same characteristics above 100 Hz. From 100 Hz to 500 Hz the mechanical Shupe error is seen. The mechanical Shupe error

(Chapter 4.2) is an error source created in the fiber coil by rapid contraction and relaxation of the fiber coils so this type of error is not related to the rate estimation techniques. So only the responses below 100 Hz are investigated. RateEst and RateEst2 graphs are nearly the same which means optical power fluctuation is not the main error source for this FOG, as expected. Similarly, RateEst3 and RateEst4 graphs behave also similarly while RateEst4 graph performs a little bit better by using the advantage of the fast optical power normalization. The main difference between RateEst and RateEst2 to RateEst3 and RateEst4 graphs is the arcsin function. Nonlinearity increases the noise level of the FOG as discussed by derivations and simulations. While there is no nonlinearity error and only the mechanical Shupe error exists for RateEst3 and RateEst4, the graphs continue to fall with the same rate as the frequency decreases.

CHAPTER 5

CONCLUSION

In this dissertation, we proposed a thermal sensitivity model for a FOG, that enables accurate simulations for obtaining the bias error, trimming effect, and strain inhomogeneity. Strong validation of the model includes bias error experiments of 4 fiber coils with two different designs, trimming simulations, and strain measurements. A validated simulation environment is a very useful tool for the analysis of the strain inhomogeneity through the fiber coil which is an important parameter that cannot be measured directly. A quadrupole FOG coil performance, which is comparable to the latest developments in the literature, is reached by controlling the strain inhomogeneity through the fiber coil.

Two side conclusions can be very useful for the thermal modeling of a FOG coil: The elastooptical error is the dominant effect relative to the pure Shupe error, and the bias error due to elongation is greater than the refractive index change.

A model to complete the bias error formation due to vibration is proposed. Vibration as a linear force (acceleration) results in a Sagnac phase shift due to the mechanical

Shupe error. This spurious rotation rate is suppressed by the closed-loop configuration and lastly multiplied by the optical power fluctuation.

The last part of the dissertation introduces the phenomenon that defines the loss of ARW performance under random vibration. Almost all literature focuses on the bias error performance under vibration. To the best of our knowledge, this dissertation is the first work trying to describe such a type of error for FOG.

REFERENCES

[1] V. Vali, and R. W. Shorthill, “Fiber Ring Interferometer”, Applied Optics, vol. 15, pp. 1099-1100, 1976.

[2] H. C. Lefèvre, The Fiber-Optic Gyroscope, Artech House, 1993.

[3] N. Barbour, and G. Scmidt, “Inertial sensor technology trends”, IEEE Sensors Journal, vol. 1, no. 4, 2001.

[4] E. Udd, and M. J. F. Digonnet, Design and Development of Fiber Optic Gyroscopes, SPIE, 2019.

[5] M. Webber, R. Willing, H. Rackowski, and A. Dineen "Modeling of rate error in interferometric fiber optic gyroscopes due to stress induced by moisture diffusion", Journal of Lightwave Technology, vol. 30, no. 14, 2012.

[6] D. T. Mead, and S. Mosor, “Progress with interferometric fiber optic gyro at Honeywell”, SPIE Defence and Commercial Sensing 2020, Proc. SPIE, vol. 11405, 2020.

[7] D. A. Egerov, A. V. Rupasov, and A. A. Untilov, “Ensuring radiation resistance of fiber optic gyroscope and ways to improve it”, Gyroscopy and Navigation 9, 2019.

[8] K. Böhm, K. Petermann, and E. Weidel, “Sensitivity of a fiber-optic gyroscope to environmental magnetic fields”, Optics Letters, vol. 7, pp. 180-182, 1982.

[9] P. Liu, X. Li, X. Guang, G. Li, and L. Guan, “Bias error caused by faraday effect in fiber optical gyroscope with double sensitivity”, IEEE Photonics Technology Letters, vol. 29, no. 15, 2017.

[10] Z. Zhang and F. Yu, “Analysis for the thermal performance of a modified quadrupolar fiber coil”, Optical Engineering, vol. 57, 2018.

[11] I. A. Esipenko, D. A. Lykov, and O. Y. Smetannikov, “Using the transversely isotropic characteristics of the coil to calculate the thermal-drift parameters of a fiber-optic gyroscope”, Journal of Optical Technology, vol. 86, 2019.

[12] S. Mitani, T. Mizutani, and S. Sakai, “Current status of fiber optic gyro efforts for space applications in Japan”, Fiber Optic Sensors and Applications XIII, Proc. of SPIE, vol. 9852, 2016.

[13] F. Mohr, "Bias error in fiber optic gyroscopes due to elastooptic interactions in the sensor fiber", Proceedings of SPIE, vol. 5502, 2004.

[14] F. Mohr, "Error signal formation in FOGS through thermal and elastooptical environmental influences on the sensing coil", Inertial Sensors and Systems, Karlsruhe, 2011.

[15] Y. Zhang and Z. Gao, "Fiber optic Gyroscope vibration error due to fiber tail length asymmetry based on elastic-optic effect", SPIE Optical Engineering, vol. 51, 2012.

[16] Z. Gao, Y. Zhang, and Y. Zhang, “Modeling for IFOG vibration error based on the strain distribution of quadrupolar fiber coil”, Sensors 16, vol. 1131, 2016.

[17] A. Cordova, “Reduction of fiber optic gyroscope vibration and temperature ramp sensitivities by controlling coil geometrical parameters”, U.S. Patent No. 5847829, 1998.

[18] N. Song, C. Zhang, and X. Du, “Analysis of Vibration Error in Fiber Optic Gyroscope”, Advanced Sensor Systems and Applications, Proc. SPIE, vol. 4920, 2002.

[19] A. Ohno, S. Motohara, R. Usui, Y. Itoh, and K. Okada, “Development of fiber optic gyroscope with environmental ruggedness”, Proc. SPIE 1585, Fiber Optic Gyros: 15th Anniversary Conf., 1992.

[20] G. Sagnac, “L’éther lumineux démontré par l’effet du vent relatif d’éther dans un interféromètre en rotation uniforme”, Comptes rendus de l’Académie des Sciences, vol. 95, 1913.

[21] G. Sagnac, “Sur la preuve de la réalité de l’éther lumineux par l’expérience de l’interférographe tournant”, Comptes rendus de l’Académie des Sciences, vol. 95, 1913.

[22] S. Merlo, M. Norgia, and S. Donati, Fiber Gyroscope Principles, Handbook of Fiber Optic Sensing Technology, John Wiley & Sons Ltd, 2000.

[23] J. R. Steele, “Digital phase modulator for fiber optic Sagnac interferometer”, U.S. Patent No. 5,137,359, 1991.

[24] T. Qui, J. Sanders, and Moser, “Alternate modulation scheme for an interferometric fiber optic gyroscope”, U.S. Patent No. 8,253,944, 2012.

[25] G. A. Pavlath, “Closed-loop fiber optic gyros”, Proc. SPIE, vol. 2837, pp. 46-60, 1996.

[26] S. Chen, J. Cheng, and W. Gao, “A phase modulation method for improving the scale factor stability of fiber-optic gyroscope”, IEEE International Conference on Mechatronics and Automation, pp. 37-42, 2008.

[27] “IEEE standard for inertial sensor terminology”, IEEE Std 528-2001.

[28] “IEEE standard specification format guide and test procedure for single-axis interferometric fiber optic gyros”, IEEE Std 952-1997.

[29] A. Cordova, R. A. Patterson, E. R. Goldner, and D. Rozelle, “Interferometric fiber optic gyroscope with inertial navigation performance over extended dynamic environments”, Proc. SPIE, Fiber Optic and Laser Sensors XI, vol. 2070, pp. 164-180 , 1993.

[30] G. A. Pavlath, “Challenges in the development of the IFOG”, AIAA, Guidance, Navigation and Control Conference, 2003.

[31] D. M. Shupe, “Thermally induced non-reciprocity in the fiber optic interferometer”, Applied Optics, vol. 19, no. 5, 1980.

[32] F. Mohr, "Thermooptically induced bias drift in fiber optical Sagnac interferometers", Journal of Lightwave Technology, vol. 14, no. 1, 1996.

[33] N. J. Frigo, "Compensation of linear sources of non-reciprocity in Sagnac interferometers", Proceedings of SPIE 0412, Fiber Optic and Laser Sensors I, 1983.

[34] S. Bilin, H. K. Kim, M. J. F. Digonnet, and G. S. Kino, “Reduced thermal sensitivity of a fiber optic gyroscope using an air-core photonic bandgap fiber”, Journal of Lightwave Technology, vol. 25, no. 3, 2007.

[35] V. Dangui, H. K. Kim, M. J. F. Digonnet, and G. S. Kino, “Phase sensitivity to temperature of the fundamental mode in air-guiding photonic bandgap fibers”, Optics Express 6669, vol. 13, no. 18, 2005.

[36] Y. Zhang, “Modeling of thermal-induced rate error for FOG with temperature ranging from -40C to 60C”, IEEE Photonics Technology Letters, vol. 26, no. 1, 2014.

[37] O. F. J. Tirat and J. F. M. Euverte, "Finite element model of thermal transient effect in fiber optic gyro", Proceedings of SPIE, vol. 2837, 1996.

[38] W. Ling, X. Li, Z. Xu, Z. Zhang, and Y. Wei, "Thermal effects of fiber sensings coils in different winding pattern considering both thermal gradient and thermal stress", Optics Communications 356, 2015.

[39] F. Schadt, “Physikalische Modellierung und Analyse thermisch und mechanisch bedingter Messabweichungen in faseroptischen Rotationssensoren”, Magdeburg University Ph.D. Thesis, 2012.

[40] S. Minakuchi, T. Sanada, N. Takeda, S. Mitani, T. Mizutani, Y. Sasaki, and K. Shinozaki, “Thermal strain in lightweight composite fiber-optic gyroscope for space application”, Journal of Lightwave Technology, vol. 33, no. 12, 2015.

[41] E. Quatraro, A. Pizzarulli, M. Catasta, G. Crescenti, E. Spinozzi, M. Zazzetta, and A. Cingolani, “High performance FOG for non-temperature stabilized environment”, Inertial Sensors and Systems, 2011.

[42] Z. Li, Z. Meng, T. Liu, and X. S. Yao, “A novel method for determining and improving the quality of a quadrupolar fiber gyro coil under temperature variations”, Optics Express 2521, vol. 21, no. 2, 2013.

[43] C. M. Lofts, P. B. Ruffin, M. Parker, and C. C. Sung, “Investigation of the effects of temporal thermal gradients in fiber optic gyroscope sensing coils”, Optical Engineering, vol. 34(10), 1995.

[44] R. A. Patterson, J. M. Todd, and G. S. Safonov, "Electronic manufacturing process improvement (EMPI) for automatic winding of quadrupole fiber optic gyro sensor coils", Technical Report, Litton Guidance & Control Systems, 1993.

[45] B. Osunluk, S. Ogut, and E. Ozbay, “Thermally induced bias error due to strain inhomogeneity through the fiber optic gyroscope coil”, Applied Optics, vol. 59, no. 33, 2020.

[46] B. Osunluk, “Double closed loop interferometric fiber gyroscope simulator design”, M.Sc. Thesis, Middle East Technical University, 2011.

[47] “Environmental engineering considerations and laboratory tests”, MIL-STD-810G, 2008.